EFFECTS OF THE SPIN-ORBIT INTERACTION ON ELECTRON TUNNELING IN SINGLE FERROMAGNETIC NANOPARTICLES

A Thesis
Presented to
The Academic Faculty

by

Patrick A. Gartland

In Partial Fulfillment
of the Requirements for the Degree
Doctor of Philosophy in the
School of Physics

Georgia Institute of Technology
December 2015

EFFECTS OF THE SPIN-ORBIT INTERACTION ON ELECTRON TUNNELING IN SINGLE FERROMAGNETIC NANOPARTICLES

Approved by:

Professor Dragomir Davidović,
Advisor
School of Physics
Georgia Institute of Technology

Professor Zhigang Jiang
School of Physics
Georgia Institute of Technology

Professor Martin Mourigal
School of Physics
Georgia Institute of Technology

Professor Michael Pustilnik
School of Physics
Georgia Institute of Technology

Professor David Anderson
School of Electrical and Computer Engineering
Georgia Institute of Technology

Date Approved: November 2, 2015

To Ashley,

Mom, Pops,

and Peter...

with love and gratitude

ACKNOWLEDGEMENTS

I would like to offer my sincerest gratitude to those who have made it possible for me to complete this work. First, I want to thank Drago, for accepting me into his lab and sharing with me his excitement for pursuing fundamental physics research, and for the privilege of studying under his guidance. I would also like to thank my committee, Professor Jiang, Professor Mourigal, Professor Pustilnik, and Professor Anderson, for agreeing to supervise my defense. I also am grateful to the US Department of Energy, Office of Basic Energy Sciences, Division of Materials Sciences and Engineering, whose funding allowed for my continuance in graduate school, under Award DE-FG02-06ER46281.

Next, I am very grateful for the time I could spend with Wenchao Jiang, and for his patience in training me to understand and grow skilled in the use of all the lab equipment. I could not have survived the rigors of the research lab without your guidance. I also learned a great deal in the lab from Jeff Wong, Jan Scrimgeour, and James Palmer. There are many other fellow graduate students and postdocs to whom I owe a great debt for their encouragement and camaraderie throughout my time at Georgia Tech. While this list is far from exhaustive, I would like to thank Lei Ma, Jan Kunc, Meredith Nevius, Martin Anquez, Dogukan Deniz, Wes Woodham, Andrew Price, James Casey, Yuntao Li, Brad Taylor, Michelle Alderman, Zhe Guang, John Indergaard, Matt Kinsey, Caitlin Baker, Jeff Tithoff, Keenan Zhuo, Chris Marcotte, Justin Ratnor, and Dongjoo Lee.

I am very thankful to the staff in the school of physics—to Shaun Ashley for her great kindness and helpfulness, to Keith for keeping the building running, to Scott for his help with our electronics, to the financial managers: Vicki, Mary Helen,

and Darryl; and to many others, including Dione, Nicole, Alison, and Kevin Carter. Thank you for all you do.

Next, I would like to thank the folks at Morningside Baptist, for offering warm community, and for their kindness, humility, and servants' hearts to both me and Ashley since I've been in graduate school. And finally, I would most like to thank my family—for their great patience, encouragement, and love during these long years in grad school. Thank you Mom and Pops, for your generosity and your instilling in me a love of life, humor, science, and learning. Thank you to my brother, Peter, for our exciting talks about engineering, and for your wit and encouragement. Thank you to Mr. and Mrs. Fish, for your thoughts and prayers. And most of all, thank you to my beautiful wife Ashley, who has had to suffer the brunt of my long hours on campus and bringing my work home. Thank you for your warmth, your encouragement, and for agreeing to go through life together. $\sim$*Psalm 19*

'Soli Deo Gloria'

TABLE OF CONTENTS

LIST OF FIGURES

SUMMARY

Recent technological innovations such as giant magnetoresistance and spin-transfer torque, along with a desire for researching the emergence of magnetism from a fundamental level, has led to much interest in understanding nanometer scale ferromagnets. In this dissertation, I use sequential electron tunneling to study the differential conductance spectra and magnetic properties of single cobalt and nickel particles below 5 nm in diameter, and observe a wealth of material-dependent effects. The spin-orbit interaction is a key mechanism in the observation of a variety of effects, including giant electron spin g-factors and shifts in the anisotropy energy of the magnetic particle upon the addition of a single electron. I show how such effects can lead to an effective magnetization blockade, which allows for the voltage control of magnetic hysteresis. I model the quantum mechanical system characteristics using master equations, and propose a new type of spin-transfer torque device that relies on the magnetization blockade effect.

CHAPTER I

INTRODUCTION AND BACKGROUND

In this chapter, I will discuss the basic concepts and theoretical background of ferromagnetism, the spin-orbit interaction, and tunneling spectroscopy in nanoparticles. Then, I will outline the goals of this dissertation.

1.1 Ferromagnetism

At its heart, magnetism is the result of angular momentum [101, 165], and arises from the coupling of magnetic moments at a quantum mechanical level. In insulating magnets, it is often expressed through a general magnetic Heisenberg Hamiltonian of the form $H_M = \sum_{i,j} J_{i,j} \vec{S}_i \cdot \vec{S}_j$, which is the pairwise sum over all individual spins of a given sample. Here, $J_{i,j}$ is the exchange coefficient between spins i and j, which in general can vary between pairs, and $\vec{S}_i$ is the quantum mechanical spin operator for spin i. To make the problem tractable, it is often assumed that the exchange coefficients are constant throughout a given sample (that is, $J_{i,j} = J = const.$) Further, the simplification is often made, since the exchange interaction is highly localized, that the coupling is only considered between nearest neighbors or next-nearest neighbors on the lattice. The sign of J determines the nature of the magnetic state of the material. If $J < 0$, then the configuration with minimal energy will favor the alignment of spins, and is known as a ferromagnetic state. If $J > 0$, on the other hand, then the minimizing the exchange energy will favor anti-alignment of neighboring spins. The latter case is known as an antiferromagnetic state. In transition metal ferromagnets, the itinerant exchange mechanism can be modeled using a Stoner or Hubbard model.

More exotic magnetic Hamiltonians can arise due to the interaction with the

local environment. For example, the Ruderman-Kittel-Kasuya-Yosida (RKKY) interaction and the superexchange interaction arise in systems where the two spins in the magnetic Hamiltonian interact via an intermediary spin. This occurs due to a nonmagnetic material separating the magnetic spins in the superexchange mechanism. Alternatively, the intermediary spin involves the conduction electrons in a neighboring metal in the RKKY interaction, and results in an effective exchange constant $J_{i,j}(\vec{R}_i - \vec{R}_j)$ that is an oscillatory function of spin position. This implies that two spins could be either ferromagnetically coupled or antiferromagnetically coupled, based on the displacement $\vec{R}_i - \vec{R}_j$ between them.

The ferromagnetic state of matter is unusual in terms of its size dependence, in that, in principle, there is no minimum sample dimension below which ferromagnetism disappears. Magnetism can persist down to the atomic length scales; however, the directional localization of the magnetization of a single magnetic atom or molecule is much weaker and tends to decay quickly [61, 84, 92, 115]. Additionally, even at the lowest temperatures, the magnetization stability is enervated by quantum tunneling of magnetization [85, 97].

The directional instability of magnetization in nanometer-scale ferromagnets arises due to the irreversible coupling of a magnetic sample to its environment, which induces spin randomization. This effectively quenches the ferromagnetic state and its key signature of magnetic hysteresis. The crossover from stable hysteresis to spin randomization is particularly pertinent as the length scale is reduced, and is well understood in the case of thermal equilibrium [32, 106, 152]. However, in the case of a perturbed, non-equilibrium ferromagnet, this crossover is more difficult to address. In magnetic molecules, magnetization measurements of large ensembles reveal robust magnetic hysteresis at sufficiently low temperatures, but measurements of a single magnetic molecule in a double tunneling barrier device show no hysteresis, even at temperatures much lower than the blocking temperature and near

zero bias voltage [34, 49, 76, 143]. Additionally, Loth *et al.* and Khajetoorians *et al.* have shown through atomically precise scanning tunneling microscopy (STM) experiments that antiferromagnetic and ferromagnetic spin chains of only a few atoms can display hysteresis, though the lifetimes of ferromagnetically stable states are much shorter [85, 97]. Similar STM experiments have demonstrated the origins of atomic scale magnetism through direct exchange and RKKY exchange mechanisms, which are critically altered by the substrate material and the presence and orientation of local adatoms [33,65,86,94,112]. All of these works reinforce the notion that magnetism on such length scales is significantly influenced by the local environment. In this thesis, I address the effects of sequential electron tunneling transport on nanometer-scale ferromagnetic particles.

Figure 1.1(a) displays an illustration of a large (bulk-scale) ferromagnetic material at a temperature that is large relative to the material's Curie temperature. At such temperatures, the material is divided into a collection of magnetic domains. In each domain, there is a local magnetic moment indicated by the arrows. The lines indicate domain walls, which separate the regions of differently oriented magnetic moments. The result of taking the average magnetic moment over the total volume of the sample will result in a net zero magnetization. As the temperature is lowered, or a strong magnetic field is applied, the domains will align and can lead to a large net magnetization on the sample. In the special case of ferromagnets below their Curie temperature, the material will exhibit a spontaneous magnetization even if there is no applied magnetic field. Figure 1.1(b) displays an illustration of a nanometer-scale single-domain magnet. In this case, the local exchange forces dominate, which results in a particle with all of the spins aligned into a large 'macrospin'. Such single-domain magnets are the subject of this thesis. Magnetic nanoparticles have garnered much attention recently due to their potential applications ranging from the medical field [113] to nonvolatile memory in computing.

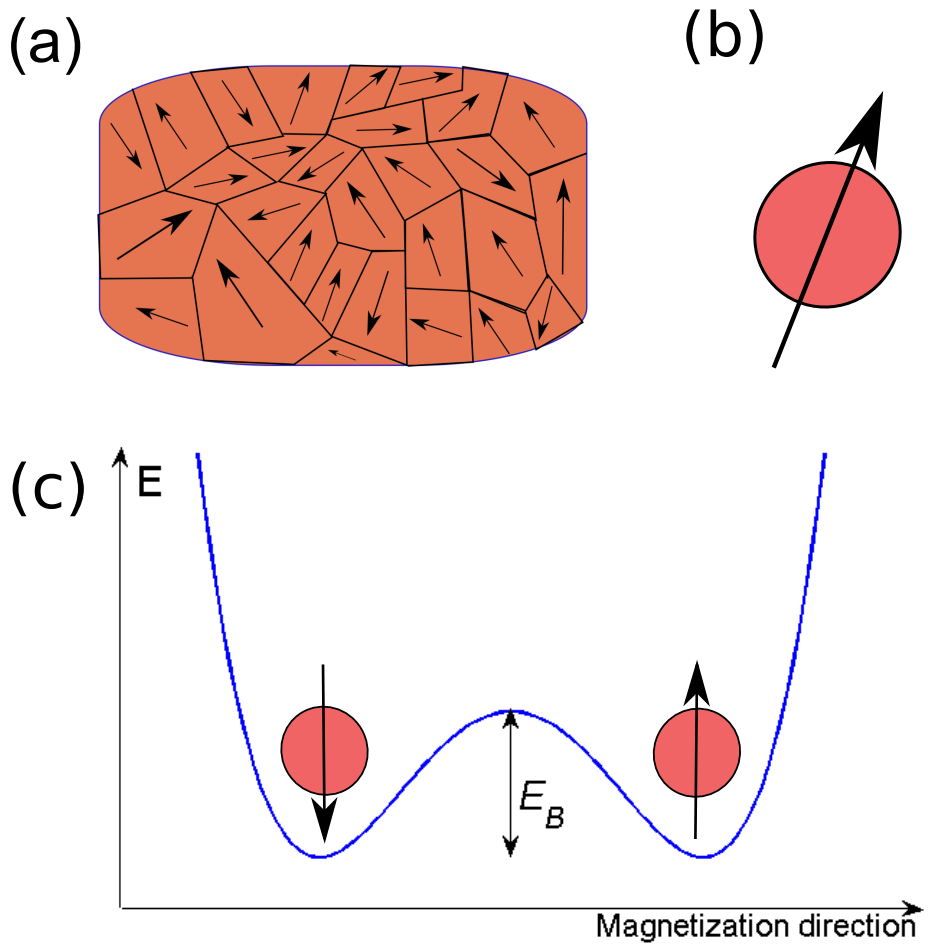

Figure 1.1: Ferromagnetism, domains, and anisotropy. Arrows indicate net magnetization orientation for given domain. (a) Illustration of large multi-domain magnetic material. (b) Smaller single domain magnetic particle. (c) Double-well energy potential as a function of magnetization angle, illustrative of stable magnetization states separated by an anisotropic energy barrier of height E_B.

1.1.1 Measuring Magnetism

Many techniques exist for the measurement of magnetic structure and magnetic fields, including Superconducting Quantum Interference Devices (SQUIDs), the magneto-optical Kerr effect (MOKE), vibrating sample magnetometry (VSM), ferromagnetic resonance, electron paramagnetic resonance, Mössbauer spectroscopy, the Hall Effect, and neutron scattering. Further, Giant Magnetoresistance and Tunneling Magnetoresistance can be used as a probe for inferring the relative orientation of magnetic domains.

1.1.2 Anisotropy

The form of the magnetic Hamiltonian quoted above is isotropic for a given pair of spins; that is, the energy depends only on the relative orientation of the two spins, not on their absolute direction relative to a fixed coordinate system. However, in many solids the magnetic energy can be minimized if the overall magnetization is oriented along one of the crystal axes. This variation of the magnetic energy as a function of magnetization angle relative to the crystal axes is a type of magnetic anisotropy, known as magnetocrystalline anisotropy, and arises due to the spin-orbit interaction.

Another type of anisotropy is due to the classical magnetostatic dipole interaction, and leads to shape anisotropy, and to the demagnetization field. The competition between the local exchange energy as indicated by the Heisenberg Hamiltonian, and the long-range classical magnetostatic dipole interaction leads to nontrivial minimal-energy states, and the formation of magnetic domains.

Variations on the magnetocrystalline anisotropy include magnetoelastic and surface anisotropy. The former results from mechanical perturbations of the crystal lattice, the distortion of which affects the minimal energy directions of the magnetization. The latter results from the truncation of a crystal in various facets at the surface of a solid.

Anisotropy with a strong enough energy barrier separating two local minima leads to the observation of hysteresis, which is characteristic of a bistable system. Such a bistable system is depicted in Figure 1.1(c). Anisotropy in a single domain ferromagnet is often described using the Stoner-Wohlfarth model. [137]

Depending on the size of the energy barrier separating the two local minima relative to other pertinent energy scales, external perturbations to the system can excite the magnetization over the barrier. The Néel-Brown model [32, 60, 106] describes this

the timescales of this process using an Arrhenius equation:

$$\tau_N = \tau_0 \exp\left(\frac{E_B}{k_B T}\right).$$

Here, τ_0 is the attempt time, τ_N is the Néel flip time, and k_B is Boltzmann's constant. If the magnetization flips many times on the time scale of the measurement, the particle is considered superparamagnetic, and the net measured magnetization will be zero.

1.2 Spintronics and Spin-Transfer-Torque

Intrinsic to the nature of the electron is both a charge ($e \approx -1.602 \times 10^{-19}$ C) and a quantized spin ($S_z = \hbar/2$, where $\hbar \approx 1.055 \times 10^{-34}$J $\cdot$ s), as illustrated in figure 1.2 (a)-(b). However, only in recent years has the electronic spin become an increasingly integral component to technological applications, leading to the emergence of spin electronics [47, 69, 155]. The discovery of the Giant Magnetoresistance (GMR) and Tunneling Magnetoresistance (TMR) effects (which express the difference in electrical resistance dependent on the degree of alignment of the magnetization in layers of the conducting medium) led to significant advances in 'spintronics' [12, 57]. Among these discoveries is the concept of spin transfer torque (STT), first predicted by Slonczewski and Berger [20, 135]. STT makes use of a spin-polarized current to induce magnetization motion and switch magnetic domains. In this way, magnetic domains in spin valve devices or TMR junctions can be controlled electronically, without the need for an external magnetic field.

Various reviews for spin-transfer torque can be found in references [69, 82, 120], but the process of STT switching can be summarized as follows. Typically, there is a 'free' or soft magnetization layer that is free to be manipulated, and a 'pinned' or hard magnetization layer that has a fixed orientation. These layers are separated by a tunneling barrier or a conducting layer for a TMR or GMR spin valve device, respectively. One technique of pinning a layer is by fabricating it adjacent to an

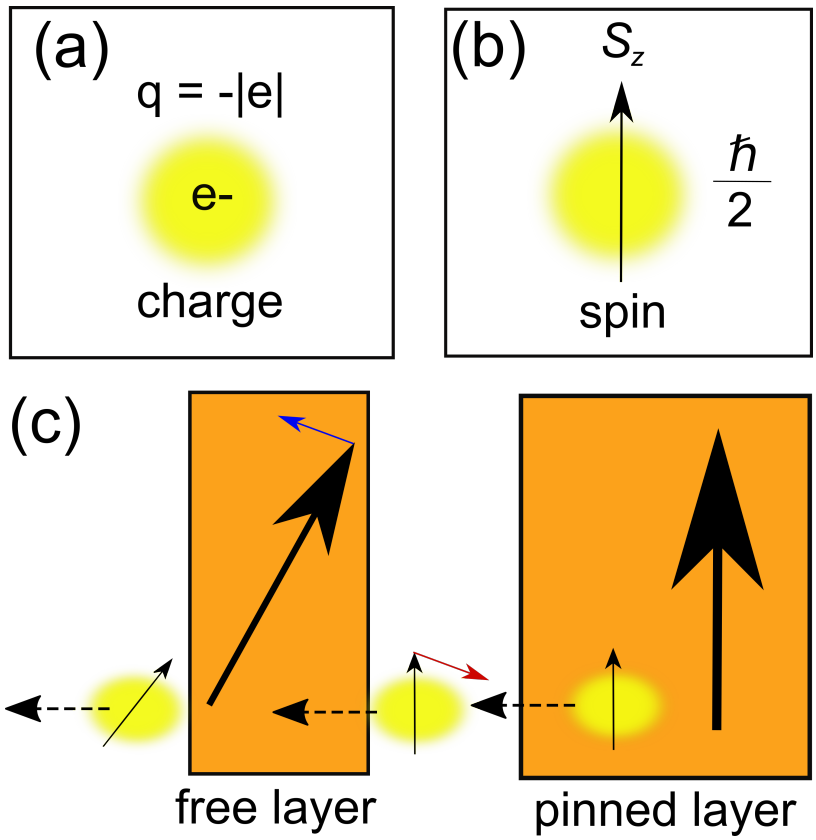

Figure 1.2: (a) Classical electronics only considered the charge component of the electron. (b) Modern spin-electronics also utilizes the quantum mechanical intrinsic spin of the electron. (c) Illustration of spin-transfer torque. Electrons flow from right to left, beginning in the pinned magnetic layer. As the electrons encounter the free magnetic layer, their spin becomes polarized along the magnetization direction of the layer, experiencing a torque illustrated by the red arrow. The free layer experiences a reactive torque, or spin-transfer torque, illustrated by the blue arrow. The net effect of current flow in this direction results in an aligning of the free layer magnetization with that of the pinned layer.

antiferromagnetic layer, which takes advantage of the exchange bias [133]. As is shown in figure 1.2(c), for electronic current that flows from right to left, the electrons have their spins polarized along the same direction as the magnetization in the pinned layer. Assuming that they maintain their spin polarization in the interstitial region between the free and pinned layers, then an impinging electron will experience a torque (indicated by the red arrow in the figure) that aligns the electronic spin with the magnetization of the free layer. However, conservation of angular momentum

implies that the electron will also exert a transfer torque to the free layer, indicated by the blue arrow in the figure. The net result of many such impinging electrons is to align the free layer with the pinned layer. The reverse process is also possible. For example, an electronic current flowing from left to right in the interstitial region will scatter from the pinned layer with a spin polarized opposite the direction of the pinned layer. This back-scattered spin-down current will exert a torque on the free layer that will have the net effect of aligning the free layer anti-parallel to the fixed layer. In this way, STT has been modeled in domain switching, macrospin modeling, and scattering processes using Boltzmann transport [81, 136, 138, 139, 158–162].

An electronic current injected from a ferromagnetic lead into a normal metal or semiconducting material will maintain its spin polarization for a certain length scale, before spin-flip scattering returns the current to its equilibrium, non-spin-polarized state. This process is analogous to the propagation of a minority charge carrier in a doped semiconductor (for example, holes diffusing in an n-type semiconductor) [96]. As there is a characteristic length known as the diffusion length over which a minority hole can propagate within an n-type region before recombination occurs, there is a similar spin diffusion length, which indicates how far a spin-polarized current can propagate before becoming unpolarized [18].

Currently, the concept of spin-transfer torque has not reached its full potential. While there are many efforts to establish magnetic memory in the form of MRAM that can be switched with spin-polarized currents, issues still exist in the implementation [82]. For example, one of the main forms of commercial spin-transfer torque is accomplished through thermally assisted switching citeprejbeanu. However, the heating process is the limiting factor in achieving higher switching rates.

In this thesis, based on the results we found regarding a magnetization blockade, we will propose a type of voltage-controlled spin-transfer torque that could offer advantages over traditional current-driven spin-transfer torque. While our experiments

focused on the low-temperature regime where we can more clearly elucidate the relevant physical processes, our discoveries of different fundamental effects is of crucial importance in expanding technologies to higher temperatures. Our basic research and exploration of the magnetization blockade effect hold a lot of promise in the potential for realizing more efficient spin-transfer torque devices.

1.3 Modeling Magnetization Dynamics

The notion of magnetization dynamics can be modeled in various ways, including the Landau-Lifshitz-Gilbert equation [131], which can be modified to account for spin-transfer torque [134]. Alternatively, the relevant magnetization angles s_i can be modeled using a stochastic Langevin equation [132]:

$$\frac{\partial s_i}{\partial t} = -\frac{1/\tau_0}{k_B T}\frac{\partial E}{\partial s_i} + \sqrt{\frac{2}{\tau_0}}\xi(t).$$

Here, τ_0 is again the attempt time, E is the energy of the system, and $\xi(t)$ is the stochastic white-noise forcing term. The distribution of s_i can be described by a probabilistic Fokker-Planck equation, or equivalently by a master equation [25, 132]:

$$\frac{\partial P_i}{\partial t} = \sum_j \left[\Gamma_{j\to i} P_j - \Gamma_{i\to j} P_i\right].$$

Here, $\Gamma_{i\to j}$ is the rate of transition from state i to state j. An example of such quantum master equation simulations with the inclusion of spin-transfer torque effects in mesoscopic magnets is found in reference [149]. It has also been considered in references [73] and [147]. Primarily, in this thesis, I use the master equation approach since the transition rates can be easily calculated, based on our phenomenological Hamiltonian.

1.4 The Spin-Orbit Interaction

The atomic spin-orbit interaction arises because an electron in a central potential moves in a non-inertial reference frame [124]. The ion about which the electron is

orbiting exerts an electric field, which transforms into an effective magnetic field in the non-inertial frame of the electron. The effective magnetic field couples to the magnetic moment of the spin of the electron, and leads to a term in the Hamiltonian proportional to $\vec{L} \cdot \vec{S}$, where $\vec{L}$ is the orbital angular momentum of the electron about the ion, and $\vec{S}$ is the electronic spin. To convert from the atomic spin-orbit interaction into a form usable in a solid, the Hamiltonian can be modeled, for example, using a tight binding method [48].

The spin-orbit interaction leads to many interesting effects, which range from band structure alterations in semiconductors [96] to a mechanism for the spin-hall effect [44]. Recently, Rashba spin-orbit splitting was found in a topological insulator using spin-resolved Angle-Resolved Photoemission Spectroscopy (ARPES) [88]. Such an effect offers a promising candidate for spintronics applications [79]. In this dissertation, the main results of the spin-orbit interaction are due to its effect on magnetocrystalline anisotropy and its ability to break spin-related symmetries. As I will discuss in detail, the main effects considered in this dissertation involve large spin g-factors [50], and the establishment of a magnetization blockade [51], which can lead to voltage control of magnetic hysteresis.

1.5 Energy Scales

One of the fascinating (and often complicated) aspects of our work involves the interplay of a number of different energy scales. Independently, these scales can be studied and modeled; but taken together, non-trivial effects can emerge.

1.5.1 Thermal Energy

The energy associated with the thermal energy of a system is on the order of $E_T = k_B T$, where k_B is Boltzmann's constant, and T is the system temperature in units of Kelvin. In our experiments, initial resistance measurements of samples are conducted at room temperature ($\sim$ 300K), which corresponds to a thermal energy of $E_T =$

25.85 meV. The measurement of preliminary current hysteresis loops as a function of magnetic field are taken at 4.2 K, which corresponds a thermal energy of $E_T = 0.362$ meV. These measurements are performed by submerging a sample directly into a liquid helium dewar. Further precise measurements are conducted in the dilution refrigerator, which allows us to vary the temperature between 0.03 K and 4.2 K. The lowest temperatures in our dilution refrigerator correspond to a thermal energy of 2.59 μeV. In the dilution refrigerator, the temperature is recorded by use of a calibrated resistor.

1.5.2 Charging Energy

The energy (or work) required to add a single electron of charge e to a metallic island separated from its environment, with a corresponding capacitance C, is given by $E_c = e^2/2C$. Because the capacitance scales with the length L of the conductor, ($C \sim \epsilon_0 L$), smaller metallic particles will have a smaller capacitance, leading to larger values of E_c [165]. At low temperatures and small particle sizes, E_c can dominate the competing energy scales, which leads to a finite bias voltage necessary for tunneling an electron onto the particle.

1.5.3 Zeeman Energy

According to Kramers' theorem, eigenstates of a system invariant under time reversal are (at least) doubly degenerate. However, if a magnetic field is introduced (which breaks time-reversal symmetry), the Kramers doublets will split as a linear function of magnetic field. In atomic single-electron systems, this splitting of degenerate levels is known as the Zeeman effect. The energy associated with a magnetic moment $\vec{m}$ coupled to a magnetic field $\vec{B}$ is given by $E = -\vec{m} \cdot \vec{B}$. The splitting of the Zeeman energy levels in a magnetic field $\vec{B}$ is given by $E_z = g\mu_B B$, where $\mu_B = e\hbar/2m$ is the Bohr magneton. Typically, $g \approx 2$ for the electronic g-factor, which leads to an energy scale of $g\mu_B = 115\mu$eV/T.

More generally, an effective electronic g-factor can be defined in tunneling spectroscopy experiments, where g can be determined from the slope of spectral lines of Zeeman-split Kramers doublets with respect to magnetic field.

1.5.4 Spin-Orbit Energy

There is an energy scale ϵ_{SO} associated with the lifetime of the spin orbit flip time τ_{SO}, given by $\epsilon_{\mathrm{SO}} = \hbar/\tau_{\mathrm{SO}}$ [31, 36, 59, 102, 116]. One of the mechanisms for spin-flipping is the Elliot-Yafet mechanism [45, 163], in which an electron will change its spin orientation with a certain probability each time it encounters a momentum-scattering event. According to reference [36], the spin-orbit energy shifts ϵ_{SO} will be given by $\epsilon_{\mathrm{SO}} = \hbar/\tau_{\mathrm{SO}} \sim \xi_d^2/W_d$. Here, ξ_d is the degree of coupling between the spin and orbital components of the wavefunction, and is on the order of 73 meV, 88 meV, and 106 meV for Fe, Co, and Ni, respectively [43], while W_d is the 3d-band width, which is on the order of 4 or 5 eV in Fe, Co, and Ni. It should be emphasized that these are only estimates, and the spin-orbit energy shifts can vary between 1 meV and 10 meV, depending on the specific particle realization [36]. These energy shifts are expected upon the tunneling of a single electron onto a magnetic particle, and are crucial for the model of a magnetization blockade introduced in this thesis.

1.5.5 Quantum Confinement Energy

As is often emphasized in elementary quantum mechanics courses, the energies of bound electronic states form a discrete spectrum of values, corresponding to standing wave solutions of the Schrödinger equation. The spacing between these eigenenergy values varies with the degree of confinement; the more tightly bound the electron, the larger the corresponding energy level spacing. For example, the energy levels for an electron-in-a-box with infinite potential wells are given by $E_n = n^2\hbar^2\pi^2/(2mL^2)$, where L is the length of the confinement region, m is the mass of the electron, and n

takes on positive integer values. While the spacing varies as a function on n, the overall scale of the separation between consecutive energy levels is inversely proportional to L^2. That is, the smaller the confinement region, the more largely spaced the energy levels. Similarly, the energy levels for a harmonic oscillator (quadratic confinement potential in the spatial variable) is given by $E_n = \hbar\omega(n + 1/2)$, where n is again a positive integer, and $\omega = \sqrt{k/m}$. Here k is the effective spring constant, and a stiffer spring leads to a larger value for k, and therefore stronger confinement potential. In the harmonic oscillator case, the energy levels are equally spaced (that is, they do not depend on n. For stronger confinement over a smaller region, the levels are spaced further apart in energy. Such confinement effects are prevalent in fabricated structures that are essentially two-dimensional, which can arise from the confinement of a physical boundary, such as the atomic extent of a layer of graphene [53, 107] or the recent studies on transition metal dichalcogenides, such as MoS_2 [117, 148]. Alternatively, the confinement boundary can result from the local electrostatic environment as is the case in modulation-doped epitaxial semiconducting heterojunctions [96]. Regardless of the cause of confinement, the results are similar. Electrons confined in one dimension behave as a two-dimensional electron gas, and therefore acquire an altered density of states. Similarly, confinement in two dimensions leads to an effective one-dimensional electron gas (as is the case in graphene nanoribbons and carbon nanotubes). Finally, electrons confined in all three dimensions behave as effective zero-dimensional structures, and are called artificial atoms or quantum dots.

1.5.6 Fermi Energy and Mean Level Spacings

Because electrons are fermions (that is, they have half-integer spin in units of $\hbar$), they obey the Pauli exclusion principle. Therefore, for a solid at $T = 0$, the electrons are prevented from condensing into the lowest energy orbital, but rather must pile into the increasing energy states so that no two electrons have the same set of quantum

numbers. The energy value $\mu = \epsilon_F$ at $T = 0$, which demarcates the highest occupied orbital from the lowest unoccupied orbital, is known as the Fermi energy. At nonzero temperatures, the average occupation of an orbital at energy E is governed by the Fermi function:

$$f(E;T) = \frac{1}{1 + \exp\left(\frac{E-\mu}{k_B T}\right)}$$

The Fermi energy of Ni and Co are 8.7 eV and 9.5 eV, respectively [114]. In normal metals, the energy cost of promoting an electron to a higher discrete level typically dominates the exchange energy. However, due to the strong electron-electron interactions in ferromagnets, there will be a rearrangement of the density of states depending on the direction of the spin. This leads to two separate spin bands, known as the 'majority' and 'minority' spin bands. Each of these bands has a different effective Fermi energy $\epsilon_{\mathrm{F,maj}}$ and $\epsilon_{\mathrm{F,min}}$ for the majority and minority bands, respectively, and the separation of these effective Fermi energies is given by the exchange energy. Further, the density of states varies as a function of energy, so the average discrete level spacing for the different spin bands at their respective Fermi energies will be different.

To calculate some of the relevant energy scale data, I followed the process described in references [37] and [90]. Our data for the exchange splitting and the minority and majority level spacings were derived from reference [114]. For the mean level spacing d_σ of the majority and minority levels, we used the expression (as is described in footnote 15 of reference [90]):

$$d_\sigma = 1/[N_a \cdot D_\sigma(\epsilon_F)],$$

where $D_\sigma(\epsilon)$ is the spin-dependent bulk density of states per atom, N_a is the number of atoms, and σ indicates either the majority or minority band. The difference in total integrated density of states gives the conversion factor $2S_0/N_a$, which allows us to write the energy spacing in terms of S_0 rather than N_a. The total integrated density of states for the spin polarized bands for majority and minority electrons,

respectively, are given by 5.33 and 4.66. The difference of these two yields a value of $2S_0/N_a = 0.67$. The density of states for the majority and minority electrons, respectively, are given by 2.51 states/Ry/atom and 21.28 states/Ry/atom. Level spacings $d_{\rm maj}$ and $d_{\rm min}$ for the nickel majority and minority levels, as evaluated at their respective Fermi levels, are then given by:

$$d_{\rm maj} = 1/N_a \cdot [2.51 \text{ Ry}^{-1} \cdot (1 \text{ Ry}/13.6 \text{ eV})]^{-1} = 5.41 \text{ eV}/N_a \cdot 0.67 N_a/(2S_0) = 1.8 \text{ eV}/S_0$$

$$d_{\rm min} = 1/N_a \cdot [21.28 \text{ Ry}^{-1} \cdot (1 \text{ Ry}/13.6 \text{ eV})]^{-1} = 0.64 \text{ eV}/N_a \cdot 0.67 N_a/(2S_0) = 0.2 \text{ eV}/S_0$$

Similarly, we used reference [114] to calculate the majority and minority level spacings for cobalt, in order to affirm the validity of our calculations. In the case of cobalt, the total integrated density of states values for the majority and minority bands are given by 5.32 and 3.67, which leads to a value $2S_0/N_a = (5.32 - 3.67) = 1.65$. The density of states for the majority and minority electrons, respectively, are given by 2.46 states/Ry/atom and 9.53 states/Ry/atom. Level spacings $d_{\rm maj}$ and $d_{\rm min}$ for the cobalt majority and minority levels, as evaluated at their respective Fermi levels, are then given by:

$$d_{maj} = 1/N_a \cdot [2.46 \text{ Ry}^{-1} \cdot (1 \text{ Ry}/13.6 \text{ eV})]^{-1} = 5.53 \text{ eV}/N_a \cdot 1.65 N_a/(2S_0) = 4.6 \text{ eV}/S_0$$

$$d_{min} = 1/N_a \cdot [9.53 \text{ Ry}^{-1} \cdot (1 \text{ Ry}/13.6 \text{ eV})]^{-1} = 1.43 \text{ eV}/N_a \cdot 1.65 N_a/(2S_0) = 1.2 \text{ eV}/S_0$$

Note that these results are identical to those obtained from reference [90], which quotes values of "$d_{min} \approx 1.19$ eV/s_0, and $d_{maj} \approx 4.61$ eV/s_0, and the exchange splittings of the Fermi energies $\Delta_F \equiv \epsilon_{F,maj} - \epsilon_{F,min}$ (≈ 2 eV for cobalt)."

Using reference [114], we used the difference in energy between the main peaks in the density of states for the majority and minority bands to estimate the exchange splitting energy Δ. Doing so yields a value of ≈ 1 eV.

I repeated all the same calculations for the data for cobalt in reference [114] as well, and found that our data agreed with the results obtained for cobalt in references [37] and [90].

In this case, the difference in majority and minority Fermi levels is approximately 2 eV, the same value quoted above from reference [90]. Note that there are different conventions for defining the exchange energy, which can differ by a factor of 2. If the exchange Hamiltonian is given by $H_M = JS \cdot S \equiv \frac{U}{2} S \cdot S$, then the "exchange energy" can either be defined as J or as U. I use the latter convention, and note as in reference [90] that "U may be estimated as $U \approx \Delta_F / s_0$", where Δ_F is the exchange energy splitting between the minority and majority fermi levels. Defining the exchange energy in the alternate way (by using $J \equiv U/2$), I estimate $J \approx 0.5$eV.

1.5.7 Altering the Energy Scales

As mentioned previously, interesting effects emerge as the result of the interplay of different energy scales. Therefore, the precise manipulation of various energy scales is crucial for exploring novel effects. The thermal energy is easily controlled via the positioning of samples in liquid nitrogen, liquid helium, or in the dilution refrigerator. The Coulomb charging energy can be controlled by altering the capacitance of the sample, either through changing the particle size or by adding a capacitively coupled gate electrode. The Zeeman energy is determined entirely by the g-factor and the applied magnetic field. For samples in the dilution refrigerator, the superconducting magnet can be ramped to fields as high as 12 T. The spin-orbit energy varies from sample to sample, and is harder to control precisely without fabricating a large statistical set of samples. The quantum confinement energy depends crucially on the size of the particle, and the dimensionality of confinement. While the Fermi energy cannot be changed for a given material, the mean discrete level spacing of particles at their respective minority and majority Fermi levels can be altered by controlling the size of the particles. Here I only predict a mean discrete level spacing; different samples will realize different instances of such spacings. In measuring such effects, our main tool is sequential electron tunneling transport [154].

1.6 Current Response Characteristics

In scientific research and engineering, a substantial number of characteristics can be probed by measuring the electronic current response of a system, I, to an applied bias voltage, V. In the simplest case, an ideal resistor with resistance R exhibits a linear $I(V)$ characteristic, with a slope equal to $dI/dV = 1/R$. An ideal diode exhibits current rectification properties as part of its current response to an applied bias voltage. That is, the current response is asymmetric with respect to the sign of V, and follows the form of an exponential function: $I(V) = I_o(e^{qV/k_BT} - 1)$. Here, I_o is the leakage current for a reverse-biased junction, q is the magnitude of electronic charge, V is the applied bias voltage, and T is the temperature in Kelvin. For $V < 0$, the current response is suppressed, or rectified. Although the current expressions above refer to the ideal response characteristics, they are instructive for how to interpret measurements in more complex experiments. For more complicated current response functions, one can define the differential conductance dI/dV which denotes an effective inverse resistance for different applied bias voltages.

Low temperature measurements of electron tunneling in quantum dots led to the observation of current suppression in the low voltage regime. This 'blockade' of current can arise due to a variety of mechanisms, such as the quantization of the electronic charge, or the quantization of discrete energy levels as a result of quantum confinement. In the experiments considered in this thesis, I use single electron tunneling spectroscopy to probe the magnetic Hamiltonian of single ferromagnetic nanoparticles. In such a case, both current suppression mechanisms are at play. That is, I observe both Coulomb blockade due to the quantization of the electronic charge, and steps in the $I(V)$ plot due to discrete particle energy levels.

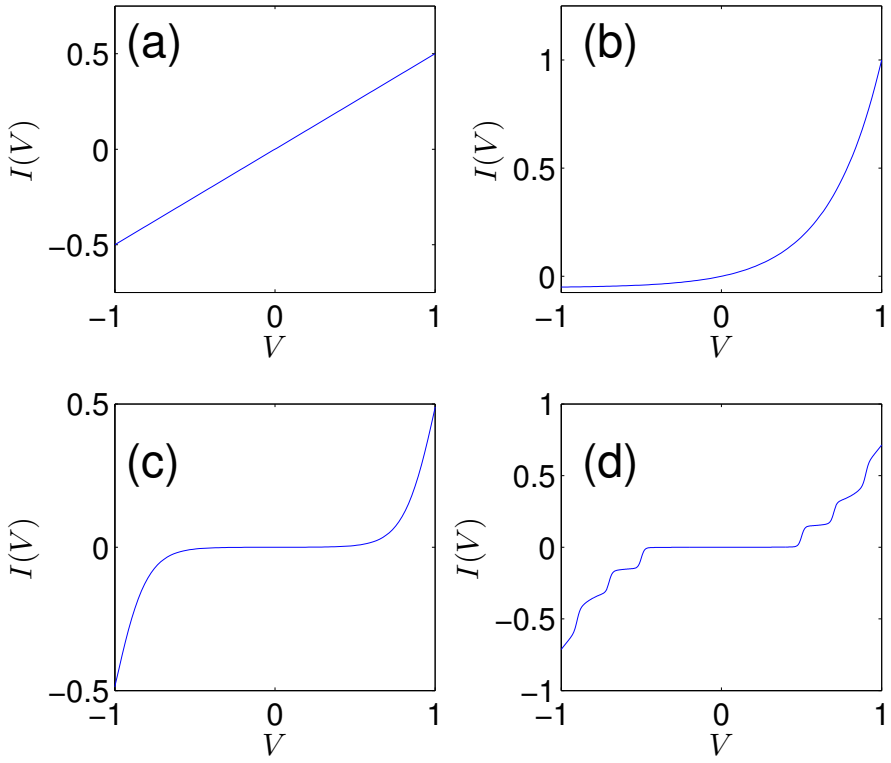

Figure 1.3: Current response curves. (a) $I(V)$ characteristics of an ideal resistor. (b) $I(V)$ characteristics of an ideal diode. (c) $I(V)$ characteristics exhibiting Coulomb blockade. (d) $I(V)$ characteristics exhibiting both Coulomb blockade and discrete energy levels.

1.6.1 Coulomb Blockade and Sequential Electron Tunneling

In the particles studied in this dissertation, the charging energy required to add a single electron to the particle requires a measurable bias voltage before tunneling current onset occurs. For low bias voltages, therefore, the current is suppressed by the Coulomb blockade. In such a situation, the current response curve to an applied bias voltage can resemble the structure of that in figure 1.3(c) or (d). Because the nano-island is localized from its environment via tunneling barriers, the electron number on the dot is a well defined quantity. Similar device configurations have been well-studied previously, and include a model for 'orthodox' Coulomb blockade transport. [10, 19, 166]. In such as configuration, a finite bias voltage on the order

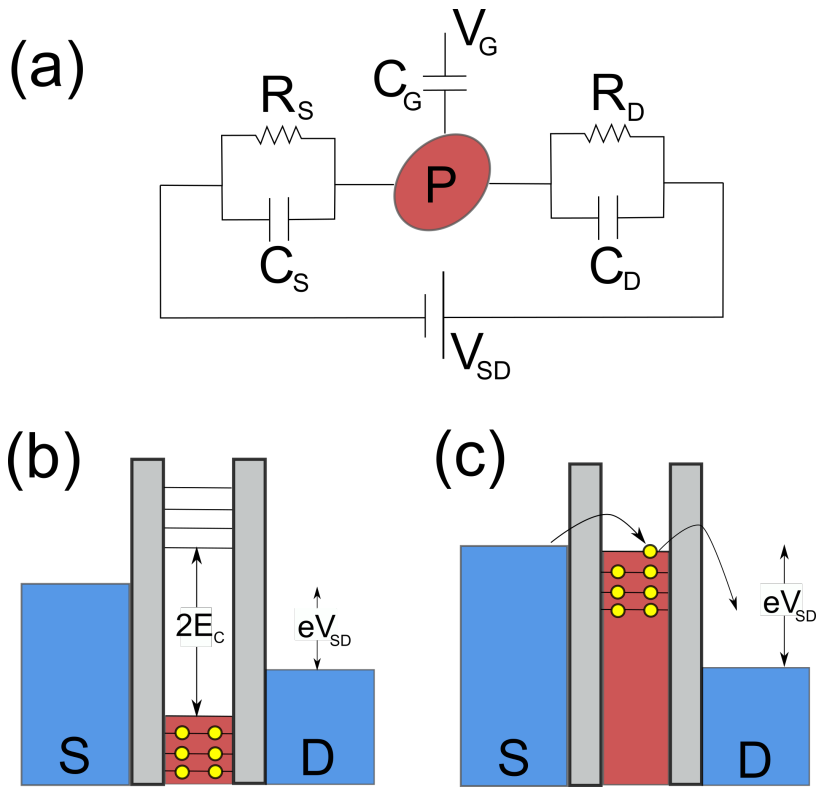

Figure 1.4: (a) Equivalent circuit for double tunnel junction. (b) Energy band diagram of double tunnel junction in a state of Coulomb blockade. (c) Energy band diagram illustrating the onset of current at the edge of Coulomb blockade.

of millivolts will supply enough energy to tunnel a single electron onto the particle. However, as long as the voltage is maintained at a low enough value, only a single electron can tunnel onto the particle at a time, before tunneling off again. To explain this effect, consider the circuit diagram in figure 1.4.

To account for discrete quantum states of the particle requires a model beyond orthodox Coulomb blockade, and can be studied with techniques such as Random Matrix Theory [3,4]. Higher order effects can be observed, such as elastic and inelastic cotunneling, which can be explained through retaining further perturbative terms in the tunneling Hamiltonian [4]. When the coupling of the particle to the conductive leads becomes stronger (that is, when the resistance approaches or becomes lower than the quantum resistance $R_Q = h/e^2$, then there is an intrinsic broadening $h\Gamma$ of the discrete levels on the dot associated with a finite lifetime. As long as the tunneling

resistance $R_T \gg \hbar/e^2$, which amounts to $h\Gamma$ being much smaller than other relevant energy scales of the system (which is the case in the experiments under consideration in this thesis), then cotunneling and higher order effects can be safely ignored. [93]

When the particle is well-separated from its tunneling leads, the effects of electron tunneling can be studied by using a reduced density matrix approach. A general procedure for studying a system with mixed quantum states makes use of the density matrix, which allows for keeping track of the populations (or probabilities) of the basis states and coherences among the basis states. For a given system Hamiltonian H and a density matrix ρ, the temporal evolution of the density matrix can be calculated from the Liouville-von Neumann equation:

$$i\hbar\frac{\partial\rho}{\partial t} = [H, \rho].$$

However, H in the above equation includes both the particle and the tunneling leads. At this point, a common procedure is to 'trace over the reservoirs,' which allows us to partition the full density matrix into a reduced density matrix that involves the particle Hamiltonian, and then treat the tunneling process from the reservoirs (or leads) as a perturbation. The metallic (or ferromagnetic) leads are assumed to be in local thermodynamic equilibrium, described by respective Fermi distributions functions and held fixed at a specific electrochemical potential. This leads to a method of tracking both the populations (probabilities) of occupation of the particle eigenstates, as well as the coherences among these states, known as a generalized master equation.

However, for this work, I am primarily concerned with the populations of the eigenstates, or the diagonal elements of the reduced density matrix. The tracking of the eigenstate probabilities makes use of a master equation, and the rate of transitions among the system states is calculated using the Fermi golden rule:

$$\Gamma_{i\to f} = \frac{2\pi}{\hbar}|\langle f|\hat{H}_T|i\rangle|^2\delta(E_f - E_i).$$

Again, here the initial states $|i\rangle$ and final states $|f\rangle$ refer to the total system eigenstates

(particle plus leads), and $\hat{H}_T$ is the tunneling Hamiltonian operator. However, I have mentioned previously the partitioning of the system into the particle and the leads, which allows the factoring of the initial and final states of the system as: $|i\rangle = |f_{L,i}\rangle|f_{R,i}\rangle|\alpha_i\rangle$ and $|f\rangle = |f_{L,f}\rangle|f_{R,f}\rangle|\alpha_f\rangle$. Here, f_L and f_R refer to the Fermi distribution functions in the left and right leads, respectively, and α refers to an eigenstate of the particle. Once attained, the tunneling rates can be incorporated into the master equation simulations to determine steady state behavior of the probability distribution, which in turn can be used to calculate the tunneling current.

1.6.2 Spin Blockade

A similar current blockade effect has been observed in double quantum dots [68, 78, 92, 95, 109, 121, 130], and has been identified as a spin blockade, due to the reliance of the mechanism on electronic spin rather than charge. The basic configuration for a spin blockade arises when there exist two quantum dots separated in a triple tunnel junction, with surrounding metallic contacts. If each dot has a single discrete level with a degeneracy of 2 to allow for tunnel electrons to assume either the state spin-up or spin-down on each dot, and if one of the dots already has a single electron in a well-defined discrete state, then the configuration will exhibit current rectification based on the sign of applied bias voltage. If the current first tunnels onto the occupied dot, then only a spin of the opposite orientation can tunnel onto the dot. Then, the electron is not restricted in tunneling into the second dot, and then off into the drain lead. If a bias is applied in the opposite direction, however, then if an electron of the same spin tunnels onto the unoccupied dot first, it is blocked from tunneling onto the occupied dot due to the energy cost of establishing a triplet state. That is, two spin-up electrons are prohibited due to the Pauli exclusion principle on the occupied dot. The only way for a spin up electron to tunnel onto the dot is for it to occupy a higher discrete level, which is energetically inaccessible for low bias voltages.

Later, I will describe a similar magnetization blockade effect, in which the spin-orbit anisotropy energy shifts can prevent the particle magnetization from departing beyond a critical angle from the easy axis, where the easy axis is defined as the energetically favorable magnetization direction. This effect leads to the voltage control of magnetic hysteresis in nanomagnets.

1.7 Semiconducting Quantum Dots

The increasingly precise techniques of nanofabrication, including methods such as electron-beam lithography and molecular beam epitaxy, have allowed for the detailed study of devices whose length scales necessitate the incorporation of quantum mechanical effects. In particular, quantization effects in semiconductors can be observed at larger length scales (fraction of a micron) as opposed to the exceedingly small scales required for metallic samples ($\sim$ 10 nm or less) [93]. Epitaxially grown semiconducting heterojunctions have allowed for the fabrication of extreme confinement of electrons in one dimension in order to form a two-dimensional electron gas. With the addition of metallic gates, the electrons can be confined even further dimensionally, allowing for precise control of sequential electron tunneling. The analogous classical trajectories of electrons in such samples exhibit chaotic trajectories, leading to a configuration for probing the effects of quantum chaos [100]. The statistics of the energy levels in such systems are amenable to statistical studies by random matrix theory, which rely on a few general symmetry properties of the particular system.

Additionally, very large g-factors due to *orbital* electronic motion have been observed in semiconducting quantum dots [105, 108, 128]. Later in this dissertation, I will show examples of large *spin* g-factors that we measured in Co samples using differential conductance tunneling spectroscopy [50]. Such effects were predicted by Gorokhov and Brouwer [55, 56], and are due to the interplay of the spin-orbit interactions and the electron-electron interactions in ferromagnetic quantum dots.

1.8 Metallic Quantum Dots

In addition to semiconducting quantum dots, research has been performed recently on metallic materials, which require sizes of the order of 10 nm in order to probe the discrete energies due to quantum confinement. Rather than using an electrostatic gate to constrict the location of electrons into a quantum well, metallic dots utilize the physical boundary of the particle to confine the electrons. As in the semiconducting quantum dot case, electronic trajectories exhibit chaos and can be studied statistically with random matrix theory. Agam *et al.* have studied Al particles to explain the clusters of resonances beyond the orthodox Coulomb blockade. The theory of single electron tunneling and the consideration of discrete levels in a metal particle, in addition to the Coulomb blockade, was studied theoretically [9].

Davidović and Tinkham used tunneling transport to observe and explain the reduced g-factors in Au nanoparticles as a result of the strong spin-orbit interaction in Au. Additionally, they observed stronger clustering of levels as the energy was increased [39]. We have observed similar effects in Ni samples that are the result of a different mechanism, in which clusters of resonances in the differential conductance spectra resemble a finite bandwidth.

Previously, our group has also studied the suppression of spin-orbit scattering in granular Au films [5, 6], as well as zero bias anomalies and localization in Au nanojunctions [26]. Additionally, they have measured the effects of spin transport in metallic particles, and the influence of ferromagnetic tunneling leads [21, 22, 150, 151]. Similarly, Deshmukh *et al.* probed discrete states on normal metal particles, using metallic or ferromagnetic leads, and observed nonequilibrium effects [40, 42].

Finally, the notion of the electronic g-factor has been studied extensively both theoretically [2, 31, 38, 125] and experimentally [23, 118, 119] in metal particles. It was found that spin-orbit scattering leads to an effective g-tensor whose magnitude depends on magnetic field direction. Further, the spin-orbit interaction tends to

reduce the magnitude of the g-factor, allows variation of the g-factor from level to level, and leads to avoided level crossing as a function of magnetic field.

1.9 Ferromagnetic Quantum Dots

The importance of single-domain magnets and the promising applications of spintronics and spin-transfer torque have led to much interest in ferromagnetic quantum dots. Theoretically, Barnas *et al.* [14–17] and Brataas *et al.* [27–29] analyzed a ferromagnetic quantum dot along with ferromagnetic leads.

Experimental works on various fronts in ferromagnetic quantum dots, including Dan Ralph's group at Cornell [41, 58], Wernsdorfer's group [70–72, 140, 142, 152], and our group [73–75, 150] have studied the nature of ferromagnetic particles and their quantum mechanical interactions. While much has been explored theoretically on these fronts as well [1, 35–37, 54, 56, 89, 90, 99, 103, 147], there remain many intricacies to be explored in such systems.

1.10 Magnetic Molecules and Electronics

Even further miniaturization of magnetic structures has led to the possiblity for molecular spintronics [11, 24, 62, 104, 111, 126, 127]. However, while there has been progress experimentally in such areas [7, 62], electron transport measurements have found stable hysteresis to be elusive [76]. Van Der Zant's group has experimentally studied different coupling regimes with the conducting lead contacts in gated sample devices [110], as well as the ability to control magnetic anisotropy in single molecule with gate voltage [167, 168]. Finally, Elste *et al.* and Timm *et al.* have conducted master equation simulations in molecular magnets that are similar in form to the simulations I perform in this thesis [46, 144, 145].

1.11 Atomic-Scale Magnetism

With the advent of the spin-polarized scanning tunneling microscope (STM), it has become possible in recent years to study the effects of building up magnetic structures with atomic resolution. A good review of such experimental techniques is provided in reference [153]. Among the researchers at the forefront of such efforts are Wiesendanger's group at Hamburg, Heinrich's group at IBM, and Otte's group at Delft. Wiesendanger's group has studied magnetic atoms and chains adsorbed on a sample surface which interact via direct [85] and RKKY [86] interactions, which contribute to both ferromagnetic and antiferromagnetic atoms and spin chains [64, 84, 87, 94]. Such techniques have also provided the opportunity to study the basic physics of spin friction [156], the effects of different types of magnetic switching in few-atom systems [94], along with the study of exotic topological states known as skyrmions [122, 123]. Further, they have considered a system for realizing spin-based logic in antiferromagnetic spin chains, which rely on geometric frustration [87].

Heinrich's group has probed antiferromagnetic states of few-atom spin chains [97], as well as pump-probe spin relaxation, the Kondo effect in dimer adatoms, and inelastic tunneling spectroscopy [63,66,67,98,112]. Otte's group has studied the manipulation and atomic control of mangetocrystalline anisotropy of an Fe dimer [33]. A common feature of all of these works is that magnetism is highly susceptible to subtle environmental influences, and that the confluence of these different perturbations can lead to novel and non-trivial effects. While the STM experiments mentioned here offer atomic precision and dynamic manipulation, the tunnel junctions considered in my dissertation are relatively static by comparison. That is, once the samples are fabricated in our lab, the tunnel junction spacing and materials are fixed. However, the amount of voltage tuning in our tunnel junctions offer an analogous degree of precision in their ability to tune the coupling of magnetic nanoparticles to their environment. The spin-orbit interaction induced anisotropy energy shifts and Coulomb blockade

are crucial in shielding our samples from undesired environmental perturbations.

1.12 Goals of the Dissertation

In this dissertation, I will explore further into the characteristics of ferromagnetic quantum dots, using sequential electron tunneling spectroscopy. I will present findings on several ferromagnetic materials, including Co and different isotopes of Ni, and find that Ni lies at the stability threshold for stable hysteresis. Measurements of Ni samples display detailed tunneling spectra as as function of magnetic field, and only some samples exhibit magnetic hysteresis. The interplay of various energy scales, as predicted by reference [36], leads to fluctuations in the anisotropy energy when a single electron is added to the particle. These anisotropy energy shifts allow for the emergence of an effect that we denote as magnetization blockade, which allows for the voltage tunable control of hysteresis in nanometer-scale ferromagnets. Additionally, I will show measurements of large electron g-factors observed in the differential conductance tunneling spectra of Co particles, which is due to the collaboration of the spin-orbit and exchange interaction. I will also discuss the intricate spectra of ferromagnetic particles. In Ni particles, this can lead to Zeeman splitting and curvature of levels due to the spin-orbit interaction. Finally, I propose a spin-transfer torque device based on the voltage control of magnetic hysteresis, which could offer improvements and alleviate some of the issues involved with power dissipation in current-driven STT devices.

CHAPTER II

EXPERIMENTAL METHODS

In this chapter, I will discuss some of the various experimental apparatus and procedures utilized by our research group. Some sections are intended to help other researchers to reproduce the work performed in this dissertation, and therefore those readers uninterested in delving into such intricacies may wish to skip ahead to chapter III.

2.1 Sample Fabrication

One challenge to the fabrication of nanometer-scale devices is the size constraint. While the common technique of photo-lithography has been utilized for decades to fabricate microelectronic devices, it suffers from the optical constraint of the wavelength of light. That is, common photoresists that are based on ultraviolet light can generate features on the order of $\lambda/2$, where λ is the wavelength of the light. In order to generate features on the order of 50 nm or less, however, visible or even ultraviolet (UV) light will not suffice. Recently, extreme UV light has been used for lithography, but our lab utilizes a different method [157]. Instead of using light, we can instead use electrons and corresponding e-beam resist. As de Broglie postulated, an electron has a momentum-dependent wavelength λ_e, which can be described by the formula: $\lambda_e = h/p$, where h is Planck's constant, and p is the momentum of the electron. Therefore, the higher the momentum of the electron, the smaller the effective wavelength.

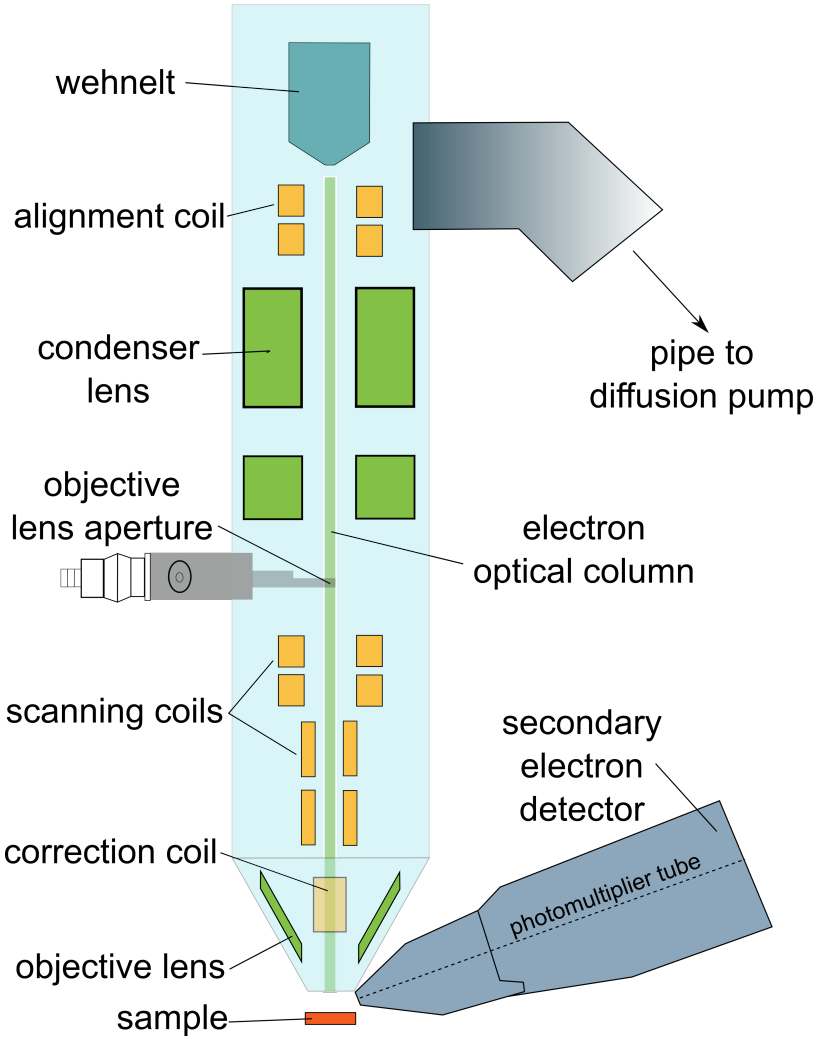

Figure 2.1: Illustration of our scanning electron microscope. Below the objective lens cone is the sample to be imaged, which is controlled by step motors (not pictured).

2.1.1 Electron Beam Lithography

As an alternative to photo-lithographic techniques that use visible or UV light, we instead use electron beam lithography [30]. This requires the use of electron optics, which are analogous to the traditional lenses used in the optics of visible light. Instead of using glass lenses, we utilize electromagnetic lenses, which focus the electrons toward the sample. Our electron optics are encapsulated in a scanning electron microscope (SEM) manufactured by JEOL. The basic configuration of our SEM is displayed in Figure 2.1.

The electrons used for imaging the sample are generated by thermionic emission from a heated tungsten filament. This filament is encased in a conical metal shell known as the wehnelt, which has a small orifice at the apex to allow the emission of electrons in a precise direction. A large potential difference is applied across the SEM column in order to accelerate the electrons towards the sample. Once the electrons are emitted from the wehnelt, they are focused by an alignment coil and a series of electromagnetic condenser lenses, followed by scanning coils and the objective lens. After striking the sample, the imaging electrons excite secondary electrons in an inelastic scattering process. These secondary electrons are ejected from the sample and detected by a collector, scintillator, light guide, and photomultiplier tube. The scanning coils deflect the electron beam to allow it to scan across the surface of the sample rapidly in a raster scan.

Because electrons react strongly with matter, the imaging system and sample chamber of the SEM must be kept in a high vacuum, in order to reduce the risk of electron scattering events with gas molecules over the length of the microscope. In our system, this is accomplished by using a rotary pump and diffusion pump in series, which are able to evacuate the specimen chamber to a high vacuum of 1×10^{-6} mbar(≈ 0.1 mPa) in less than 10 minutes. The rotary pump maintains a low pressure on the exhaust end of the diffusion pump. Once this high vacuum level is achieved in the specimen chamber, the electron beam can be turned on. A routine calibration process must be practiced each time the specimen chamber is opened.

As with visible light optics, the imaging system of electron optics suffers from various aberrations such as spherical aberration, chromatic aberration, and astigmatism. Spherical aberration occurs when the electrons further off axis radially experience more deflection than electrons closer to the axis. It results in image nonuniformities known as barrel and pin cushion distortions. Chromatic aberration arises in light optics due to dispersion and the fact that light of different wavelengths experience

Figure 2.2: Photograph of Scanning Electron Microscope that I use to image samples and conduct electron-beam lithography. Optical column is open at the top during a routine filament replacement. The silver cone is the wehnelt.

slightly different focal lengths, and for non-monochromatic sources, this causes a blur along the optic axis near the focal point. In electron optics, the de Broglie wavelength of the electron depends on the electron's momentum. The generation of imaging electrons from the filament begins with the fact that electrons are in thermal equilibrium with the filament. These electrons will therefore exhibit a spread in velocities given by the proper probability distribution. The current density J of the electrons flowing from the wehnelt can be approximated by $J = AT^2 \exp(-E_w/k_B T)$, where A and E_w (the filament material work function) both depend on the material composition of the filament.

The important point is that this distribution of velocities has a non-zero variance, and so the imaging electrons will contain a spread in momentum values. This spread in momenta results in a spread in effective wavelengths of the electrons, or a non-monochromatic electron optics source, which is susceptible to chromatic aberration.

Astigmatism is the common optical aberration due to lenses having different focal lengths along two orthogonal directions that are transverse to the optic axis. We observe astigmatism regularly when imaging with the SEM, and fortunately the SEM contains an 8-pole electromagnetic lens that can be finely tuned each time we image a sample. This is referred to as stigmator, and can be used to correct for astigmatism. During the initialization process of the SEM, we move the sample stage to the calibration region of the sample mount, which contains gold standard nanoparticles of a known shape. We zoom the magnification to levels between 50,000× and 100,000× and adjust the focus parameter until the nanoparticles are in the focal plane. To check for astigmatism, we use the fine-focusing feature to shift the focal plane above and below the height of the nanoparticles. If the particles begin to blur uniformly in all directions as the focal plane is adjusted, then the astigmatism is negligible at this stage. However, if the particles begin to distort and elongate preferentially along one

direction as we change the focal plane, this is an indication that astigmatism is prevalent. To fix this, we adjust the x- and y- stigmator feature when the nanoparticles are slightly out of focus. This should compress the image along the elongated direction. We then bring the particle plane back into focus and defocus in the opposite direction. If there is elongation of the particles along a different direction, we continue to adjust the x- and y- stigmator iteratively until the image blurs isotropically as the focal length is varied.

As with the focus calibration procedures, a careful routine should also be followed when replacing the filament. If the filament burns out in the middle of an electron-beam lithography writing procedure, or during the imaging calibration steps, a notification will alert the SEM user on the computer screen. If this occurs, users should wait a few minutes for the system to cool down before attempting to replace the filament. As always, a clean pair of gloves must be donned before touching anything near the open SEM chamber. Once the specimen chamber is vented to atmospheric pressure and the wehnelt has cooled off, the top of the optical column can be opened, as is shown in Figure 2.2. Then the wehnelt and filament can be carefully removed, and the top of the optical column should be closed to avoid letting any dust or debris into the SEM.

To remove the filament from the wehnelt, the three mounting screws can be loosened, and the broken filament should be inserted into the case of used filaments, and marked with the current date. There is a ring with three dashes that keeps the tungsten filament a certain distance from the wehnelt tip. However, before the filament can be replaced, the wehnelt and ring need to be cleaned. Wooden sticks (as from a cotton swab) with metal polisher can be used to clean the inside of the wehnelt. The stick might need to be broken to fit into the crevices of the wehnelt. The wehnelt should be cleaned with sterile lab wipes, and all of the residue and burn marks should be removed. This process typically takes 15 or 20 minutes. Next, the wehnelt should

be wiped and cleaned with acetone, followed by its placement in a beaker with 50/50 isopropanol(IPA)/acetone mixture to be ultrasonicated for 30 minutes. The wehnelt should immediately be transferred to a second ultrasonicated bath of pure IPA, and then sprayed clean with IPA. Finally, the wehnelt should be dried with compressed air under the fume hood. At this point, some of the screws might have been jostled free during the ultrasonication process, so the wehnelt should be inspected before proceeding. Next, the ring can be inserted, followed by a new filament, with the filament notch 180° degrees away from the notch in the wehnelt. The filament filament should be visually inspected through an aperture in the tip of the wehnelt, to ensure that the filament is centered. Realignment and centering can be accomplished by adjusting the relative tightness of the mounting screws that position the filament within the wehnelt. Finally , the SEM optical column can be opened, and the new filament can be inserted.

Now, the new filament needs to be calibrated and adjusted to ensure proper imaging and long filament life. To accomplish this, insert a sample holder in the specimen chamber that has a Faraday cup. Pump the specimen chamber to high vacuum and turn on the SEM beam.

Increase spot size to 40 or 50 (in spot size units on screen) to get more accurate current readings, and zoom into the Faraday cup in order to read out the total current from the imaging electron beam. On the gun menu, increase the L.C. parameter (which stands for load current through the filament), and you will see one peak in current followed by a sudden drop. Keep increasing the L.C. until a plateau is reached in the ammeter. The plateau has been reached when the L.C. is increased and the output current goes up by only one part in one hundred. If the current value is stable, adjust the beam position coordinates iteratively to maximize the current output. A lens reset might be necessary if the current becomes unstable. This is typically due to charge buildup in the column and the lens reset will clear the unwanted charge away.

If the filament tip in the wehnelt is well-centered, all of the maximized parameters (x, y, tilt/shift) should be close to the center marks as well. Lower the spot size, and readjust alignment parameters.

Another issue to address in the electron beam lithography process is the nature of the sample substrate. If the substrate is strongly insulating electrically, then the flux of the charged imaging electrons on the substrate causes a buildup of charge, which distorts the path of the later electrons. This leads to the distortion as shown in Figure 2.3(a). To alleviate this issue, we spin-coat a conductive polymer layer on top of the electron photoresist methyl methacrylate/polymethyl methacrylate (MMA/PMMA) bilayer, just prior to placing the sample in the SEM chamber for lithography. This polymer layer is called ESpacer, and it is expensive so it should be used conservatively. Figure 2.3(b) and (c) display the same contact pattern that was attempted in Figure 2.3(a), but pre-treated with ESpacer. This allowed the quick dissipation of charge during the writing process, and therefore avoided the striped distortion issues shown in Figure 2.3(a).

2.1.2 DesignCAD and NPGS

In order to efficiently automate the process of fabricating many samples at once, we first specify and draw the sample geometry using a specific computer-aided-design program called DesignCAD. This program interfaces with a numerical control system and the SEM in order to generate sample geometries to our exact specifications, without the need for lithographic masks. The numerical control software we use is called Nanometer Pattern Generation System, or NPGS. NPGS controls the step motors, the magnification, and electron beam blanker in the SEM chamber, and is thus able to rapidly expose sections of the sample substrate in the desired geometric pattern with an accuracy of approximately 50 nm for our setup. Figure 2.4 displays the process of drawing sample contacts in DesignCAD, and using NPGS in the SEM

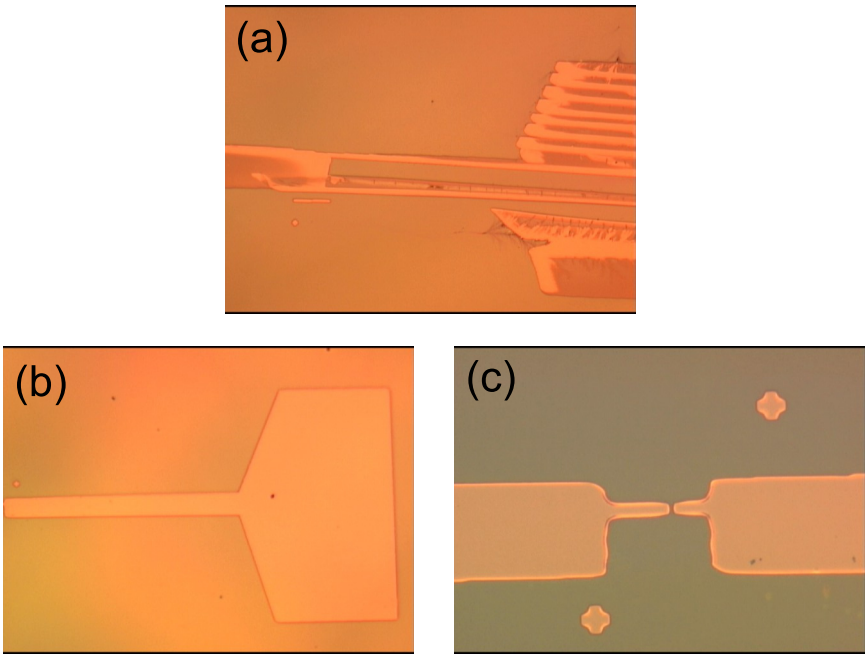

Figure 2.3: Optical images of contacts made by electron-beam lithography. (a) Charge buildup problem on insulating substrate distorts electron-beam writing process. (b),(c) display different magnifications of sample with conducting ESpacer pre-applied to substrate.

to deposit metallic contacts.

2.1.3 Vacuum System and Metal Deposition

After the sample substrate has undergone electron-beam exposure, we develop the chip in a solution of methyl isobutyl ketone (MIBK) and isopropyl alcohol (IPA) in a volume ratio of 1:3 for MIBK:IPA. After submerging the sample chip in the MIBK/IPA solution for one minute, we wash the surface of the chip with pure IPA for ten seconds and then use dry air to blow the surface dry. At this point, the sample chip still has a MMA/PMMA bilayer over most of the surface, but the areas that were exposed to the electron beam have been washed away in the chemical development process. This leaves a series of trenches in the MMA/PMMA bilayer that reach to the surface of the chip. After inspecting the geometry of the trenches with an optical microscope to ensure that there were no misalignments during the electron beam patterning process, we place the chip on a rotating state and mount the stage in a

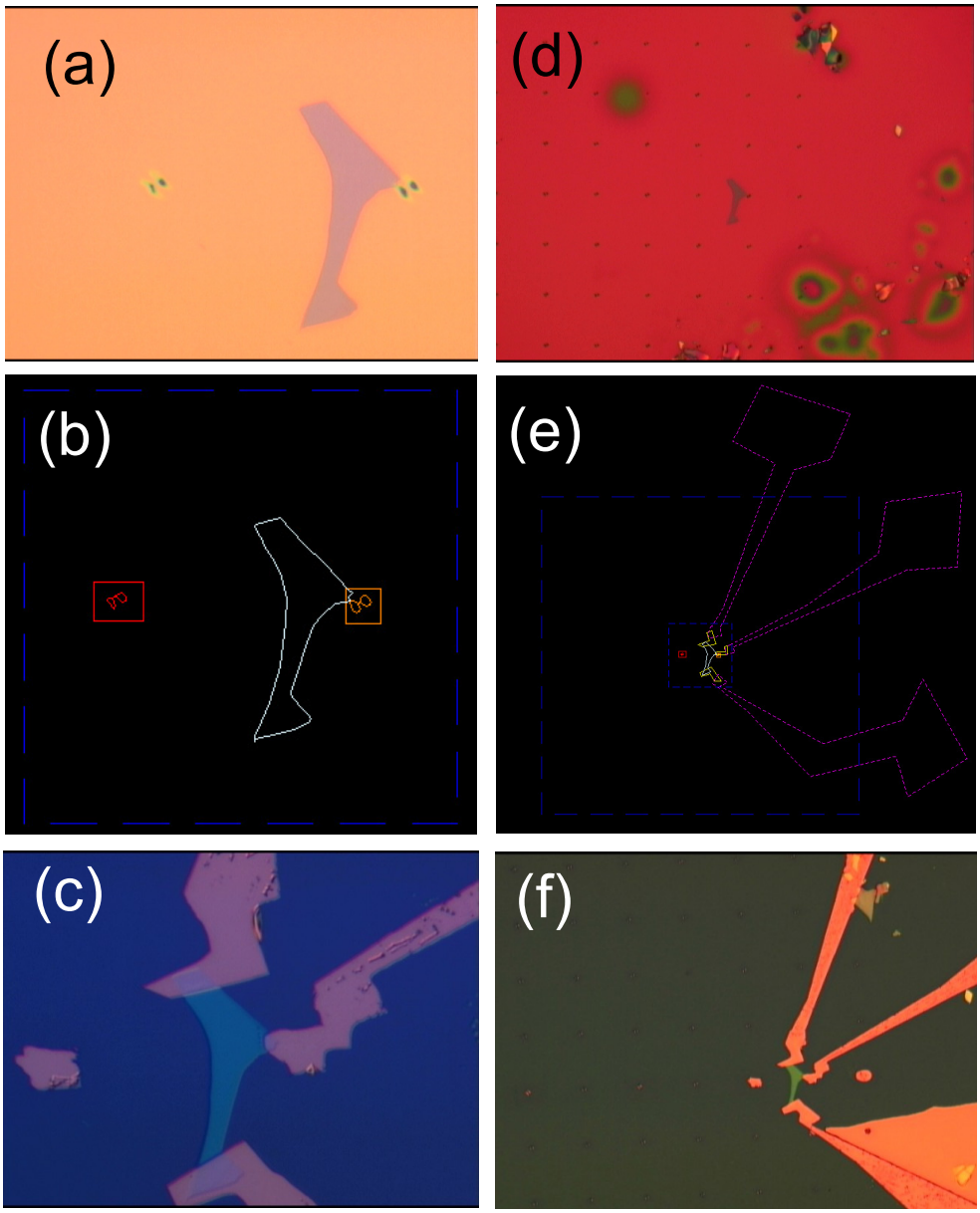

Figure 2.4: Optical images and DesignCAD files showing example of electron beam lithography process with two magnification levels. (a),(d) Few-layer sample of MoS_2 on a SiO_2 substrate. (b),(e) DesignCAD image used for alignment in SEM. (c),(f) deposited Au contacts on MoS_2 sample. The larger dashed-blue squares in (b) and (e) have a side length of 90 μm and 450 μm, respectively.

vacuum chamber, as depicted by the schematic in Figure 2.5. Under the inverted stage, we can connect up to three metal boats. These boats contain a bowl-shaped region covered with an insulating material into which we can place different metal materials for use in the evaporation and sample deposition process. The boats are

secured in position with large copper electrodes, which can drive large currents and induce Joule heating of the boat. This causes the metal pellets to melt, if enough power is transferred through the boat. However, this evaporation process must be performed in a high vacuum ($\sim 10^{-7}$ torr) in order to avoid possible contamination between the deposited layers.

When the chamber is pumped down to low pressures, the partial pressure of the surrounding gas is substantially reduced, and the melted metals evaporate into the chamber. When the evaporated metal reaches the walls of the chamber or the sample chip, it condenses on the cool surface and forms either a thin film or a collection of nanoparticles, depending on the thickness of the deposited layer. We measure the amount of metal that reaches the sample by use of a quartz crystal deposition monitor. The principle of operation of such a deposition monitor relies on the fact that the resonant frequency of a piezoelectric material such as quartz changes based upon the addition of adsorbed mass on an outer layer of the crystal. Through material calibration parameters (such as density), we can therefore determine the amount of metal deposited on the surface of the crystal in a very accurate manner based upon the precisely measured frequency shift of the resonant (low-impedance) response of the crystal to an applied electric field. If we assume a uniform angular distribution over small solid angles in the chamber, then the thickness of material is approximately constant over the surface of the crystal. However, the thickness of material deposited on the crystal will not in general be the exact same thickness as is deposited on the sample chip, since the crystal is displaced from the sample chip. That is, the sample chip is mounted vertically above the evaporation boat, while the crystal deposition monitor is positioned at the same height, but at a horizontally displaced position. We can correct for this difference by calibrating the amount of material deposited on the chip and comparing it with the thickness measured by the crystal monitor. This ratio is defined as an appropriate tooling factor, and is included in the metal deposition

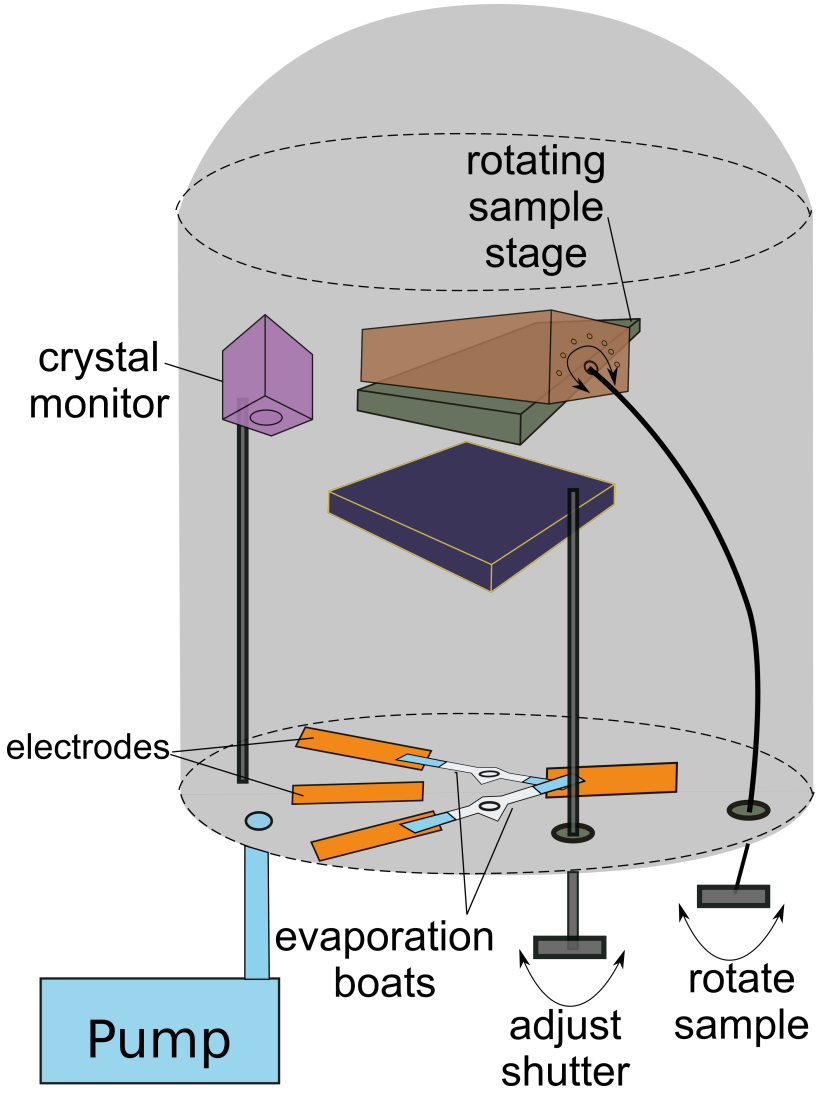

Figure 2.5: Illustration of the vacuum chamber in our lab. A cryopump reduces the pressure in the chamber to 10^{-7} torr in order to perform thermal evaporation and deposition of metallic layers on the samples etched by electron beam lithography.

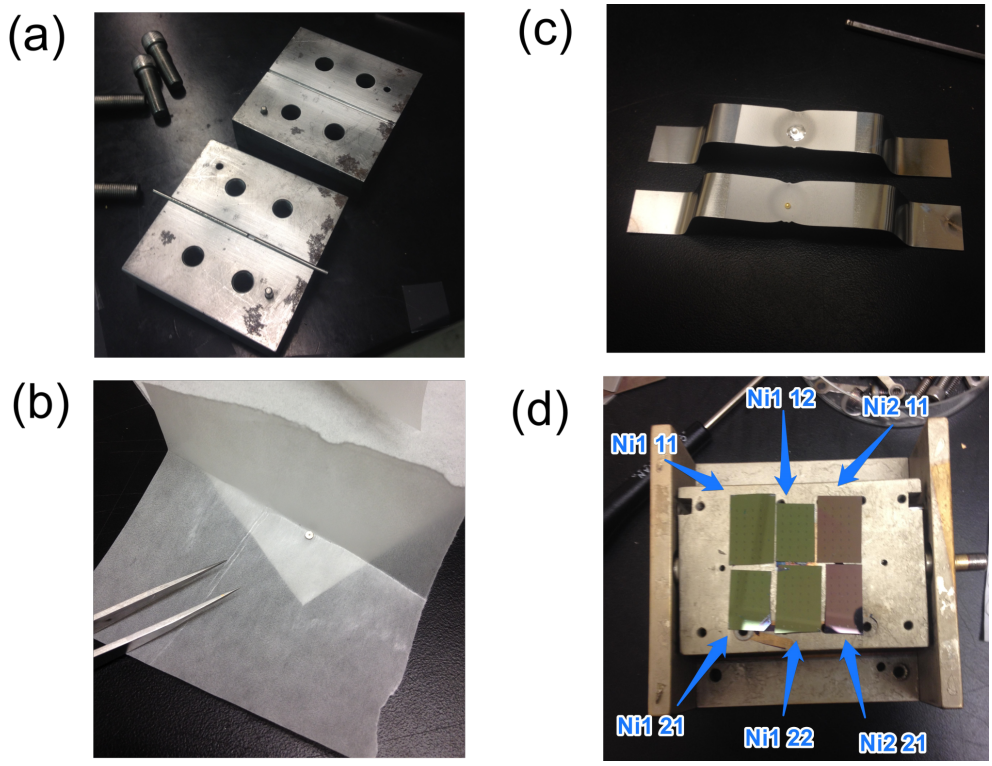

Figure 2.6: (a) Apparatus used to sinter Ni powder into a pellet form. (b) Sintered pellet on wax paper. (c) Evaporation boats used in the vacuum chamber, containing Al and Au that were used to deposit nanometer-scale films. (d) Array of sample chips about to undergo metallic layer deposition, held on rotating sample stage. Numbers refer to sample and fabrication batch numbers.

process. The thickness calibration can be performed in various ways. In our case, we deposited a large amount (hundreds of nanometers) of material on a substrate, and used an atomic force microscope to compare the deposited region with the normal substrate.

The deposition of specific materials on our samples requires the acquisition of metals in solid pellet form, rather than a powder. While this is easily accomplished for a wide variety of materials, we ran into some difficulty when trying to evaporate a rare and expensive isotope of nickel, ^{61}Ni. The only way to purchase this isotope of Ni was in a fine powder form. In order to remedy the situation, we used an apparatus to compress the powder into a solid piece through a sintering process, the steps of which are depicted in Figure 2.6.

2.1.4 Wiring the Sample Chips to a Mount

Once the samples have undergone the metal deposition process, we place the chip in an acetone bath in a glass Petri dish for 20 minutes. The temperature is elevated to 40° C, and the dish is topped loosely with a second glass Petri dish to avoid evaporation of the acetone. Next, we spray the surface of the chip with acetone, then isopropyl alcohol before the surface dries, and the remaining metal layers are washed away with the MMA/PMMA bilayer. What remains are the patterned devices on the surface of the chip. However, at this point, we still need to connect the contact pads of the devices to an external circuit. We accomplish this by first fabricating a plastic mount to which each tunnel junction sample will connect. We make each of these sample mounts by etching a copper plate with ferric chloride, and then soldering large contacts on one edge of the mount. Each of these contacts is connected to microtech contacts, which in turn are connected to a dipstick. A set of old completed samples that have already undergone measurement in the dilution refrigerator are depicted in Figure 2.7. When placing the sample chips on the sample mounts, we apply indium solder with a needle probe (by hand) to copper wire, and connect the copper wire to the larger solder contacts on the sample mount.

2.2 Measurement Process

Most of our measurements involve evaluating the current response to an applied bias voltage. Due to the energy scales involved in our measurements, low temperatures are essential. Therefore, many of our measurements are performed either in a liquid helium bath (which corresponds to a temperature of 4.2K) or in the dilution refrigerator (which uses a mixture of two isotopes of helium to achieve temperatures as low as 0.03K in our setup). Below, I will give a basic summary of the principle of operation of a dilution refrigerator, and the basic routines for running our particular apparatus.

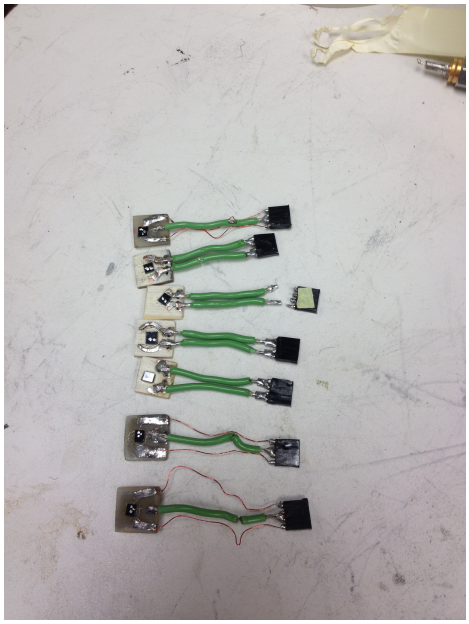

Figure 2.7: Samples that have already undergone measurement in the dilution refrigerator.

2.2.1 Dilution Refrigerator

The basic principle of a dilution refrigerator is similar to that of a conventional refrigerator, except that the refrigerant is a mixture of the two stable isotopes of helium, ^{3}He and ^{4}He. At low temperatures, there is a spontaneous phase separation of the two isotopes, as is depicted in the schematic in Figure 2.8. The heavier, ^{4}He phase and the lighter, ^{3}He phase separate spatially. However, even at absolute zero, there is still a finite amount of 'dilute' ^{3}He within the ^{4}He region, from whence comes the name 'dilution refrigerator'. When ^{3}He crosses the phase boundary between the ^{3}He-rich phase and the ^{3}He-dilute phase, it requires energy, in the same way evaporating water requires latent heat of vaporization. The energy for such a phase change is supplied by the surroundings of the mixing chamber, including the sample. This allows the sample to cool to approximately 0.03 K, if the superconducting magnet is turned off, or about 0.06 K if the magnet is running.

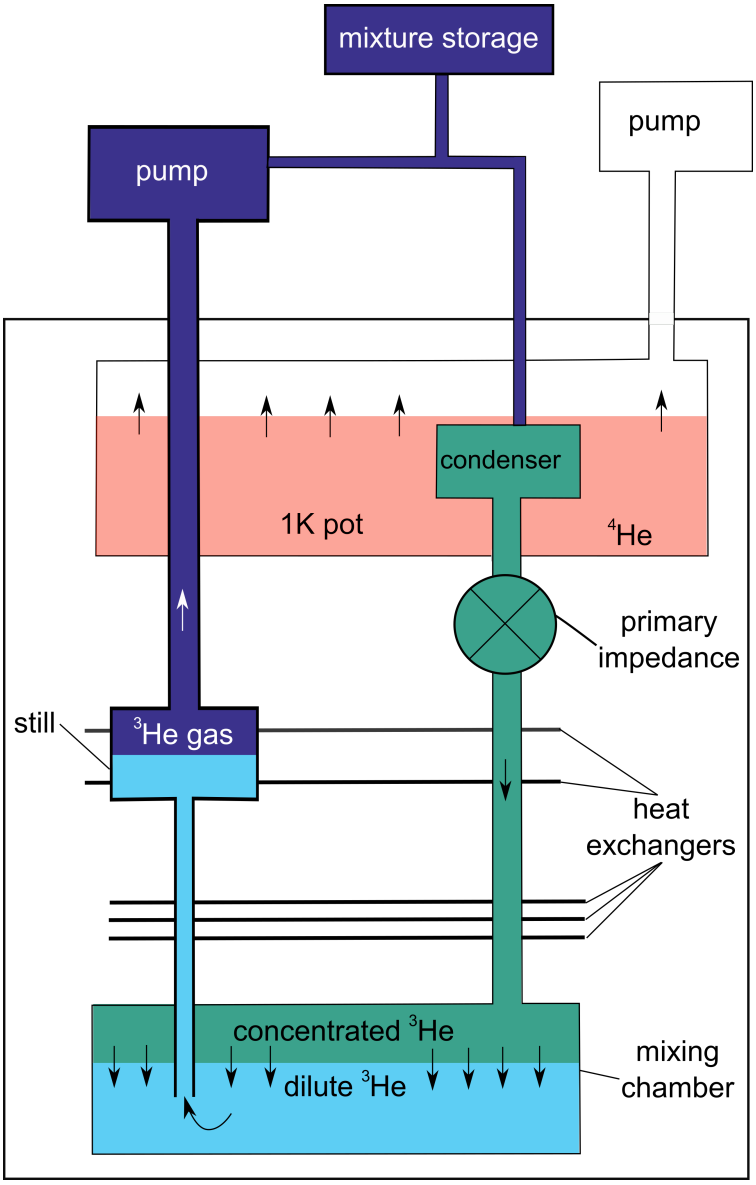

Figure 2.8: Dilution refrigerator principle of operation. There are two separate circulation systems. One includes the 1K pot which contains liquid ^{4}He (red in figure), and is pumped to maintain a temperature of approximately 1.5K. The second, main circulation system consists of the ^{3}He/^{4}He mixture, which passes through the condenser and the primary impedance. A phase boundary between the ^{3}He-rich phase (green) and the ^{3}He-dilute phase (blue) is set up in the mixing chamber. Flow of ^{3}He across the phase boundary cools the sample. Extra ^{3}He from the dilute phase is preferentially evaporated by the still heater and pumped away (purple), to begin the circulation again.

2.2.2 Pre-Cooldown Procedures

Because of the high cost of liquid helium (particularly ^3He for the mixture, but even ^4He is quite costly), it is best to make the most efficient use of time and resources in preparation for a dilution refrigerator cooldown, including the fabrication of many samples and the proper testing of the dilution refrigerator. Prior to the cooldown, pump out the still line and the condenser line overnight using the turbopump. On the dipstick, perform a leak check using the He leak detector and by spraying He gas near the joints of the dipstick where we replaced the indium seals.

Then, if there are no leaks, ground yourself at all times with the large resistance bracelet and attach the sample holders and check to make sure they are all working. Once this is performed, seal up the sample holder with the copper cylinder, and put a little apiezon grease around the ridges in order to keep it lubricated. Otherwise, copper against copper can fuse together. At this point, it is good to check the viability of the samples again.

When the fridge starts off hot, the liquid nitrogen cold traps need to be cleaned. This can be done in the following manner. Make sure the manual valve to the inner vacuum chamber (IVC) and outer vacuum chamber (OCV) is closed. Put a cap on the main bath tube. Note, these are labelled behind the control apparatus in the shield room. You will want to use the heat gun on the nitrogen cold trap to heat it up a lot (above 100°C). Open valve 11A, then 2, then 7. As you do this, the pressure reading on gauge G1 will increase (if valve 2 is open to connected the cold trap to the trap). Then, turn on the ^{4}He rotary pump, and open valves 5A and 2A. Because the vent ports are all connected to the same place, the final opening of valve 2A connects the ^{4}He rotary pump to the line connecting the Ni cold trap. Continue heating the trap with the heat gun for a few minutes, then close valve 11A which will seal off the Ni cold trap. Then, close valves 2 and 7. Last, close valves 2A, then 5A, then turn off the ^{4}He pump.

The next step is sealing the inner vacuum chamber. Once the inner radiation shield has been attached to the dipstick and the holes have been covered with metal tape, it is time to heat the sorb with the heat gun, apply the indium wire seal, and then seal the IVC. Then the IVC line should be evacuated with the turbo pump for at least an hour. Next, perform a leak test using the He leak detector. If no leaks are detected, you can insert the He exchange gas in the IVC. Be sure to use the T shaped pipe adaptor with the helium gas line attached to the nozzle on one side, and the turbo pump line on the other. The small port will attach to a small valve, which attaches to the IVC line. Be sure to insert the copper cylinder inside the bottom of the small valve where it connects to the IVC. This allows a specific quantity of He exchange gas to be placed in the IVC to help the dipstick cool down. Then, pump with the turbo pump's roughing pump with the small valve open. Flush with helium gas then turn gas off and keep pumping with the turbo pump's roughing pump. Then switch off the electronic valve on the turbopump to disconnect it from system. Turn on the gas and then seal the small valve. Open the IVC valve for a second to admit exchange gas, then close it. Then remove the fitting from the dipstick and cap seal the IVC port. You also need to pump out the transfer line with the turbopump overnight.

When the dipstick is ready, attach the fiberglass shield and carry it over to the Faraday cage shield room and attach it to the wench on the ceiling. Use caution and raise it up and watch that the wire doesn't snap or hit the ceiling. It has very little leeway and will just have less than a centimeter to be raised over the fridge and slid into place. Then, slowly lower the dipstick and make sure the alignment markers are overlapping in each marked location.

Again, because of the high cost of Helium, the dilution refrigerator should first be cooled from room temperature down to $\sim$ 77K using the much less expensive liquid nitrogen. This procedure can be achieved as follows. Make sure that the port to the

fridge (exhaust) and the port to the dipstick fiberglass attachment are OPEN (that is, don't attach any one-way valves or anything like that). Then attach the nitrogen transfer line with the fridge link attachment, rough side towards the rubber hose. This will be slid into place in the cone in the bottom of the fridge, through the same port where the helium transfers take place. Slide the rod into this port, and watch for the piece of tape near the top of the rod— this marks where to slow down and feel for the placement of the rod in the cone. Once it is in place, open the nitrogen line valve from the dewar and allow the built up pressure in the dewar to transfer the liquid nitrogen into the fridge. Note that if the transfer rod is in the cone, the transfer process will be slower due to the flow impedance of the cone and this narrow region. This process takes about two hours. Once the exhaust gas (outgassing) of the fridge is cold, it won't be too much longer before the fridge is full, so keep an eye on the fridge. When liquid nitrogen starts spewing out of the exhaust port, turn off the faucet on the dewar and use the heat gun to warm the rubber hose to allow it to be bendy enough to remove the transfer rod from the fridge. Note that right *after* this is the time to apply the two one-way valves to the fridge— one to the exhaust port and one to the fiber glass attachment port. If you put the valves on previously, then the outgassing of the nitrogen will cause the liquid to spew out of the transfer port right as you are trying to remove the rod. To avoid this, wait until after removing the rod and capping this area to put on the one way valves. The flanges will probably be cold and caked with ice, so you might need to apply the heat gun around the exhaust ports before attaching the one-way valves. Typically, the liquid nitrogen will need to cool the fridge for a few hours (preferably overnight).

Before cooling the dilution refrigerator with liquid helium, the liquid nitrogen must be evacuated; otherwise, it will freeze due the low temperature of liquid Helium (and it will waste some or all of the liquid helium in the process). This is done by attaching the transfer line to the nitrogen dewar again, but this time it is crucial to

insert the transfer rod into the cone. If this is not done, then you will not be able to evacuate all the nitrogen since the cone is connected to a pipe leading to the bottom of the fridge. Remove the one-way valves, then insert the transfer rod.

Attach the adapter nozzle to the exhaust port of the fridge, and attach the other end to a cylinder of ultra high purity (UHP) Ni gas. Then, open the vent port of the nitrogen dewar and cap the fiber glass exhaust port.

Then open the liquid valve of the dewar and turn on the nitrogen gas to force the liquid out of the fridge and back through the transfer line into the dewar.

Once all of the liquid nitrogen has been evacuated, the liquid helium transfer can begin. The liquid helium transfer, and the process of cooling the mixture of Helium isotopes is very complicated, and is best only performed with an experienced advisor or senior graduate student to supervise. The particulars of the helium transfer and mixture circulation are available in the Oxford Instruments instruction manual for our dilution refrigerator.

2.2.3 I(V) Curves and Magnetic Field Sweeps

Once the liquid helium has been transferred and the mixture is properly circulating, the fridge should reach a base temperature of approximately 0.03 K. Once this occurs, the low-temperature data collection can begin. To further shield the samples from extraneous interference due to ambient electromagnetic signals, we surround the entire dilution unit in a copper-lined Faraday cage room. Measurement signals are fed into the shield room via a filter box. Inside the dilution refrigerator is the superconducting magnet, which we utilize for applying a magnetic field as large as 12 T. The superconducting magnet is a solenoid that is placed in thermal contact with the 4.2K liquid helium bath during operation. Note, some care must be taken when operating this powerful magnet. The power supply given by Oxford Instruments allows setting a linear field sweep with an initial and final value, and a step size. In order to change

the current flowing through the superconducting magnet, a small portion must be heated in order to change the magnitude of the current through the coil. It is crucial that the leads are driven normal by a heater before the magnetic field is swept, so as to match the applied current with the persistent mode coil current. If this is not taken into account, and there is a mismatch between the applied current and the coil current, the coil will undergo a quench. This means that the whole coil suddenly has a finite resistance, and dissipates power, heating the liquid helium in its vicinity. This can quickly boil off and waste a significant amount of helium in the dilution refrigerator, and will fill the shield room with helium gas.

The $I(V)$ curves we measure as a function of temperature and magnetic field are evaluated as follows. First, we apply a bias voltage via a function generator through the tunnel junction. The output current of the tunnel junction is grounded through a current amplifier, which yields a measurement with sub-pA resolution. Both the applied bias voltage and the resulting current are measured using a data acquisition board from National Instruments, which in turn is connected to a computer on which we collect and store data with a Labview program.

2.3 Finding Hysteresis at the Stability Threshold in Ni Particles

In the process of measuring magnetoresistance of Ni particles at 4.2 K, we were surprised to find no hysteresis in any of the sample batches. Even though much work has been done previously on cobalt nanoparticles of similar size, in those works the observation of hysteresis was always quite clear, even at 4.2 K. We were curious why we could not observe hysteresis in a Ni nanoparticle, and thought the result required further study. Therefore, we systematically varied many experimental parameters, such as isotopic content and Fe impurities. In addition to studying these different parameters, it was also a matter of experience and refinement of our skills that led to the observation of magnetic hysteresis in a Ni nanoparticle in a narrow bias voltage

and temperature range.

We believed that the lack of hysteresis in nickel samples (juxtaposed with the robust ferromagnetism in cobalt samples) required investigation and therefore motivated us to determine the cause behind this suppression of stable ferromagnetism for different ferromagnetic materials.

First, we posited an effect from nuclear spin. Common isotopes of Co have nuclear spin 7/2, but common isotopes of Ni have zero nuclear spin. Therefore, we thought it was plausible that there could be a hyperfine relaxation mechanism present in cobalt which allowed an excited magnetization to relax toward a stable direction (and thus allow multiple stable magnetization directions and hysteresis). To test our theory, we fabricated samples of Ni isotope ^{61}Ni, which possesses an intrinsic nuclear spin of 3/2. We performed the same hysteresis measurements on ^{61}Ni samples at 4.2 K, but found the same results as with common-isotope Ni; that is, there was no visible hysteresis. Thus, we determined that the nuclear spin mechanism was not the primary driving force behind absence of magnetic hysteresis at 4.2 K in nanoparticles of the size we were considering.

Next, we considered the effects of shape anisotropy in the nanoparticles. Co has a higher saturation magnetization than Ni and therefore a greater shape anisotropy energy for two particles of the same size but different material composition. Therefore, we posited that the high shape anisotropy energy of cobalt established a larger energy barrier between stable magnetization directions, thereby fortifying Co more strongly against the effects of magnetization perturbation by coupling to electron transport and other environmental influences. To test our hypothesis, we performed hysteresis experiments on different magnetic materials with different saturation magnetization values. We fabricated Fe nanoparticles and permalloy ($Ni_{0.8}Fe_{0.2}$) nanoparticles of the same size as particles in the initial hysteresis measurements as cobalt and nickel. We found that all the Fe samples displayed hysteresis at 4.2K, and that about half

of the permalloy samples displayed hysteresis at 4.2K. The magnitude of saturation magnetization, and, correspondingly, the shape anisotropy strength, increases from Ni to permalloy to Co to Fe. Similarly, the percentage of samples of a given material that show hysteresis increases monotonically from Ni to permalloy to Co to Fe. We therefore concluded that shape anisotropy is the primary mechanism behind stable magnetization and therefore hysteresis in nanoparticles of this size at 4.2K.

Next, we studied Ni samples in the dilution refrigerator, which has a base temperature of 30 mK. When a constant magnetic field is applied to samples in the dilution refrigerator, the temperature is typically at 30 mK. However, when the magnetic field is swept to different values (e.g., during hysteresis measurements or for magnetic tunneling spectra measurements), the temperature rises to values between 60 mK and 80 mK. Initially, the differential conductance spectra vs. magnetic field of nickel samples did not show hysteresis at 60–80 mK or below, unlike the previous experiments we performed on cobalt samples at 60 mK.

Because our nickel samples were not showing hysteresis, we added a ground plane on-chip filter, in order to reduce effects from environmental noise. Even though the temperature of the electrons on the particle remained between 70 and 80 mK (as measured from the energy spectrum level widths full-width-half-maximum) there could still have been a larger effective magnetic temperature (magnetic excitations) due to stray microwaves coupling to the particle. These microwaves can excite the particle magnetically, but, due to the time scales involved, may not be able to couple strongly to the electrons in the leads and appear in our temperature readings. Similar effects have been observed in single electron transistors [146] in the observation of superconductivity suppression, even when the electron temperature is low. A silver paint, sealed on-chip Faraday cage was required, in addition to cryogenic filtering, to observe the full parity effects of superconductivity.

While we are uncertain of the exact mechanism that ensures the presence of hysteresis in a given sample, we can surmise that the likely explanation for the lack of hysteresis in most Ni samples is due to the weak shape anisotropy of Ni in comparison to Co. The weaker energy barrier between different magnetization directions in Ni with respect to Co makes Ni more susceptible to environmental perturbations (such as thermal effects, high-bias voltage non-equilibrium effects, and stray electromagnetic coupling effects). Any of these perturbations may be enough to excite the magnetization of Ni across a barrier that separates two stable magnetization directions. If the required excitation energy is low, (i.e., if the anisotropy energy barrier is low) then the magnetization direction can easily explore all of the directional phase space available to it instead of remaining localized in a stable equilibrium position. Additionally, our master equation simulations will show that hysteresis is not guaranteed, as it depends on the mesoscopic details of the particular nanoparticle.

To consider whether the voltage bias was too high for stable hysteresis, we note that some of our Ni particle samples measured at 60 mK did not display any hysteresis even though the Coulomb blockade voltage was low (8.9 mV and 2.5 mV for two other samples). In our updated model based upon the master equation simulations, we have shown why it is possible (and likely), based upon the mesoscopic variations among the different particle Hamiltonian parameters from sample to sample, that many Ni samples will not display hysteresis, even for the lowest bias values.

The effect of bias voltage history on magnetic hysteresis is further discussed in chapter V, from which we learned that the magnetic hysteresis in the spectra can only be measured only in a narrow range of voltage, which includes the Coulomb blockade region.

The temperatures of the electrons in the leads can be estimated from the width of the energy levels in the tunneling spectra data at high magnetic field. However, the temperature of the electrons in the leads is always of the same order of magnitude,

regardless of whether there is a filter present, and has been measured over many trials. Therefore, we do not believe the electron temperature can explain the presence or lack of hysteresis. As mentioned previously, magnetic temperature might be expected to rise even in the case when the electronic temperature has not increased.

There is a loss of magnetoresistance contrast at the expected switching field for higher temperatures than 2.3 K. We cannot unambiguously discern reproducible magnetic switching events at the higher temperatures. This doesn't necessarily mean that hysteresis is lost above 2.3 K. We do not have the data to confirm the status of hysteresis above that temperature. Our estimation of the blocking temperature is based on extrapolation.

In chapter V, I will further detail the process of the findings of hysteresis in a representative Ni sample. There, I note that five Ni samples were measured in the dilution refrigerator. These samples were from a batch of five identically prepared Ni samples of which two showed hysteresis. Here, I wanted to make a fair comparison between samples since there were many possible parameters that could be varied (isotope, ground plane filter, temperature range, Coulomb blockade width, material composition). It would be quite complicated and infeasible to compare samples with so many different parameters. Therefore, those different samples are not counted among those considered in that chapter.

CHAPTER III

COMPUTATIONAL METHODS

3.1 Introduction

In this chapter, I will summarize some of the simulations and computational techniques I used in modeling and interpreting the experimental data. As mentioned previously, the primary type of simulations I employed are two different implementations of solutions to the master equation. I will briefly review random processes and how we can use a particular stochastic realization to model the time evolution of the eigenstates of the magnetic particle. I will also describe the spin-dependent tunneling density of states, and explain how it is a useful quantity for understanding a specific Hamiltonian and its tunneling and magnetic characteristics.

3.2 Tunneling Density of States

During the sequential tunneling process, the particle Hamiltonian alternates between two phenomenological magnetic Hamiltonian operators, H_0 and H_1, corresponding to the N and N+1 electron particles:

$$H_0 = -KS_z^2/S_0 + 2\mu_B B S_z, \text{ and}$$

$$H_1 = H_0 + \epsilon \left[\cos\theta_{\mathrm{SE}} S_z + \sin\theta_{\mathrm{SE}} S_x\right]^2 / S_0^2 + \epsilon_z S_z^2/S_0^2 + E_0.$$

For the simulations studied here, we assume that H_0 is characterized by a uniaxial anisotropy with coefficient K and a Zeeman energy term. Similarly, we assume that the N+1 electron particle is characterized by the same uniaxial anisotropy and Zeeman terms, along with an additional term due to the spin-orbit energy anisotropy shifts ϵ and ϵ_z. Here, θ_{SE} is the angle relative to the initial easy axis of the ϵ anisotropy term. Such shifts depend on the orientation of the magnetization, as predicted by

reference [36]. E_0 is the constant offset energy due to the charging energy of one extra electron. In the following three figures, the Hamiltonian parameters chosen were $S_0 = 100$, $K = 10$, $\epsilon = 200\mu$eV, $\epsilon_z = -200\mu$eV, $\theta_{\rm SE} = \pi/6$, and $E_0 = 1$ meV. One useful tool for observing the characteristics of a given tunneling Hamiltonian is a spin-dependent tunneling density of states (DOS). We define

$$DOS(S_z, E) = \sum_{\alpha} |\langle N, S_z | N+1, \alpha \rangle|^2 \; \delta(E_{N+1,\alpha} - E_{N,S_z} - E).$$

The δ-functions are broadened by convolving with a Gaussian of width 1μeV. Such a structure displays the energy weights corresponding to specific transitions between the two different particle Hamiltonians as a function of the spin projection along the easy axis of the particle, for the $N \rightarrow N+1$ electron particle transition.

Figures 3.1, 3.2, and 3.3 display the tunneling DOS for a particle with the Hamiltonians described above. This particular set of anisotropy energy shifts displays magnetization blockade and voltage control of magnetic hysteresis. In each figure, the tunneling DOS is portrayed in the center of the figure, where the dark blue region represents zero density and the lighter regions display higher density. For Figure3.1, the electrochemical potential in the source lead, represented by the solid orange line, is below the level for the onset of sequential electron tunneling. The Coulomb blockade charging energy is portrayed as the dotted red line, and the magnetization blockade energy is depicted as the dashed green line. As a result, no current flows and so the particle remains in its N electron ground state with $S_z = -100$. The horizontal axis displays the projection of the particle spin onto the easy axis (z-axis), and the illustrations above indicate the precession of the spin at these given S_z projections.

In the following Figures 3.2 and 3.3 illustrating the tunneling density of states, I also plot the long-time distribution of particle states for higher bias voltage values, again corresponding to a particle initialized in the N electron, $S_z = -100$ state. In Figure 3.2, the electrochemical potential in the source lead is maintained between the Coulomb blockade energy and the magnetization blockade energy. As a result, the

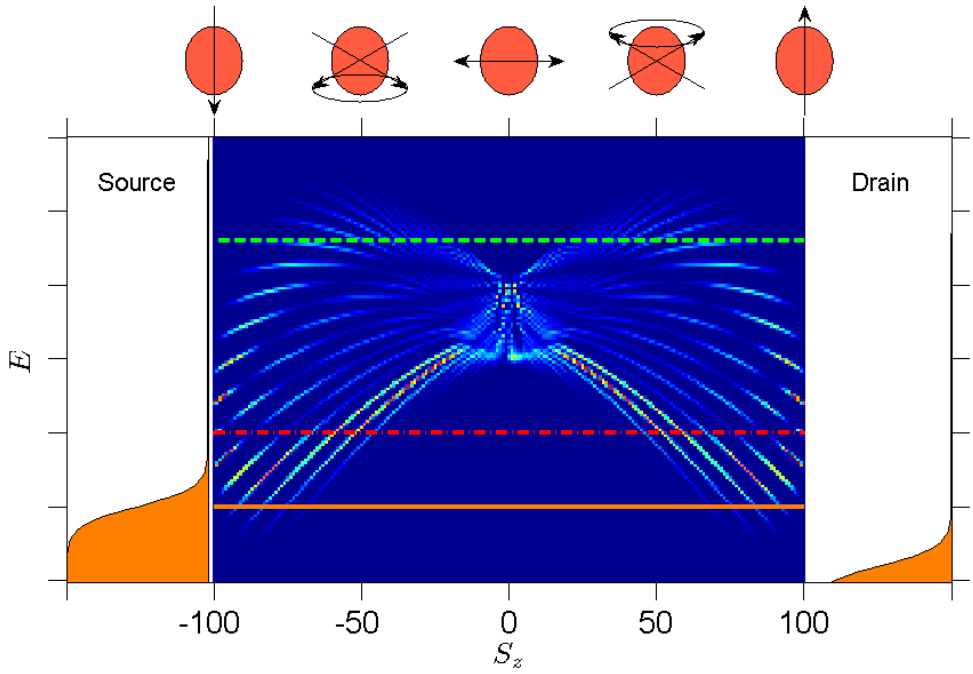

Figure 3.1: Tunneling density of states with low source-drain bias, $\mu_s < E_c < E_M$, where E_C is the charging energy and E_M is the magnetization blockade energy. Lighter regions correspond to stronger density, while dark blue regions correspond to zero density. The orange curves on the left and right illustrate the Fermi functions in the source and drain leads, respectively, and the orange solid line indicates the source Fermi level (that is, the electrochemical potential μ_s in the source lead). The red dotted line indicates the Coulomb blockade. The green dashed line indicates the magnetization blockade. The axes in the bottom and top indicate the spin projection and illustrate the process in the dot. No current flows in this low bias regime, so the particle remains in its initial state.

magnetization becomes excited and departs from the easy axis, but the level of μ_s limits the degree of magnetization motion, and the long-time probability distribution remains localized near the $S_z = -100$ state.

In Figure 3.3, μ_s is raised above the magnetization blockade energy, and thus the particle magnetization is able to explore the full directional phase space. This leads to a state probability distribution in the long-time limit that is approximately uniform.

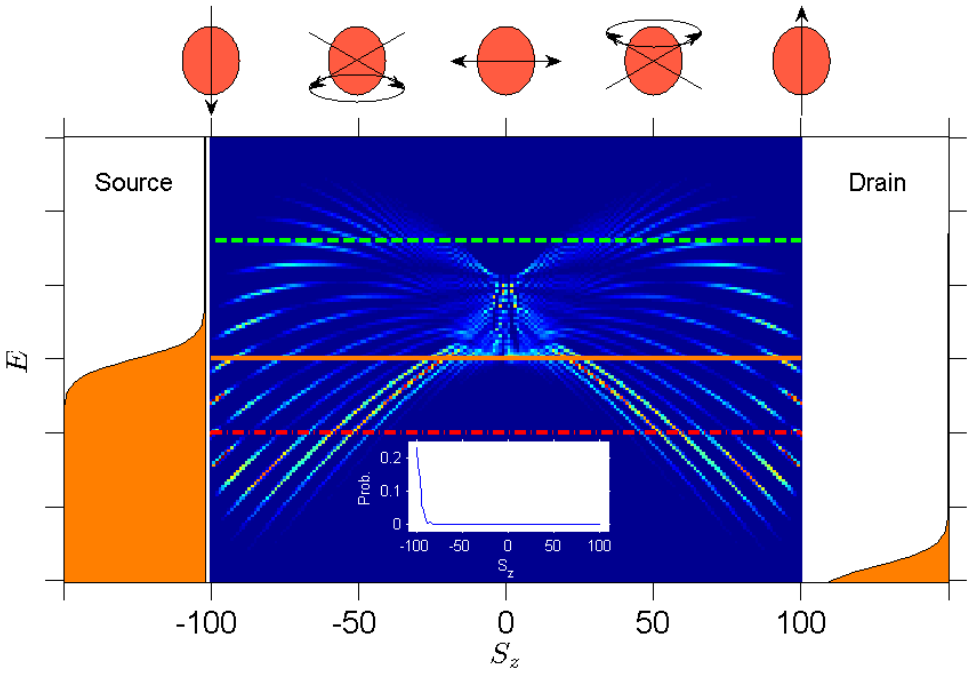

Figure 3.2: Tunneling density of states with medium source-drain bias raised past the threshold of sequential electron tunneling, but remains below the magnetization blockade energy $E_c < \mu_s < E_M$. Particle is initialized in N-electron, $S_z = -100$ state. The inset graph shows the long time histogram of the state distribution. The particle is unable to switch into the other metastable state.

3.3 Probabilities and Generating a Random Event

A stochastic process is one which involves a random variable on some level. When we discuss a random variable $\mathbf{X}$, we often assume that we know something about the values x which the variable can take, where x is a particular realization of the random variable $\mathbf{X}$. Additionally, we often assume that the likelihood of $\mathbf{X}$ realizing the value x is known, and is given by $P(x)$. Here, $P(x)$ is the probability distribution of the the random variable $\mathbf{X}$.

For example, flipping a coin yields either 'heads' or 'tails', which are the particular realizations of x. If the coin is fair, then the probability of the coin landing 'heads' is equivalent to the probability of the coin landing 'tails': $P(H) = P(T) = 0.5$. Note that if we sum over all possible realizations of x if $P(x)$ assumes discrete values (or

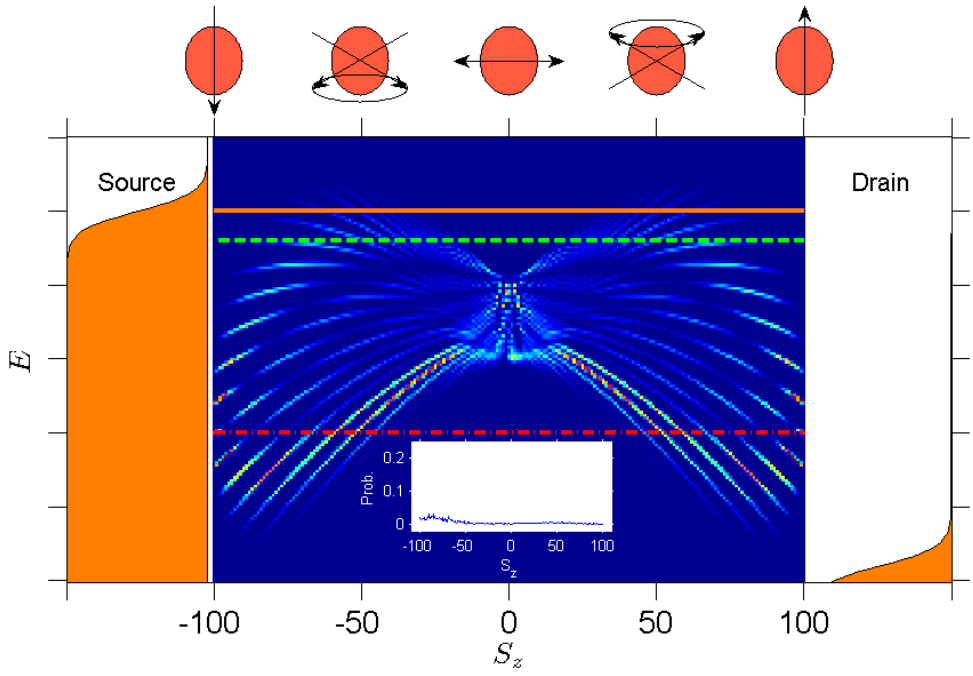

Figure 3.3: Tunneling density of states with large source-drain bias, $E_c < E_M < \mu_s$. Because the energy is raised past the magnetization blockade, the distribution of state probabilities in the inset becomes delocalized and approaches a uniform distribution.

integrate over all realizations of x if $P(x)$ is continuous), then the result is equal to 1. This merely reflects that all possibilities are accounted for.

In the course of the stochastic implementation of the time evolution of the ferromagnetic particle Hamiltonian state distribution, there arises the need to generate a random event each time step to determine whether or not the particle will transition between eigenstates. While there exist standard pseudo-random number generating functions in Matlab and other programming languages for generating random numbers on a given interval, this is mainly accomplished through uniformly distributed random numbers or normally distributed random numbers. Here, the terms 'uniform' and 'normal' refer to the shape of the probability distribution function (pdf) for a given random number [77]. As is indicated in Figure 3.4(a) and (b), the long-time histogram pdf for a normally distributed, and uniformly distributed, respectively, take the shapes of a normal (Gaussian) distribution and a uniform (constant) distribution.

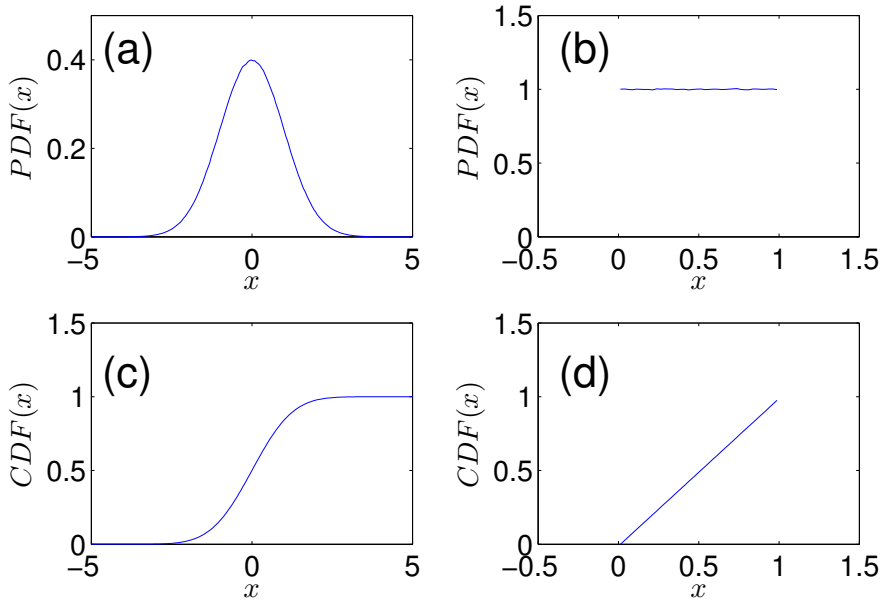

Figure 3.4: Probability Distribution Function (PDF) for (a) normally distributed variable and (b) uniformly distributed random variable. Cumulative Distribution Function (CDF) for (c) normally distributed variable and (d) uniformly distributed variable.

Figure 3.4(c) and (d) display the cumulative sums of (a) and (b), respectively, and model the cumulative distribution function (cdf) for the normally distributed and uniformly distributed pdf's in (a) and (b). Note, in Figure 3.4(d), the true CDF should continue at a constant value of 1 after $x = 1$.

3.4 Stochastic Time-Dependent Simulations

Figure 3.5 displays the basic procedure for generating a random event during each time step and choosing a new eigenstate according to the state change probability distribution function. For visual clarity purposes, the total spin of the N and N+1 electron particle was chosen to be $S_0 = 10$ and $S_0 - 1/2 = 19/2$, respectively. This allowed the total state probability distribution vector (including both the N electron states and N+1 electron states) to have a length of $2 \cdot S_0 + 1 + 2 \cdot (S_0 - 1/2) + 1 = 41$. The first $2S_0 + 1$ state vector indices correspond to the z-projection states of the

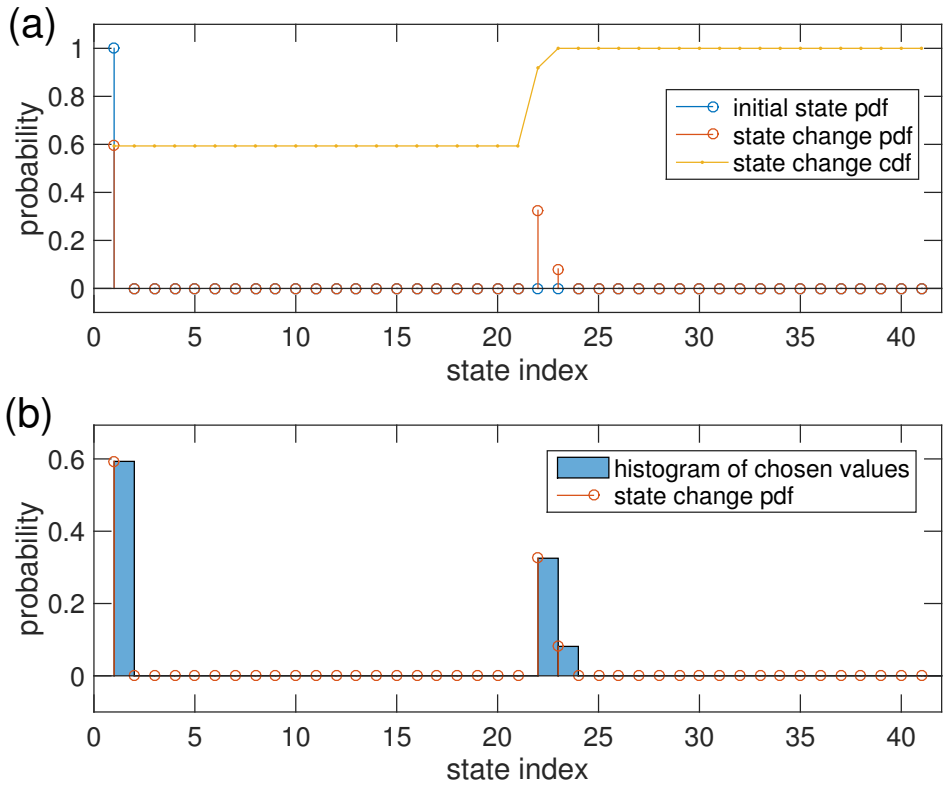

Figure 3.5: State transition illustration. (a) Initial state, state transition pdf, and state transition cdf are displayed. (b) Comparison of state transition pdf and a histogram of randomly chosen values according to the distribution.

N electron particle, where S_z runs from $-S_0$ to S_0 in steps of 1. The remaining $2(S_0 - 1/2) + 1$ state indices correspond to the energy eigenstates of the N+1 electron particle, sorted according to their minimum to maximum S_z values.

In Figure 3.5(a), the particle is assumed in the ground state of the $N = 10$ electron particle at the beginning of the time step (that is, the state index is 1). The master equation is integrated one time step to determine the state change pdf. From the state change pdf, a random number is chosen from this distribution, and the result determines the new particle state at time $t + dt$. This is accomplished by choosing a uniformly distributed random number between 0 and 1, using that number to invert the state change cdf and find the new state. This process is iterated many times as the Hamiltonian or the bias voltage values change. Figure 3.5(b) displays the state

change PDF and a histogram of values randomly chosen according to this distribution using the method described above. The two values match extremely well, showing the reliability of this general random number generator method.

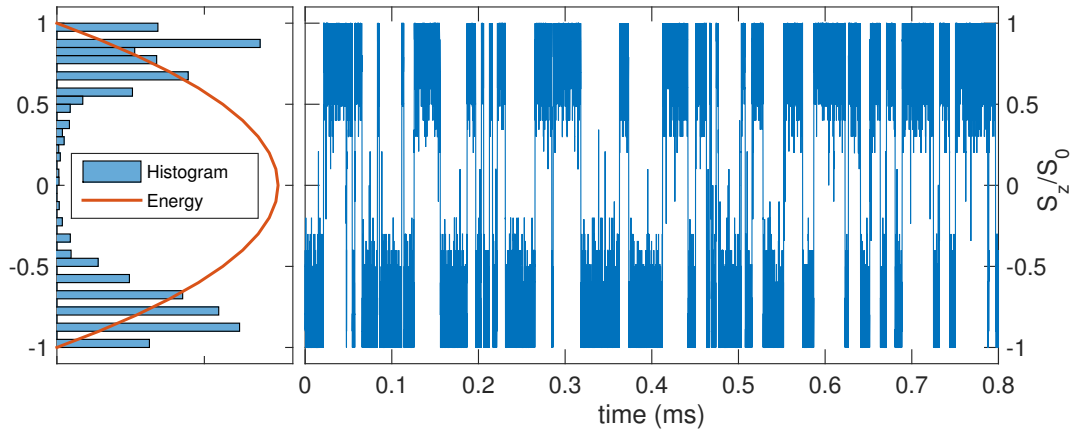

Figure 3.6: Random walk of magnetization due to electron transport. Right, evolution of particle magnetization in time. Left, histogram of occupied spin states (blue bars) and uniaxial anisotropy energy well (red curve).

Figure 3.6 displays the random walk of the magnetization of an $N = 10$ particle with a high applied bias voltage. On the left is a histogram of the states on which the particle dwelt (blue bars), along with the shape of the uniaxial anisotropy energy curve for the N=10 electron particle.

When the time-dependent simulation involves a changing magnetic field, this changes the form of the Hamiltonian and the corresponding eigenstates. For definiteness, suppose that the particle is initially in eigenstate $|\alpha_N\rangle$ of the N-electron Hamiltonian at time t. If the new particle Hamiltonian at time $t+dt$ is different than the Hamiltonian at time t, then before calculating a possible transition to the state at this new time step, I first project the old eigenstate $|\alpha_N\rangle$ onto the the new set of N-electron eigenstates $|\beta_N\rangle$. Upon this projection, I choose the new eigenstate $|\beta_N\rangle$ such that the quantity $||\langle\beta_N|\alpha_N\rangle||$ is maximized. The validity of such an assertion lies in the adiabatic approximation, which assumes that the Hamiltonian is changing slowly enough that the new eigenstate will correspond to an analogous state in the

new Hamiltonian.

To do this, I first need to express $|\alpha_N\rangle$ and $|\beta_N\rangle$ in a common basis. Since the eigenstates of S_z, $|m_z\rangle$, form a complete basis set, I expand $|\alpha_N\rangle$ and $|\beta_N\rangle$ within the $|m_z\rangle$ basis: $|\alpha_N\rangle = \sum_{m_z=-S_0}^{S_0} |m_z\rangle\langle m_z|\alpha_N\rangle$ and $|\beta_N\rangle = \sum_{m_z=-S_0}^{S_0} |m_z\rangle\langle m_z|\beta_N\rangle$. Using this common basis, the projection can be evaluated as:

$$||\langle\beta_N|\alpha_N\rangle|| = ||\sum_{m_z}\sum_{m'_z}\langle\beta_N|m_z\rangle\langle m_z|m'_z\rangle\langle m'_z|\alpha_N\rangle||.$$

Since $|m_z\rangle$ form an orthonormal set, $\langle m_z|m'_z\rangle = \delta_{m_z,m'_z}$, where $\delta_{i,j} = 1$ if $i = j$, or $\delta_{i,j} = 0$ if $i \neq j$. This simplifies the expression of the overlap: $||\langle\beta_N|\alpha_N\rangle|| = ||\sum_{m_z}\langle\beta_N|m_z\rangle\langle m_z|\alpha_N\rangle||$. Once this overlap is calculated for each possible state $|\beta_N\rangle$, I choose the state $|\beta'_N\rangle$ which maximizes the overlap, and change the eigenstate of the particle at time $t + dt$ to $|\beta'_N\rangle$. Then, the usual evolution process of calculating the small change in the state probability distribution vector under the new Hamiltonian and generating a stochastic event to see if the particle will transition during this time step.

3.5 Other Example Simulations

I studied a Hamiltonian parameter space of $K = 10$, $\epsilon = [-200, 200]$, $\epsilon_z = [-200, 0, 200]$, and $\theta_{\rm SE} = [\pi/6, \pi/4, \pi/3, \pi/2]$. All energies are in units of micro-electron volts. Due to mesoscopic fluctuations, these adjustable parameters will vary from sample to sample, and our goal was to merely sample the large possible parameter space. Note, in order to convert from E to voltage, one needs to add the orbital, the exchange, and the charging energy to E, and account for the capacitive division of the voltage. I assume there is only one quasiparticle state μ within the energy range of tunneling, and that the Fermi level in the drain is $-\infty$; that is, $f_R = 0$.

When determining the $I(V)$ characteristics, the state is initialized in the ground state of the N-electron particle. For subsequent bias voltage data points, the initial

state probability distribution is taken as the saturated value from the previous voltage point.

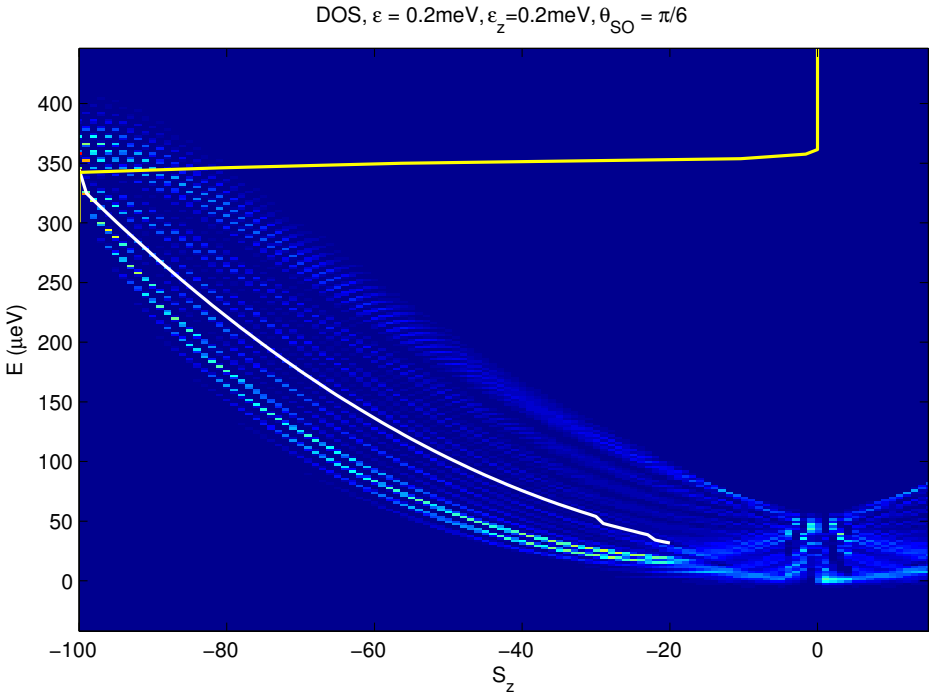

Figure 3.7: Density of states for a magnetically unstable particle. The white line separates regions of spin increasing and spin decreasing transitions. The yellow line indicates the evolution of $\langle S_z \rangle$ as the bias voltage is increased.

In this way, the progression of current and $\langle S_z \rangle$ will occur in the same way as in experiments. Figure 3.7 displays the case for an unstable Hamiltonian ($\epsilon = \epsilon_z = 200\mu$eV, $\theta_{\mathrm{SE}} = \pi/6$), which leads to magnetization stability loss almost immediately after the onset of current. In the DOS shown in Figure 3.7, the white line separates spin increasing and decreasing transitions. For transitions below the white line, the spin projection S_z of the new $N+1$-electron particle state is lower than that of the initial N-electron particle state. The yellow line follows the evolution of $\langle S_z \rangle$ as the source Fermi level is increased. In this example Hamiltonian, the edge of the Coulomb blockade (that is, the source Fermi energy corresponding to the onset of current) is located at 0.342meV. The magnetization begins to become unstable (that is, $\langle S_z \rangle$ begins to rapidly increase) at the same source Fermi energy of 0.342 mV. By the

time the source Fermi level is raised to 0.346 meV, the magnetization is completely randomized as $\langle S_z \rangle \to 0$. Therefore, the current and magnetic stability characteristics are highly dependent on mesoscopic fluctuations from particle to particle. The form of the DOS in this unstable case, unlike the example in earlier in the chapter, lacks levels that increase along with increases of S_z. In the example DOS in at the beginning of the chapter, $\langle S_z \rangle$ follows the upward-sloped levels, and doesn't become unstable until the level features begin to decrease vs. S_z. In the DOS referenced here, the initial levels near the onset of Coulomb blockade are decreasing vs. S_z, so the magnetization is unstable from the beginning of current onset. In both DOS cases, when the levels begin to decrease vs. S_z, a spin-flip cascade is initiated as subsequent spin-increasing transitions require less and less energy. The result is the delocalization of $\langle S_z \rangle$ as magnetic stability is lost.

3.6 Master Equation

The master equation utilized in our present work is adapted from references [73] and [147]:

$$\frac{\partial P_\alpha}{\partial t} = \sum_\beta \sum_{l=L,R} \sum_{\sigma=\text{up,down}} \Gamma_{l\sigma} \Big[\left|\langle \beta | c_{\mu\sigma} | \alpha \rangle\right|^2 \left(f_l(E_\alpha - E_\beta) P_\beta - (1 - f_l(E_\alpha - E_\beta)) P_\alpha \right) + \left|\langle \beta | c^\dagger_{\mu\sigma} | \alpha \rangle\right|^2 \left(-f_l(E_\beta - E_\alpha) P_\alpha + (1 - f_l(E_\beta - E_\alpha)) P_\beta \right) \Big]$$

The above equation determines the evolution of the probability P_α of occupation of a given particle state $|\alpha\rangle$ in time. The spin of the electron is σ, and the tunneling rate $\Gamma_{l\sigma}$ in general could be different for the source and drain leads, and could depend on the spin polarization. The time rate of change of P_α depends on the Fermi level in the source and drain leads (L and R, respectively). These Fermi functions are evaluated at the energy differences $E_\alpha - E_\beta$ between the states involved in tunneling. Each term in the sum also depends on the overlap between states $|\alpha\rangle$ and $|\beta\rangle$, upon the addition ($c^\dagger_{\mu\sigma}$) or subtraction ($c_{j\sigma}$) of an electron, where $c^\dagger_{\mu\sigma}$ is the electron creation

operator for the μ^{th} level, and $c_{\mu\sigma}$ is the electron annihilation operator for the μ^{th} level.

Figure 3.8 illustrates the result of running the full master equation simulation, rather than a stochastic realization. Each of the panels show how the state probability distribution evolves as a function of time for different constant bias voltage values. For each time step, the probability distribution is normalized by the occupation factor of its most likely state, in order for the color scale to be readable for all times. This might give the appearance of an (unphysical) increase in the total amount of probability, but this is for visual clarity only. The total probability is always normalized to 1 throughout the simulation.

In Figure 3.8(a), the only occupied states remain well-localized near the $S_z = -100$ eigenstate. If the bias voltage is increased, as in Figure 3.8(b), some of the probability leaks into the other minimum energy well (that is, the state distribution acquires a finite value for states near $S_z = +100$. This effect of the spreading of the probability among the two different potential wells is even more apparent in Figure 3.8(c). For Figure 3.8(d), which corresponds to the highest applied voltage, the state probability distribution quickly becomes uniform or equipartitioned among all of the eigenstates.

When determining the $I(V)$ characteristics, the state is initialized in the ground state of the N-electron particle. For subsequent bias voltage data points, the initial state probability distribution is taken as the saturated value from the previous voltage point. In this way, the progression of current and $\langle S_z \rangle$ will occur in the same way as in experiments.

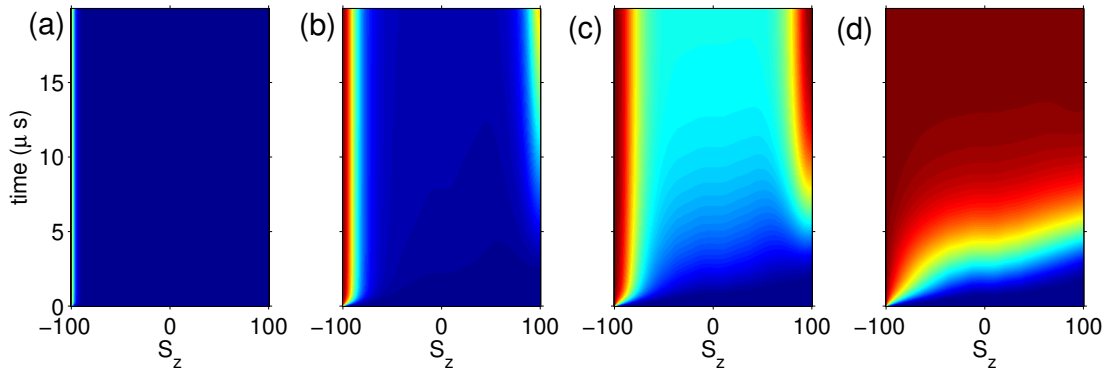

Figure 3.8: Evolution of full master equation state distribution vs time, for a particle initialized in the $S_z = -S_0$ ground state. Four panels show the effects of an increasing bias voltage on the steady state convergence of the state distribution. (a) Low bias voltage, the state distribution remains localized near $S_z = -100$. (b) Slightly higher bias, some state probability surmounts barrier and begins to collect near the $S_z = +100$ state. (c) Still higher bias voltage. The state distribution quickly fills both wells of $S_z = \pm 100$. (d) Highest voltage considered here, the particle state distribution becomes equipartitioned among all eigenstates.

CHAPTER IV

GIANT ELECTRON-SPIN-G-FACTORS IN A FERROMAGNETIC NANOPARTICLE

In this chapter, we utilize single-electron tunneling spectroscopy to measure the discrete energy levels in a nanometer-scale cobalt particle at T=60mK, and find effective single-electron spin g-factors ≈ 7.3. These large g-factors do not result from the typical orbital contribution to g-factors, since the orbital angular momentum is quenched. Instead, they are due to non-trivial many-body excitations. A kink in the plot of conductance vs. voltage and magnetic field is a signature of degenerate total spin on the particle. Spin-Orbit interactions cause the new particle eigenstates to have 'spin' that is an admixture of pure spin states. Fluctuations in the discrete energy level spacing allow for the total change in 'spin' on the particle during a single-electron tunneling event to be $\Delta S' = 3/2$, leading to a g-factor around 6.

4.1 Introduction

The g-factor of an elementary particle is a dimensionless parameter relating the magnetic moment and the angular momentum. For an electron, the magnetic moment due to spin $\vec{S}$ is $\vec{\mu} = -g\mu_B\vec{S}/\hbar$, where g is the spin g-factor, μ_B is the Bohr Magneton, and $\hbar$ is the reduced Planck constant. In the Dirac point particle model of an electron, the spin g-factor is precisely 2, but the coupling to the environment can change that value. Recently, g-factors were measured of single electrons occupying quantum electron-in-a-box levels in a nanometer-scale metallic particle . [8, 23, 39, 41, 74, 80, 118, 119, 125] In particles made from light metals such as Al, the g-factors are very close to 2, demonstrating that the g-factors are (very nearly) spin g-factors, and that coupling

between the spin and the environment is weak. The orbital motion of the electron does not affect the g-factors in light metallic particles because of the quenching of the orbital angular momentum. [2, 102] Introduction of heavier metals into the particle material leads to a significant reduction of the g-factor, caused by the coupling between the electron spin and the crystalline environment, via the Spin-Orbit (SO) interaction. [39, 125]

Here we present measurements of electron g-factors $g \approx 7.3$ in a ferromagnetic (Cobalt) particle. We show how this strong enhancement arises from the coupling between traditional electron-in-a-box levels and the many-body states in the electronic environment, when the ground state of the particle is nearly spin-degenerate. A different mechanism leading to very large spin g-factors has been proposed for normal metal particles, but large g-factors have not been confirmed until now, probably because of the weak electron-electron interactions in normal metals. [55, 56] By switching the material from normal metal to a ferromagnet, the electron-electron interactions strengthen, making it more probable to observe large g-factors. Very large g-factors have been observed recently in semiconducting quantum wires and dots, where they represent the orbital contribution. [105, 108, 128] The difference between semiconducting wires or dots and our metallic particles is that the orbital contribution is quenched in the metallic particle. The assumption that the orbital angular momentum is quenched in a metal particle is based upon the work by Matveev and Adam, [2, 102] wherein they calculate the orbital contribution to the g-factor for a range of SO strengths, as well as for diffusive and ballistic transport. In the case of zero SO interaction, there is no contribution to the orbital g-factor because the magnetic field required to add a magnetic flux quantum over the area of our sample is $\approx$ 1000T. When SO$\neq$0, the orbital contribution for a ballistic nanoparticle is on the order of $\left(\frac{m}{m^*}\right)^2$, where m and m^* are the electron mass and effective mass, respectively. Because the effective mass is enhanced for the narrow d-band of Cobalt,

this orbital contribution term will not be $\gg 1$. For the diffusive particle case, the orbital contribution will be even smaller. The large g-factors described in this letter are of spin-origin, making the effect described herein different from that in semiconducting quantum dots and wires. This finding shows that a fundamental property of an electron, like the spin g-factor, can be strongly modified by the environment in an unexpected way.

4.2 Experimental Methods and Data

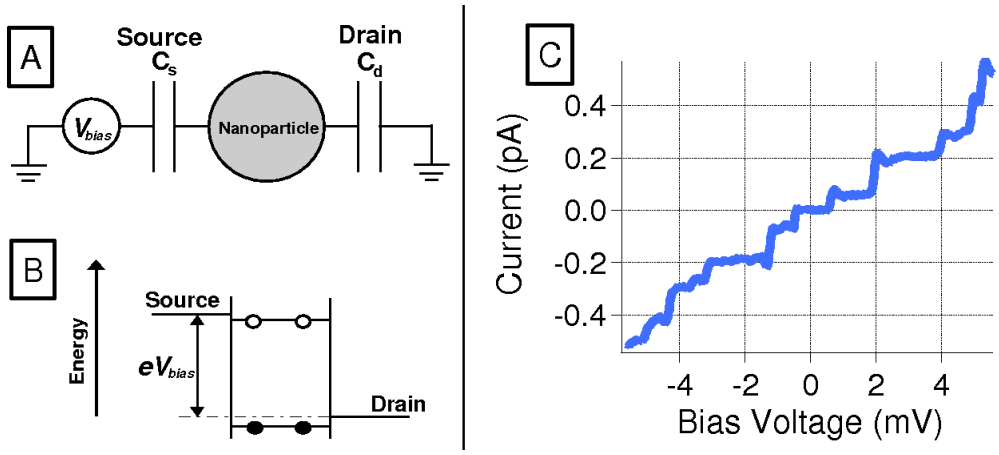

Figure 4.1: (a) Circuit diagram of tunneling through particle. (b) Energy level diagram for tunneling process. (c) IV curve displaying coulomb blockade and discrete single-electron tunneling steps.

Fig. 4.1(a) sketches our arrangement for the studies of quantum levels and g-factors in a metallic particle. A single metallic particle is attached between two macroscopic leads, via high resistance tunnel junctions. Fig. 4.1(b) displays the energy levels of the particle between the tunnel junctions. A voltage V_{bias} is applied on the source lead, changing the Fermi level in that lead by eV_{bias}. When the Fermi level in the source is equal to the energy difference between the final and the initial quantum state of the particle (after and before tunneling), an electron can tunnel from the Fermi level in the lead into the particle, resulting in current flow. In that case the electrons flow through the particle one-by-one. Current versus voltage increases

in discrete steps at the voltages where the Fermi level in the source equals the energy difference between the final and the initial quantum states of the particle, as our sample shows in Fig. 4.1(c). In most metallic particles, the energy difference between the final and the initial quantum state of the particle is equal to a discrete electron-in-a-box level in the particle. Thus, voltages at which the steps are observed in the I-V curve correspond to the discrete electron-in-a-box levels ϵ_μ. These levels are two-fold spin-degenerate, because of Kramers' theorem, and the degeneracy is lifted by the applied magnetic field. The g-factor is defined as in Ref. [56], by

$$g = \frac{\pm 2}{\mu_B} \frac{d\epsilon_\mu}{dB}. \tag{1}$$

The tunneling junction devices are fabricated using the same recipe quoted in Ref. [74]. See Appendix A for more details. The devices are studied at T=60mK in a dilution refrigerator. The voltage bias is swept and the output current is measured using an Ithaco model 1211 current preamplifier. The detailed data sweeps involve a slow magnetic field ramp, along with a slightly faster sweep of the voltage bias. The differential conductance is calculated numerically. Fig. 4.2 displays our experimental data of the differential conductance vs. applied magnetic field and bias voltage for a Co sample. There are three main features of the data that are different from previous work on magnetic field dependence of tunneling spectra in a Co particle. First, the energy levels vs. magnetic field exhibit an abrupt change in slope around $B = 4$T. This kink was absent in prior work, which displayed energy levels that were monotonic with field in the range $B > 1$T. [41, 58, 74] Second, the g-factors of some levels in the figure are larger than 2. For example, the levels marked A and B in the figure correspond to g-factors of ≈ 7.3 at $B > 4$T. In comparison, prior work displayed only g-factors < 2 or ≈ 2 [41, 58, 74]. Finally, the fluctuations in the weights (i.e., the relative heights of the differential conductance peaks) of various levels is enhanced. Level A has a weight that is a factor of ≈ 4 smaller than level C, which displays a g-factor of ≈ 0.6. In Appendix C, additional data is provided, demonstrating the usual

magnetic hysteresis loops of discrete levels in the low magnetic field range (< 1.5T). Because the energy level spacing of the Co particle is comparable to that of our previous work, we estimate the particle size to be ≈ 2nm . [74]

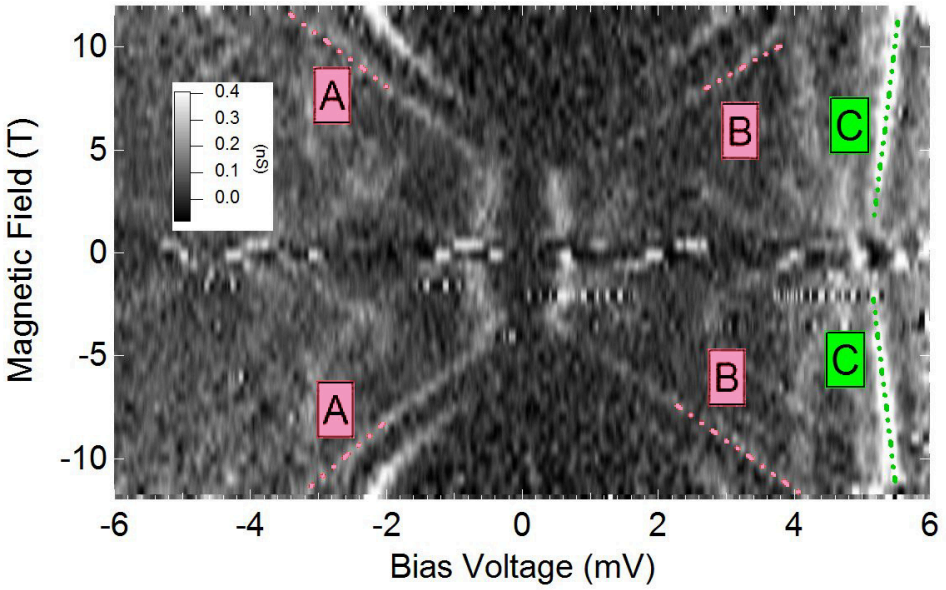

Figure 4.2: Experimental data of differential conductance vs. magnetic field and bias voltage. The dotted lines follow the conductance peak behavior for two different spin transitions. The slope of the red dotted lines (A and B) yield a g-factor of ≈ 7.3, while the green dotted lines (C) correspond to a g-factor ≈ 0.6.

4.3 Data Model: the Universal Hamiltonian

In this letter, we will present the analysis of electron tunneling through the particle, based on the Universal Hamiltonian (UH) model, and show how giant spin g-factors naturally arise in a ferromagnetic particle near spin degeneracies. [3] In the UH model, when the SO-interaction is zero, the electron-electron interaction commutes with the kinetic energy and the confinement potential, and the electronic energy in a metallic particle can be written as

$$E(N, S_0) = \sum_{\mu,\sigma=\uparrow,\downarrow} \epsilon_\mu n_{\mu,\sigma} - \frac{U}{2} S(S+1) - 2\mu_B B S_z, \tag{2}$$

where ϵ_μ is the energy of electron-in-a-box level μ, $n_{\mu,\sigma}$ is the occupation number for the level μ and spin direction σ, U is the exchange interaction, B is the magnetic field applied along z-axis, and S and S_z are the spin magnitude and its z-component, respectively, in units of $\hbar$. If the exchange interaction is small compared with the level spacing δ_μ at the Fermi level, then the ground state for this Hamiltonian will be the normal-metal Fermi sphere, with spin 0 or 1/2, depending on parity of the number of electrons on the particle (N). Giant spin g-factors can arise in the normal-metal state; however, their probability is very low. In the ferromagnetic state, the probability of giant g-factors increases dramatically; thus, we first analyze the ferromagnetic case.

Ferromagnetism occurs if the exchange interaction U is comparable to or larger than the level spacing $\delta_\mu = \epsilon_{\mu+1} - \epsilon_\mu$ at the Fermi level, and some minority electrons are promoted to higher level majority states. The maximum energies of the occupied levels will be labeled ϵ_m and ϵ_M (with corresponding level spacings δ_m and δ_M), for the minority and majority electrons, respectively. In the ground state, the exchange splitting between ϵ_m and ϵ_M is compensated by the gain in the exchange interaction energy: $\epsilon_M - \epsilon_m = U(S_0 + 1/2) + d(B)$. [35, 99] The parameter $d(B)$ has magnetic field dependence $d(B) = d_0 - 2\mu_B B$, where d_0 is a mesoscopic parameter. Since the level spacings vary by the Wigner-Dyson statistics, the value of $\epsilon_M - \epsilon_m$ will have mesoscopic fluctuations comparable to $\delta_M + \delta_m$. Fig. 4.3(a) depicts the N-electron ferromagnetic ground state with spin S_0. S_0 will be the ground state spin of the particle if $(U/2 - \delta_M) < d(B) < (\delta_m - U/2)$. At the applied magnetic field B_d, defined as $d(B_d) = U/2 - \delta_M$, the ground state is degenerate; that is, $E_N(S_0) = E_N(S_0 + 1)$. In a magnetic field slightly above B_d, the N-electron particle ground state spin will be $S_0 + 1$. The $S_0 + 1$ state is obtained from the diagram in Fig. 3-A, by annihilating the minority electron at energy ϵ_m and creating a majority electron at energy ϵ_{M+1}.

As the magnetic field increases further, the transitions to higher spin states take place at the corresponding degeneracy fields. The stability regions for the ground

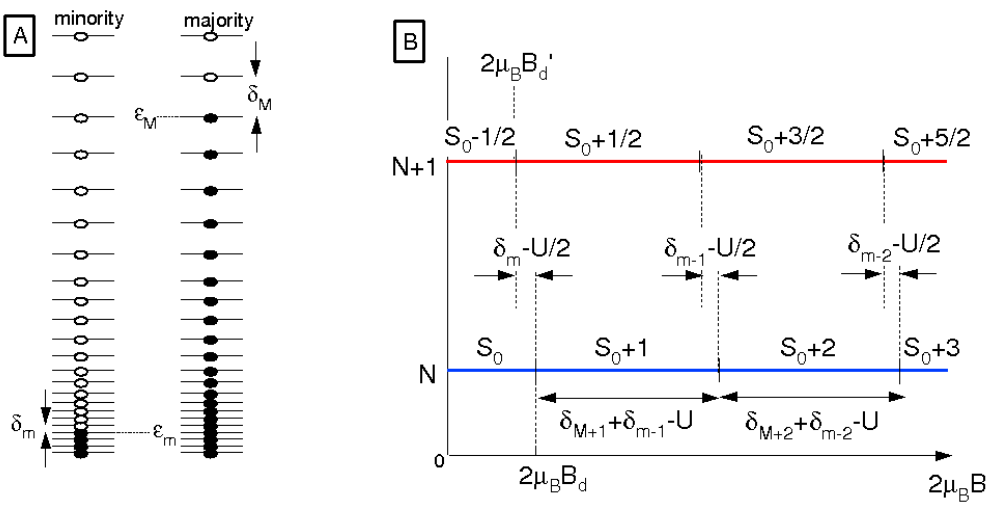

Figure 4.3: A. Electron-in-a-box levels for minority and majority electrons. The black dots signify occupied levels. B. Stability Diagram for N- and (N+1)-electron particle. The spin value in each region denotes the ground state spin for the given magnetic field range. There is a degeneracy in ground state spin at $B = B_d$ and $B = B_d'$ for the N- and (N+1)-electron cases respectively.

state spins $S_0 + i$, $i = 0, 1, 2, ...$ are shown in Fig. 4.3(b).

In a Co particle, the average spacings and the exchange interaction are $\overline{\delta}_M = 4.58\text{eV}/S_0$, $\overline{\delta}_m = 1.18\text{eV}/S_0$, and $U = 1.77\text{eV}/S_0$, respectively. [35,114] Note that the level spacings scale as $1/S_0$, which accounts for the vanishingly small level spacings as the electron number approaches typical bulk values. The magnetic field region (ΔB) for the stability of a particular spin is, on average, $2\mu_B \Delta B = \overline{\delta}_M + \overline{\delta}_m - U = 4\text{eV}/S_0$. For a typical Co particle in our experiment, $S_0 \approx 1000$, and the corresponding magnetic field range is quite large, $\Delta B \approx 35\text{T}$. Since our typical experimental field range of is $\approx 10\text{T}$, we do not expect to observe spin degeneracy in a typical sample.

In an electron tunneling process, the number of electrons on the particle changes by one. In that case, if the particle spin before tunneling is S_0, then the final spin of the particle after the tunneling transition will be $S_0 \pm 1/2$. In Co, most tunneling transitions will be spin-lowering, as discussed previously. [41, 58, 74] Indeed, experimental studies of electron-in-a-box levels in Co particles done to date show that the levels from a given sample have roughly linear magnetic field dependence above about

1T, with similar g-factors < 2.

Fig. 4.3(b) also displays the regions of stability for the ground state spins of $S_0 - 1/2 + i$, for the $(N+1)-$electron system. B'_d is the degenerate magnetic field value for the $(N+1)$-electron particle. Note that in most of the magnetic field range, the tunneling transition between the ground states reduces the spin by 1/2. However, in the narrow magnetic field range slightly below the degeneracy field B_d, the tunneling transition between the ground states will be spin-increasing, $S_0 \rightarrow S_0 + 1/2$. Such spin increasing tunnel transitions occur between $B = B'_d$ and $B = B_d$, where $g\mu_B(B_d - B'_d) = \delta_m - U/2$. On average, $\langle B_d - B'_d \rangle / \Delta B = 0.07$. However, there is a prediction from the UH model that did not gain much attention until now, as far as we are aware. Because the level spacings fluctuate, there is a possibility that $(\delta_m - U/2)$ could be negative. In a Co particle, $\overline{\delta}_m = 1.33U/2$. Assuming the Wigner-Dyson distribution for δ_m, Pr$[(\delta_m - U/2) < 0]$=36% (See Appendix B). If $(\delta_m - U/2) < 0$, then in the magnetic field interval $[B_d, B'_d]$, the ground state spins of the $N-$ and $(N+1)-$electron systems will be $S_0 + 1$ and $S_0 - 1/2$. In that case, the tunneling transitions between the ground states involve a spin-difference of 3/2, so the tunnel transition would display a g-factor of 6. Near any spin degeneracy, tunneling transitions between excited states can show large g-factors as well.

However, the tunnel Hamiltonian has zero-valued matrix elements between states of the particle with a spin difference other than $\pm 1/2$. That is, there is a spin selection rule $\Delta S = \pm 1/2$. But, if the SO-interaction in the particle is included, then the matrix elements $\langle S_0 - 1/2, S_0 - 1/2 | H_{\rm SO} | S_0 + 1/2, S_0 + 1/2 \rangle$ and $\langle S_0, S_0 | H_{\rm SO} | S_0 + 1, S_0 + 1 \rangle$ will be nonzero. For example, the calculation of the matrix element $\langle 3/2, 3/2 | H_{\rm SO} | 1/2, 1/2 \rangle$ is available in Ref. [56].That calculation can be extended in a straightforward way to our states with large S_0, but would be beyond the present scope. In a ferromagnetic particle with large S_0, many of the matrix elements of $H_{\rm SO}$ calculated in Ref. [56] become negligibly small in the thermodynamic

limit. For example, while $\langle S_0+1, S_0+1|H_{\rm SO}|S_0, S_0\rangle$ and $\langle 3/2, 3/2|H_{\rm SO}|1/2, 1/2\rangle$ are comparable, $\langle S_0+1, S_0|H_{\rm SO}|S_0, S_0\rangle$ is smaller by factor of $\sim 1/\sqrt{2S_0}$ compared to $\langle 3/2, 1/2|H_{\rm SO}|1/2, 1/2\rangle$. The SO-interaction becomes a tri-diagonal matrix connecting only spin ground states, while the matrix elements connecting different magnetically excited levels can be neglected.

The result is that the spin-eigenstates of the particle with N+1 electrons are 'spin' admixtures (hereafter labeled with a prime index) of pure states $|S_0+1/2, S_0+1/2\rangle$ and $|S_0-1/2, S_0-1/2\rangle$. Similarly, for the N electron system, states $|S_0, S_0\rangle$ and $|S_0+1, S_0+1\rangle$ mix. The closer the system is to spin-degeneracy, the stronger the admixing will become. The admixing produces two effects. First, the matrix elements of the tunnel Hamiltonian between $|S_0, S_0\rangle' \rightarrow |S_0 \pm 1/2, S_0 \pm 1/2\rangle'$ and $|S_0+1, S_0+1\rangle' \rightarrow |S_0 \pm 1/2, S_0 \pm 1/2\rangle'$, become nonzero. Now all tunneling transitions involving these four levels become active. If admixing is weak, then the weight of the transition $|S_0+1, S_0+1\rangle' \rightarrow |S_0-1/2, S_0-1/2\rangle'$ will be weak compared to the weight for transition $|S_0, S_0\rangle' \rightarrow |S_0-1/2, S_0-1/2\rangle'$. Similar variation in weights have been predicted before. [56] Second, the admixing will change the g-factors of the levels. For example, we expect the g-factor for the transition $|S_0+1, S_0+1\rangle' \rightarrow |S_0-1/2, S_0-1/2\rangle'$ to be widely distributed around 6 and likely to remain much larger than 2, similar to the analysis in Ref. [55,56]. However, there needs to be a more rigorous, full Random-Matrix-Theory description that includes orbital contributions to the g-factor in order to fully account for the value measured of 7.3.

Fig. 4.4-(a),(b) sketches the energy versus magnetic field near the spin-degeneracy for the N- and $(N+1)$- electron systems. In the magnetic field range between B_d and B_d' indicated in the figure, the tunneling transition between the ground states involves a 'spin' change of $\Delta S' = 3/2$, and the g-factor should be about 6. Even if $B_d > B_d'$, the tunnel transition with $\Delta S' = 3/2$ will be close in energy. Thus, we expect to observe large g-factors for the transitions between the excited states, as

long as the applied magnetic field is tuned near spin-degeneracy.

In a normal metal particle, the above analysis leads to a similar result. At the degeneracy field $B_{d,S-T}$ between singlet and triplet for the N-electron state (assuming N is even), the magnetic field is off degeneracy between doublet-quadruplet for the (N+1)-electron state by the amount given by $g\mu_B(B_{d,S-T} - B_{d,D-Q}) = \delta - U/2$. In order to observe a tunnel transition between ground state with spin-difference 3/2, $(\delta - U/2)$ needs to be less than zero. In contrast to the Co particle, U in a normal metal is small. For example, in a Au particle, $U/2 \approx 0.06\delta$, leading to the probability of 0.3% that the tunneling transition between ground states has $\Delta S' = 3/2$. [56] This is perhaps the reason no g-factors larger than two have been measured in a metallic particle, until now.

Moving back to Co particles, in order to measure large g-factors, we need to measure the particle near spin-degeneracy at the ground state. The experimental signature of the degeneracy would be a kink in the energy level versus magnetic field, according to Fig. 4.4(c),(d). This is consistent with our data, where several levels display a kink near $B = 4$T. Our model also agrees with the predictions of Ref. [13], which discusses the signature kink in data near degeneracies, and is reminiscent of Ref. [91,141]. Although the shape of the kink is not the exact same as that suggested by our simple model, the two have qualitatively good agreement. Additionally, we do not observe a second kink in the higher field range. However, due to the increasing intensity of the conductance peaks in the higher field range (which we attribute to stronger admixing between states), as well as a slight curvature of the lowest level near 12T, it is likely that a second kink lies beyond our magnetic field range.

4.4 Conclusion

In summary, we predicted the possibility of large spin-g-factors of a ferromagnetic particle tuned close to spin-degeneracy. The existence of these giant effective g-factors

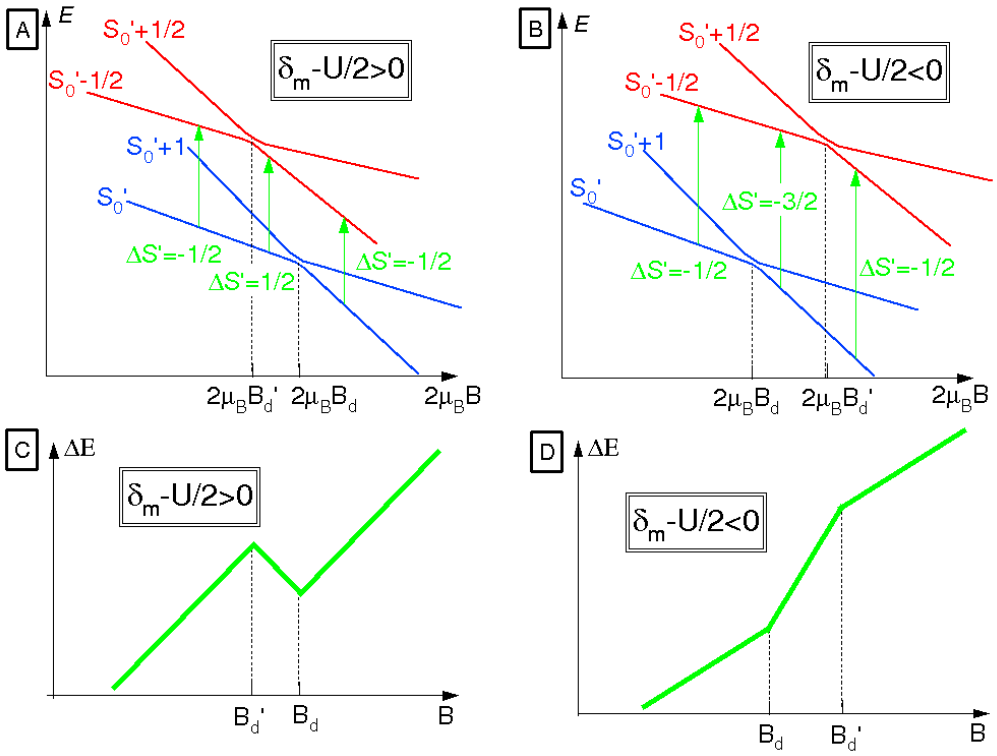

Figure 4.4: Possible spin transitions upon the tunneling event of a single electron onto the particle. The length of the arrows represent the energy change of the particle upon such a transition. A. Case where $B_d' < B_d$, ($\delta_m > U/2$). B. Case where $B_d' > B_d$, ($\delta_m < U/2$). C,D. Kink in energy curve as a function of B for the two cases considered in A,B.

is due to the many-body interactions (i.e., strong exchange energy) in a ferromagnetic particle. When tuned within a certain range, the magnetic field induces a degenerate total spin value on the particle. Due to fluctuations in the electron-in-a-box level spacings, there is a significant probability that this magnetic field range, along with spin-orbit interactions, can allow transitions that change the 'spin' of the particle by 3/2 upon the tunneling event of a single electron. However, this will only occur if the magnetic field is tuned sufficiently close to one of these degenerate field values. We prepared many samples of cobalt particles, and found the experimental signature of a degenerate magnetic field value (the kink in the conductance data plot). Within this data set, we found very large g-factors (g$\approx$ 7.3), in relatively close agreement with

our prediction. These giant spin-g-factors display the intricate interplay between the many-body energy states and the traditional electron-in-a-box quantum states.

4.5 Appendices

4.5.1 Appendix A: Sample Fabrication

The structures of our samples are defined using electron-beam lithography on a poly(methyl methacrylate)(PMMA) substrate, as is illustrated in Fig. 4.5.

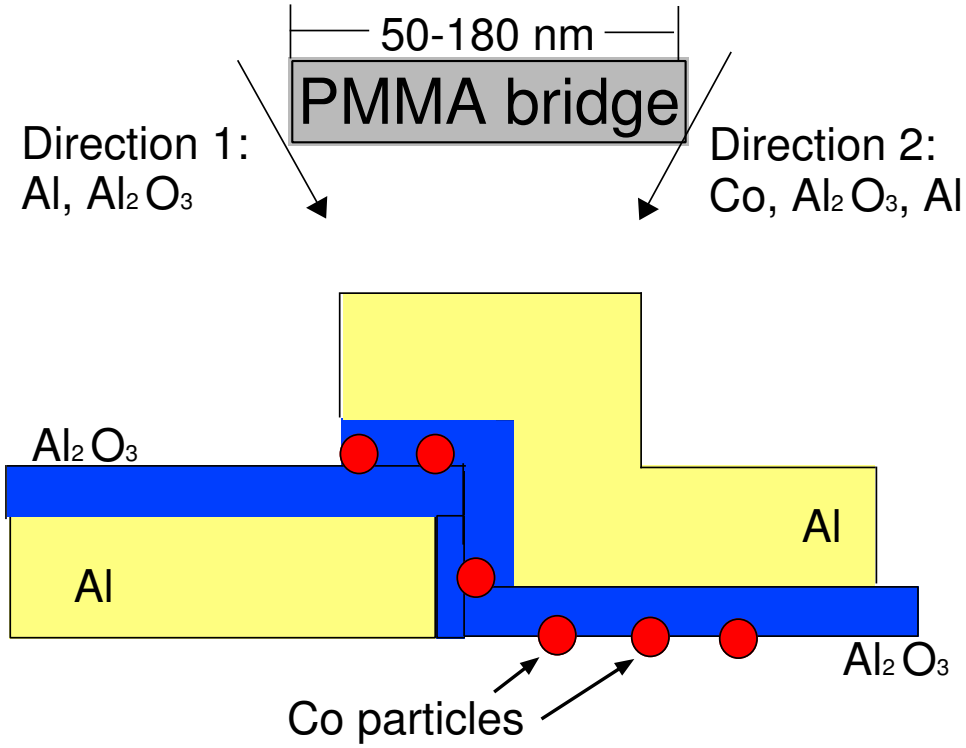

Figure 4.5: Sample fabrication process. The cobalt particles are shown in red between the two tunneling barriers (blue) and the conducting Al electrodes (yellow)

After exposure to the electron-beam, the sample is placed in developer solution and a bridge of PMMA is established for use in shadow evaporation. Next, the sample is placed in a vacuum chamber and the tunnel junctions are created through shadow evaporation around the PMMA bridge. Aluminum is evaporated to form the electrode, followed by a a layer of Al_2O_3 to form the first tunneling barrier. Next, the sample is rotated and a layer of Cobalt on the order of 0.6 nm is added, which

nucleates due to surface tension and forms the nanoparticles to be studied. A second layer of Al_2O_3 is then added to form the other tunnel junction, and then a final layer of Al is evaporated to form the other electrode. The electrodes are $\approx$ 14 nm thick, and the Al_2O_3 tunnel junctions are $\approx$ 1.7 nm thick. After the evaporation process, the excess metals are lifted off in acetone, leaving a series of patterned devices on our substrate. The nanoparticles are pictured in Fig. 4.6 in a Transmission Electron Microscope (TEM) micrograph.

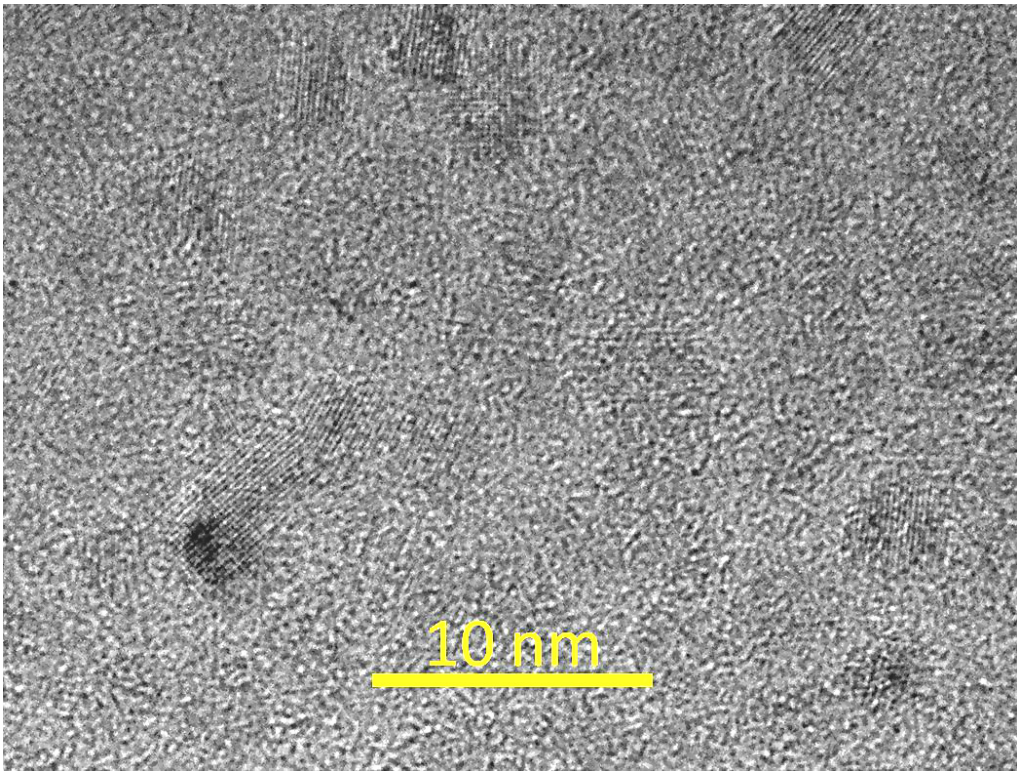

Figure 4.6: TEM image of Co nanoparticles (dark) on amorphous Al_2O_3 background (light)

4.5.2 Appendix B: Wigner-Dyson Statistics

The energy level statistics of electrons occupying chaotic wavefunctions on the quantum dot can be modeled using Random Matrix Theory (RMT) and Wigner-Dyson statistics. For our model, we use the Gaussian Orthogonal Ensemble (GOE) because

we are in the low magnetic field regime and therefore can treat the system as effectively time-reversal invariant. Modeling the system with the Gaussian Unitary Ensemble (GUE), which is the ensemble that should be used for systems without time-reversal symmetry, was also performed, but the results for GOE and GUE have a difference of only a few percent. The GOE has normalized energy level $\left(x \equiv \frac{\delta_m}{\langle \delta_m \rangle}, \text{ where } \langle \delta_m \rangle \equiv \overline{\delta}_m\right)$ fluctuations that follow the distribution function $F(x)$:

$$F(x) = \frac{\pi}{2} x e^{-\frac{\pi}{4}x^2} \tag{3}$$

So to find the probability, Pr, that $(\delta - U/2)$ is negative, we note:

A similar calculation using the GUE instead yields a probability of $\approx 30\%$. Either way, there is non-negligible probability that the quantity $(\delta - U/2)$ will be negative.

4.5.3 Appendix C: Low Magnetic Field Data (< 1.5T)

The data shown in Fig. 4.7 displays the low magnetic field regime of the differential conductance vs. voltage. Over time, the field was swept from $-1.5 \rightarrow +1.5$T, and then from $+1.5 \rightarrow -1.5$T. This is shown in the graph by reading it from top to bottom. The discontinuities in the conductance data for the same bias voltage values indicate that a magnetic switch has occurred. Note the hysteresis in the switching field values— when the field is swept from negative values to positive ones, the switch occurs in the positive magnetic field range. Conversely, when the field is swept from positive to negative values(the lower half of the graph) the switch occurs for negative field values. These characteristics indicate that we are indeed measuring the tunneling through a single ferromagnetic particle, and agree qualitatively with previous work on Co particles [74].

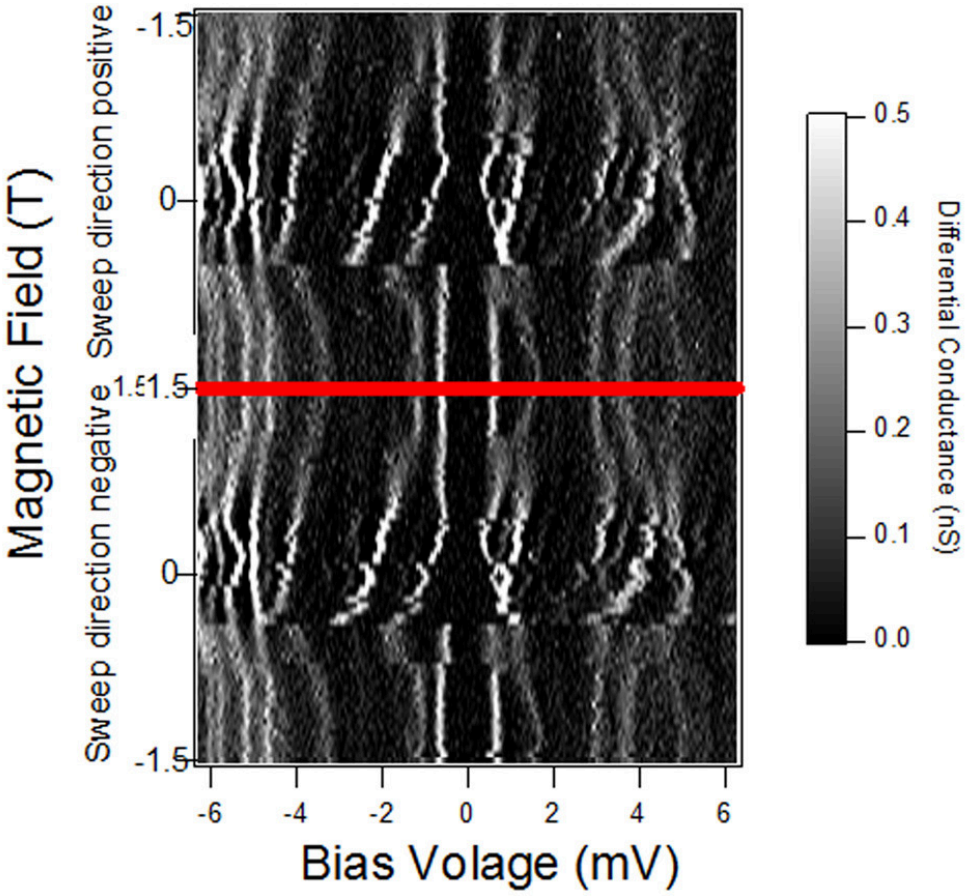

Figure 4.7: Low Magnetic Field Data < 1.5 T

CHAPTER V

VOLTAGE CONTROL OF MAGNETIC HYSTERESIS IN A NICKEL NANOPARTICLE

In this chapter, the effects of voltage bias on magnetic hysteresis in single Ni particles 2-3nm in diameter are measured between temperatures of 60mK and 4.2K, using sequential electron tunneling through the particle. While some Ni particles do not display magnetic hysteresis in tunneling current versus magnetic field, in the Ni particles that display hysteresis, the effect of bias voltage on magnetic switching field is nonlinear. The magnetic switching field changes weakly in voltage interval $\sim$1mV above the tunneling onset voltage, and rapidly decreases versus voltage above that interval. A voltage-driven mechanism explaining this nonlinear suppression of magnetic hysteresis is presented, where the key effect is a magnetization blockade due to the addition of spin-orbit anisotropy ϵ_{SO} to the particle by a single electron. A necessary condition for the particle to exhibit magnetization blockade is that ϵ_{SO} increases when the magnetization is slightly displaced from the easy axis. In that case, an electron will be energetically unable to access the particle if the magnetization is sufficiently displaced from the easy axis, which leads to a voltage interval where magnetic hysteresis is possible that is comparable to ϵ_{SO}/e, where e is the electronic charge. If ϵ_{SO} decreases vs magnetization displacement from the easy axis, there is no magnetization blockade and no hysteresis.

5.1 Introduction

The loss of magnetic hysteresis in nanomagnets arises due to the irreversible coupling of a magnetic sample to its environment, and is well understood in the case of thermal

equilibrium [32,106,152]. In this article, we address the loss of magnetic hysteresis in the case of a voltage-biased nanomagnet. Such a nanomagnet is attached to electric leads via two high resistance tunneling junctions, and the electron transport through the nanomagnet at low temperatures exhibits Coulomb blockade and sequential electron tunneling. Prior measurements of voltage biased single magnetic molecules, in a double tunneling barrier device, showed no magnetic hysteresis, even at temperatures much lower than the blocking temperature. [34, 76] In contrast, bulk measurements in ensembles of such molecules show hysteresis at low temperature [49, 143]. Recent scanning tunneling microscopy experiments show that antiferromagnetic and ferromagnetic spin chains of only a few atoms can display hysteresis, though the lifetimes of ferromagnetically stable states are much shorter [85, 97]. In single Co particles a few nm in diameter, in a double tunnel barrier device, electron transport measurements find hysteresis [41, 58, 74]. In this article we find that voltage-biased single Ni particles 2-3nm in diameter lie at the threshold of stable magnetic hysteresis. While some of our Ni particle samples do not display magnetic hysteresis at low temperature and low bias voltage, other Ni particle samples display hysteresis in current versus magnetic field. In the latter case, we find that the magnetic switching field is initially weakly dependent on bias voltage. But at voltages $\sim$1mV above the voltage threshold for sequential electron tunneling, the magnetic switching field quickly diminishes with further increase in bias voltage, and the signatures of magnetic hysteresis are quickly lost. This property is explained in this article in terms of bias voltage control of magnetic hysteresis. The possibility of bias voltage-control of magnetization dynamics in a voltage-biased ferromagnetic nanoparticle was first proposed by Waintal and Brouwer. [147] In their proposal, the magnetization relaxation time is tunable by the bias voltage and temperature. Their model has limited scope, however, because the spin-orbit (so) interaction is taken into account only trivially, by the simple uniaxial magnetic anisotropy energy of the particle. The effects of so-shifts (ϵ_{SO}) of discrete

energy levels were not considered. Since ϵ_{SO} in transition metal particles ($\sim$ 1meV) is much larger than the magnetic anisotropy energy (per spin, $\sim$ 0.01meV), [36, 41, 58] the model does not apply to realistic transition metal ferromagnetic particles. In this work, we extend the model from Ref. [147] to include the spin-orbit shifts of discrete levels, and find that the extended model explains our results well. We find that the necessary condition for magnetic hysteresis is that ϵ_{SO} increases in response to magnetization movement from the easy axis, due to an effective magnetization blockade. If the condition is satisfied, the voltage scale governed by ϵ_{SO} determines the bias voltage range where hysteresis can be detected. If ϵ_{SO} decreases in response to magnetization displacement from the easy axis, then magnetic hysteresis will be unstable with respect to sequential electron tunneling.

The outline of this chapter is as follows. In the next section, we describe the measurements of magnetization dynamics as a function of temperature and bias voltage, and the differential conductance spectra characteristics. Next, we introduce the basic theory and numerical models to explain the main effects observed in the experimental section. Next, we describe the detailed theory behind our observation of an effective magnetization blockade induced by voltage control of hysteresis. Finally, we summarize our main results and point to future research areas.

5.2 Experimental Methods

As shown in Fig. 5.2(a) and (b), our samples consist of one or few Ni particles immersed between two Al leads in a high-resistance aluminum-oxide double tunnel junction. The sample fabrication process has been described in our earlier work [74], and additional details are given in appendix A. Fig. 5.2(b) shows the image of Ni particles created by the fabrication process. The $I(V)$ curve of a Ni sample at $T =$ 0.06K and an applied magnetic field of $B = 0.5$T is displayed Fig. 5.2(c) . The sample exhibits clear Coulomb blockade, which is the low voltage region where the

current is negligibly weak.

To determine if the particle has magnetic hysteresis, a magnetic field is applied parallel to the film plane. The bias voltage and temperature are held fixed, and the current is observed while sweeping the magnetic field slowly, at low temperatures.

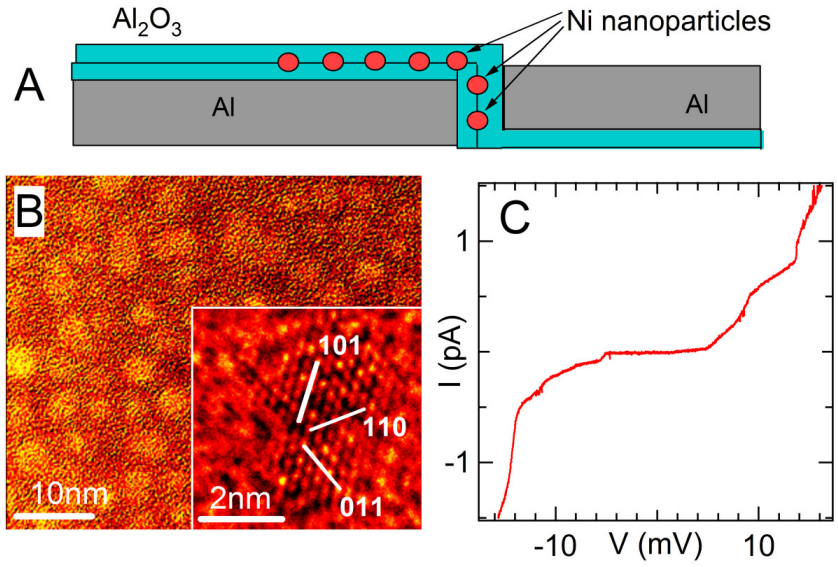

Figure 5.1: Experimental arrangement of tunneling through single Ni particles. (A) Double barrier tunneling geometry. (B) Transmission Electron Micrograph of Ni particles on amorphous Al_2O_3 background. Inset: zoomed figure that displays crystal facet of Ni particle. (C) Current (I) vs. voltage (V) curve at $B = 0.5$T and $T = 0.06$K.

We study the effects of magnetization dynamics in the Ni particle by measuring the following quantities: (1) temperature dependence of the magnetic switching field at fixed bias voltage, (2) bias voltage dependence of the magnetic switching field at fixed temperature, and (3) tunneling spectra and current noise versus magnetic field. Five Ni particle samples from the same sample fabrication batch have been studied, and are mounted in the dilution refrigerator at the same time. Only two of the five samples display magnetic hysteresis in tunneling current versus magnetic field at low temperature and bias voltage, while the remaining three samples show no detectable hysteresis at 0.06K temperature, for any bias voltage. For the presentation in this

paper, we select a representative sample that displayed magnetic hysteresis at low temperatures and bias voltage. The samples displaying no magnetic hysteresis will be discussed in a separate publication. The second sample that exhibits magnetic hysteresis reproduces the key observations from Ni sample 1.

5.2.1 Temperature Dependence of the Switching Field

First, we study the hysteresis of the tunneling current vs. magnetic field, as a function of temperature at fixed bias voltage.

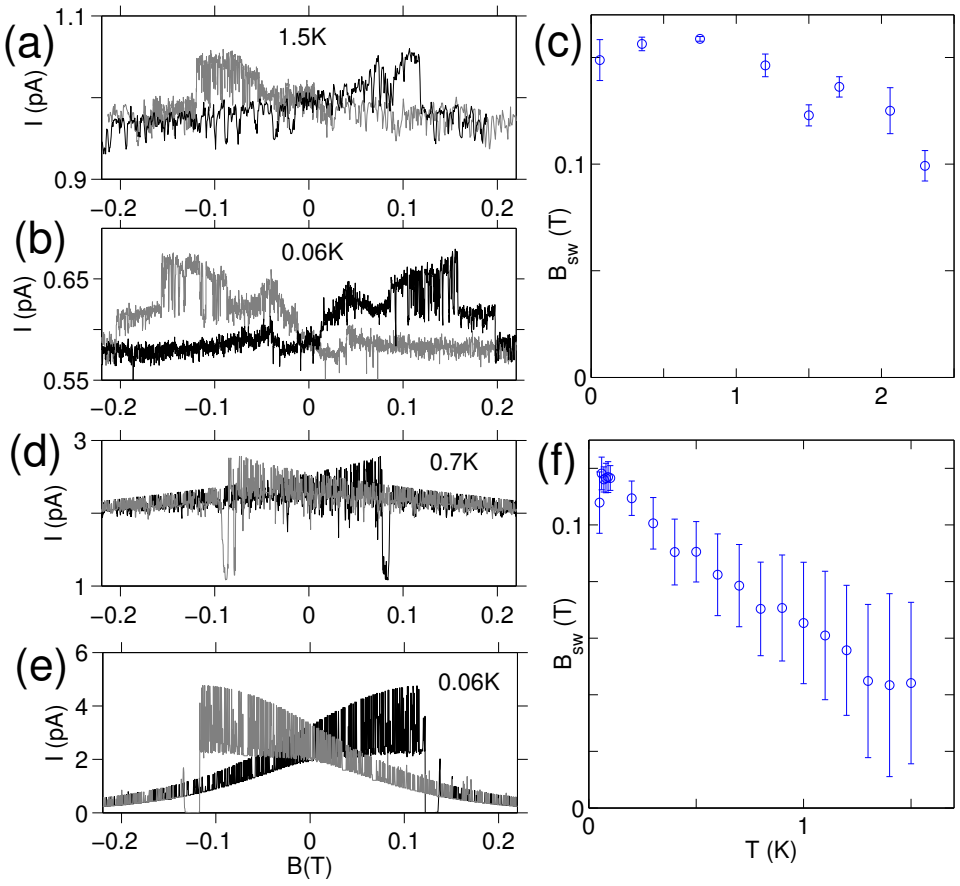

Figure 5.2: Hysteresis loops in current versus magnetic field and temperature dependence of switching fields. (A),(B) Representative measured hysteresis loops of the Ni sample. Gray (Black) curves corresponds to decreasing (increasing) magnetic field sweep direction. (C) Temperature dependence of the switching field averaged over 10 sweeps of magnetic field. (D),(E) Simulated hysteresis loops at different temperatures. (F) Simulated switching field vs. temperature as taken over 50 simulation runs. Error bar indicate ± standard deviation.

Figs. 5.2(a) and (b) display hysteresis loops in current versus magnetic field, at $T = 1.5$K and $T = 0.06$K, respectively, at a bias of 7.8mV.The sweep rate in Fig. 5.2 is 0.07T/min.In Fig. 5.2(a), the magnetic field range ± 0.5T, but the figure shows a zoomed color scale image of a scan in current versus negatively-sweeping magnetic field at rate 0.07T/min, while the bias voltage is slowly increasing from 6.0mV to 12.0mV, at a rate 0.0067mV/min. In the supplementary data in the appendix, the voltage is increased slowly from 4.5mV to 11.0mV at a rate of 0.035mV/min, while the magnetic field is swept more quickly in the interval ± 0.25T at a rate 0.07T/min in the negative sweep region $0 \rightarrow$-0.2T, and 0.28T/min elsewhere. There is pronounced current noise, in the form of downward spikes in current. After such a spike, current generally returns back to the value before the spike. The magnetic field locations of the spikes are random and not reproducible between repeated field sweeps, so the spikes represent noise. In addition to the noise, however, one can see that the current switches between two different values in the vicinity of ± 0.12T at $T = 1.5$K and ± 0.16T at $T = 0.06$K in Fig. 5.2(a) and 5.2(b), respectively. Those switches are reproducible between different sweeps, with the standard deviation of the switching field shown by the error bars in Fig. 5.2(c). Similar to the work in Refs. [41, 58, 74], the switching fields as measured from the current switches will be identified here as the magnetic switching fields of the Ni particle. Fig. 5.2(b) shows the temperature dependence of the switching field at 7.8mV. At each temperature, 10 magnetic hysteresis loops are measured, to obtain the average switching field. The largest temperature where magnetic hysteresis is resolved is 2.3K. Above that temperature, there is a loss of magnetoresistance contrast at the expected switching field. The extrapolated temperature where the switching field goes to zero (similar to the blocking temperature T_B) is $\sim 4 - 5$K. In comparison, in previously studied similarly sized Co particles, which had magnetic hysteresis at 4.2K, the extrapolated temperature for the suppression of magnetic hysteresis was $\approx$ 12K. [74] The blocking temperature in

our Ni nanoparticle is comparable to that of a magnetic molecule Mn-12 [129]. Figs. 5.2(d),(e), and (f) display numerical simulations that will be discussed in the theory section of the paper. In that section, we will estimate the size of the particle and find a diameter ≈2-3nm. We note that the measured switching field versus decreasing temperature saturates at $\sim$ 1K.

5.2.2 Hysteresis dependence on voltage bias

Next, we discuss our measurements of the current versus magnetic field at $T = 0.06$K, as a function of the bias voltage applied across the particle, and discuss the main result of the paper. Fig. 5.2.2(a) displays the experimental data in the form of single sweeps of current vs. a decreasing magnetic field, for different bias voltage values. Fig. 5.2.2(b) contains line profiles taken from individual constant-bias sections of Fig. 5.2.2(a). The line profiles are offset by 0.08pA for clarity. One notable feature in Fig. 5.2.2(a) and 5.2.2(b) is the symmetric positive peak in current versus field, of width $\sim$ 30mT centered at 0T. the peak is an artifact arising from the field reversal in the superconducting magnet. The artifact disappears when the sweep rate is sufficiently but impractically reduced, and thus will not be discussed further.

The magnetic switching fields are marked by arrows in Fig. 5.2.2(a) and 5.2.2(b). Our main result is that the magnetic switching field is weakly dependent on voltage in the interval $6.5 - 9$mV, and drops rapidly between 9 and 10mV, while above 10mV, there is a loss of magnetoresistance contrast at the anticipated switching field. At low voltages, below the onset of tunneling current, there is also a loss of magnetoresistance contrast at the switching field because the current is too small to be resolved. The tunneling current increases relatively quickly in the voltage interval $6.5 - 9$mV, where the switching field is constant (that is, $\Delta I_1 \approx 0.4$pA over this bias range). However, the current is only weakly changing over the narrow voltage regime where the magnetic switching field is reduced (that is, $\Delta I_2 \approx 0.05$pA). So, it can be concluded that the

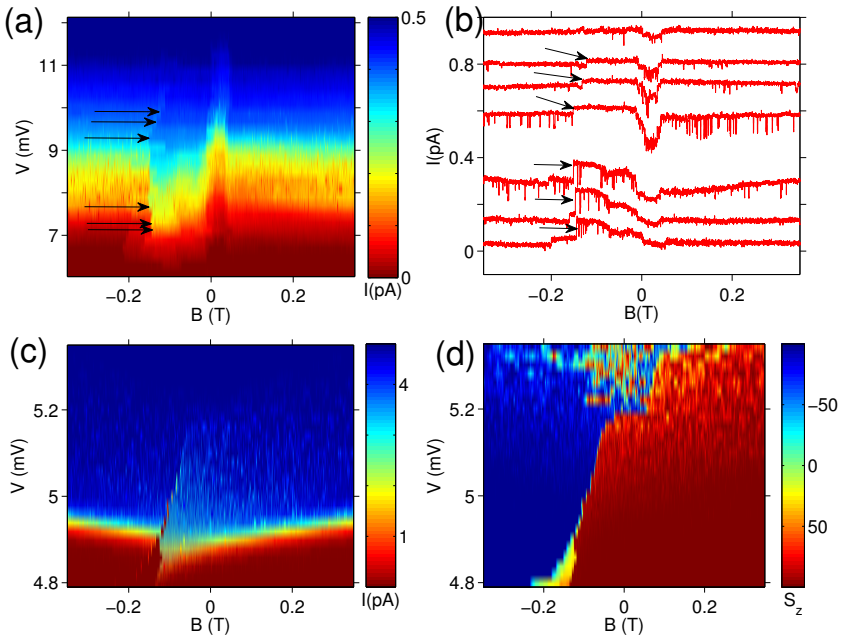

Figure 5.3: Colorscale plots of dependence of hysteresis on the applied bias voltage. In all cases, magnetic field is only swept from right to left. Black arrows correspond to magnetic switching events. (A) Experimental data of hysteresis in current as a function of magnetic bias voltage V. (B) Data slices at constant voltage values of 7.1,7.3,7.7,9.3,9.7,9.9, and 10.7 mV, taken from colorplot in (A). Each slice is offset vertically by 0.08pA for visual clarity. (C) Simulation of hysteresis of particle current as a function of V. (D) Simulation of hysteresis of particle magnetization projection on z-axis as a function of V.

magnetic hysteresis suppression is bias-voltage driven, rather than proportional to the tunneling current as in our previous work [74]. In the power range $(0, 3.6)$fW the switching field is nearly constant, while it takes only an additional 0.5fW to suppress the switching field above 9mV. This shows that the effect is not due to simple heating, which would be proportional to the power. Further evidence that heating is not responsible for the suppression of magnetic hysteresis is supplied by the width of the spectral levels in high field, and will be discussed in the next section. Additional data on bias voltage dependence of magnetic switching field, over a wider voltage range than here, are provided in appendix C.

5.2.3 Tunneling Spectra

In a voltage biased quantum dot, the differential conductance (dI/dV) versus bias voltage at low temperature is known as the tunneling spectra, due to the fact that the differential conductance peaks map to quantum levels of the particle. At voltages corresponding to such peaks, the Fermi level in one of the leads is equal to the energy difference between the final and the initial quantum state of the particle, after and before a single electron tunneling event, respectively. In our Ni particles, while magnetic field sweeps at fixed voltage bias display both current noise in the form of spikes, and reproducible magnetic switching at low voltage, as already discussed, the tunneling spectra for a given sample possess a higher complexity. In the measurement of the tunneling spectra vs magnetic field, the magnetic field sweeps slowly while the bias voltage sweeps more quickly.For the differential conductance measurements of Fig. 5.2.3(a), the field was swept from -11.5 T to +11.5T at a rate of 41mT/minute. Simultaneously, the voltage was swept in a triangle wave from 0mV to 17.1 mV at a rate of 4.39mV/minute. The current noise leads to strong noise in differential conductance, making identification of the magnetic switching field in the tunneling spectra difficult. A further complication is that the spectra may not display hysteresis as a function of magnetic field; that is, the presence of hysteresis vs. magnetic field in a given conductance spectra is dependent on the voltage range where the spectra is measured.

Fig. 5.2.3(a) displays the tunneling spectra of Ni sample 1 in a voltage interval $4-12$ mV and a magnetic field interval of $\pm$11.5T. The noise in differential conductance is manifested as apparent speckle noise over the large voltage bandwidth in the low magnetic field region. However, in the higher field regime, the noise is reduced as the spectral width of the lowest level sharpens into two linear functions of field. This is shown in Fig. 5.2.3(b) and 5.2.3(c), which show data slices of Ni sample 1 at $B = 0.2$T and $B = 11.3$T, respectively, taken from Fig. 5.2.3(a). In Fig. 5.2.3(b), over wide

voltage bandwidth, the differential conductance exhibits noise and rapidly oscillating values, while in Fig. 5.2.3(c), the noise is much less pronounced. Rather, the spectra have collapsed into a smaller voltage range.

The full width-half maximum (FWHM) of the lowest conductance peak can be obtained by fitting the conductance peak to a Gaussian function, which is indicated by full line in Fig. 5.2.3(c). The fit leads to a FWHM of 220μeV. The FWHM can be related to the electron temperature T_e in the leads as $k_B T_e < FWHM/3.5(1 + c_1/c_2) = FWHM/7.7$, leading to electron temperature of approximately 0.3K. Here, $c_1/c_2 \approx 1.2$ is the capacitance ratio obtained from the ratio of the current onset voltage at positive and negative bias, and 3.5 is from the FWHM of the derivative of the Fermi function. Since the electron temperature is much smaller than the temperature below which the switching field saturates (see Fig. 5.2), it confirms that sample heating cannot be responsible for the bias voltage dependence of the switching field.

Fig. 5.2.3(d),(e),(f) display the numerically simulated spectra, showing qualitative agreement with the magnetic field dependence of the observed conductance speckle noise and bandwidth. This will be further discussed in the theory section of the paper.

5.3 Modeling using Master Equations

We model the physics of electron transport through Ni particles using two magnetic Hamiltonians, and assume that the particle is in the sequential electron tunneling regime, wherein the electron number on the particle alternates between N and $N+1$. The particle magnetic Hamiltonian therefore alternates between H_0 and H_1, where $H_0 = -KS_z^2/S_0 + 2\mu_B B S_z$ and $H_1 = H_0 + \epsilon \left[\cos\theta_{\rm SE} S_z + \sin\theta_{\rm SE} S_x\right]^2 / S_0^2 + \epsilon_z S_z^2/S_0^2 + E_0$. where B is the magnetic field. S_0 is the ground state spin of the N-electron particle, in units of $\hbar$. For the sake of notational simplification, we have not written explicitly

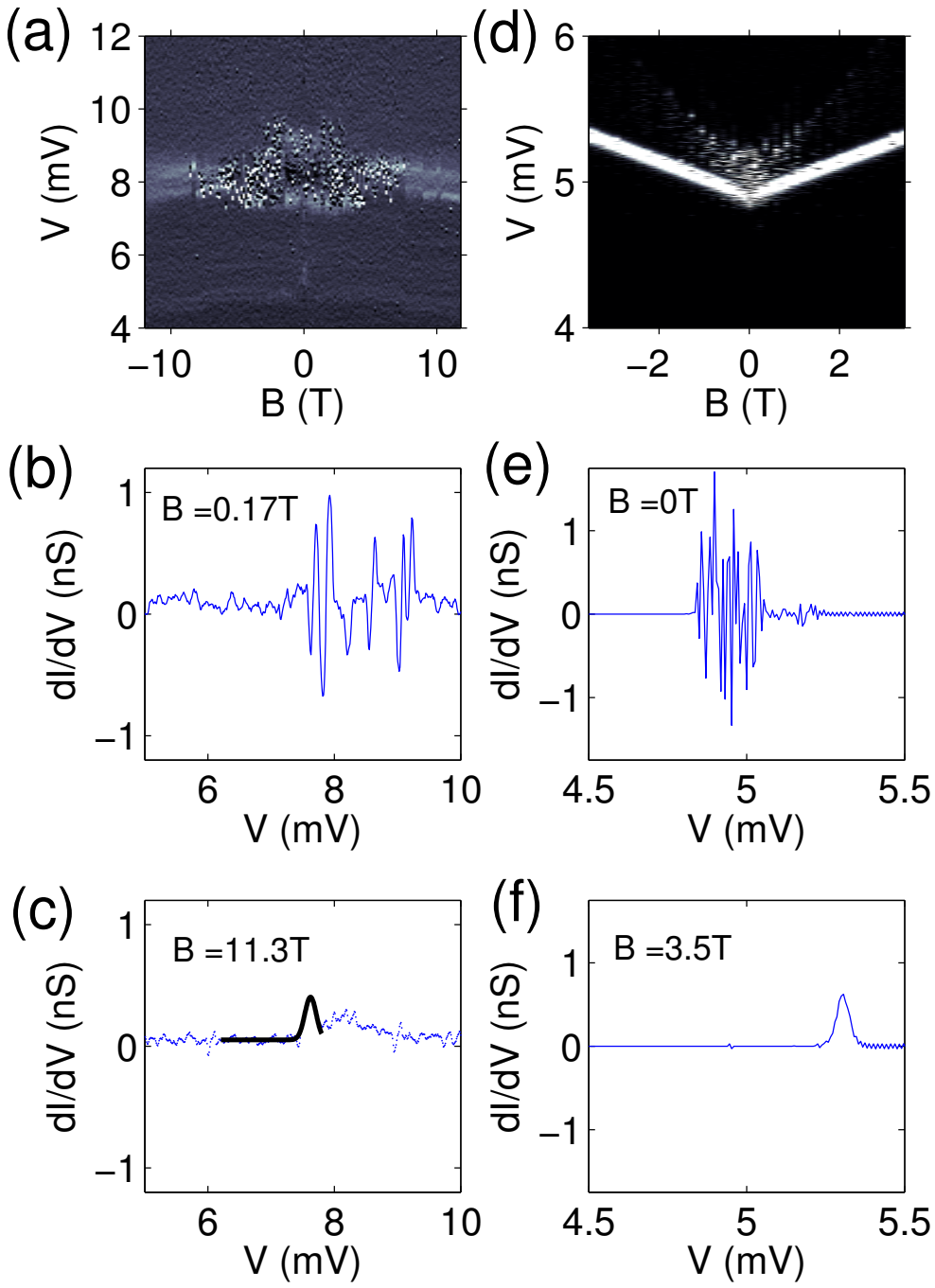

Figure 5.4: Differential conductance spectra (dI/dV vs. V). (a)Experimental data of differential conductance spectra. The gray-scale range is between -0.1 nS (dark) and 0.8 nS (light). (b) and (c) display display the line profiles in conductance taken from $B = 0.17$T and $B = 11.3$T, respectively. The offset smaller curve in (c) is a local Gaussian fit to the level. (d) Simulations of the differential conductance spectra given by the main Hamiltonian considered in this paper. (e) and (f) display simulated dI/dV curves at zero and 3.5 Tesla, respectively, taken from the gray scale in (d).

that S_0 changes by 1/2 upon the electron tunneling event. This alters the spin operators, and require the use of Clebsch-Gordan coefficients upon transforming the size of the spin space. While we have included such effects in our simulations, we neglected their expression in the Hamiltonians for notational clarity. The extra terms in H_1 correspond to the anisotropy added by a single electron. To motivate this form of the single electron anisotropy, we note that the discrete electron-box levels in a transition metal ferromagnetic particle are anisotropic with respect to the direction of the total magnetization, and they fluctuate on the order of $\epsilon_{\rm SO} = \hbar/\tau_{\rm SO} \approx 1$meV due to the so-interaction. [36, 37] Here $\tau_{\rm SO}$ is the so-flip time and is estimated to be 0.58 ps for Ni particles of this size. [36] Therefore, upon the addition of a tunneling electron onto a discrete level of the particle, an anisotropy energy shift $\epsilon_{\rm SO}$ (which is played by the role of ϵ and ϵ_z) will be added to the particle Hamiltonian. Such so-shifts in a ferromagnetic nanoparticle were first studied experimentally by Deshmukh *et al.* [41] We explored a parameter space of 24 different H_1 operators by varying $\theta_{\rm SE}$, ϵ, and ϵ_z. In each case, we obtain the eigenenergies for the $N+1$ and the N electron particle $E_{N+1,\alpha}$ and E_{N,S_z}, for the eigenstates $|N+1,\alpha\rangle$ and $|N,S_z\rangle$, respectively. We also add a constant energy term $E_0 = 2.5$meV to the $N+1$ electron particle Hamiltonian, which accounts for the charging and the orbital energy contributions in a tunneling transition. We convert from energy to voltage using capacitive division between source and drain lead of 1:1.

In this article, we consider a particular realization of H_1, where $S_0 = 100$, $K = 10\mu$eV, $\epsilon = 200\mu$eV, $\epsilon_z = -200\mu$eV, and $\theta_{\rm SE} = \pi/6$, which qualitatively agrees with our measurement. Using such parameters, we simulate the time evolution of both the tunneling current through the particle, and the total magnetization of the particle, as a function of magnetic field and bias voltage. As we will show later, $S_0 \sim 200 - 300$ for our experimental particle, and $\epsilon_{\rm SO} \sim 1$meV. The reason for using spin $S_0 = 100$ in our computations is to make the simulations feasible in a reasonable time frame.

Consequently, we reduced the effective ϵ_{SO} in the simulation to maintain a comparable ratio of the total anisotropy (which scales with S_0), and ϵ_{SO}.

When modeling the effects of electron transport on the eigenstates of the particle, a common approach uses a master equation to calculate the evolution of the ensemble probability distribution, among all eigenstates of the particle, until temporal convergence is achieved [73, 147]. We will discuss such a calculation later (See appendix B for more details on the implementation process). Another, complementary method that yields simulation data with a more direct mapping to our experimental data is to calculate the magnetization and tunneling current as a function of time, assuming that the particle at each time step is in one of its eigenstates. We then calculate transition probabilities and generate a random event each time step based upon these transition probabilities in order to determine if the particle transitions to a different eigenstate for the next time step. Even with this relatively simple model, we are able to reproduce a significant number of characteristics of the experimental data, including the apparent noise in the measured current. We have confirmed that the statistical distribution histogram among different quantum states in time is the same as the ensemble distribution obtained from the solutions of the total master equation.

5.3.1 Modeling Temperature Dependence of Switching Field

As in the experiment, simulations are carried out at a fixed bias voltage. The voltage in the source lead is fixed at 4.9mV, which corresponds to the energy of tunneling current onset at the edge of the Coulomb blockade at zero applied magnetic field and the particle in the spin-ground state. The Fermi function value of 0 is assumed in the drain lead. The magnetic switching field $B_{sw}(T)$ as a function of temperature is determined from the switches (that is, largest discontinuity) as observed in both current and magnetization. The effect of changing the particle temperature is taken into account in the simulations only through the shape of the Fermi level in the

source lead. That is, the particle receives indirect temperature equilibration with the environment through the transport of electrons, rather than explicitly linking the particle to a thermal bath. Fig. 5.2(d) and 5.2(e) display simulated hysteresis in current for two representative values $T = 0.7$K and $T = 0.06$K, and Fig. 5.2(f) shows the average simulated switching fields vs. temperature, with the error bar indicating $\pm$ standard deviation. The noise in the current hysteresis loop increases in magnitude as the field approaches the switching value. The results are in good qualitative agreement with our experimental data.

The blocking temperature in the simulation is $\approx$ 2K, approximately two times smaller than that estimated from measurements, while the magnetic switching fields near zero temperature are comparable between measurement and simulation. Since the blocking temperature generally scales with the size of the particle, [32,106] we can conclude that the measured particle is two times larger in volume than the simulated particle, or $S_0 = 200 - 300$, which corresponds to the particle diameter in the range 2-3nm, in agreement with the transmission electron micrograph in Fig. 5.2.

5.3.2 Modeling Bias Voltage Dependence of Switching Field

The simulated negatively-swept hysteresis curves in the colorplots of Fig. 5.2.2(c) and (d) were calculated using the same scheme as in the temperature dependent scans, but we varied the bias voltage for each sweep and held the temperature fixed at $T = 75$mK. In the simulations, we can also observe the particle magnetization directly. In Fig. 5.2.2(d), the magnetic switch is indicated by the sudden shift from red to blue, and is well-defined and slowly varying over a large voltage range. Once the bias reaches 5.16mV, the magnetic switch becomes unstable and the switching field value decreases quickly. For bias values above 5.18mV, the magnetization switches at random fields. In Fig. 5.2.2(c), the simulated tunneling current, rather than the magnetization, is displayed.

The simulation data in Fig. 5.3.2 consists of individual line profiles from the colorplots of Fig. 5.2.2(c) and 5.2.2(d), plus data from the other field sweep direction. At the lower bias values in 5.3.2(a),(b), the switches in current and magnetization occur at clear, reproducible values. The magnetization vs. field begins to exhibit small-amplitude noise as the field approaches the switching field, but the amplitude of noise in the current relative to average is much higher than the corresponding relative noise in the magnetization. However, in Fig. 5.3.2(c), the current has already reached its saturated value for the higher bias voltage value, and thus the magnetization in Fig. 5.3.2(d) exhibits no hysteresis, but rather, random switching events. When current becomes saturated at the highest bias values, fluctuations in current diminish, but the switch is no longer resolvable. It is precisely this high bias voltage region of current saturation where the switching of the magnetization exhibits the most noise. This is in good agreement with our experimental data in Fig. 5.2.2(a), where the switching field varies little over a large current range, but quickly falls of when the voltage is raised further, while the current noise is suppressed above that voltage.

5.3.3 Modeling Energy Spectra and Noise

The numerical simulations of the tunneling spectrum versus magnetic field are displayed by the gray scale image in Fig. 5.2.3(d). As with our measured spectra, there is significant noise in the conductance at low field in the simulation, which appears as speckle noise at low field values of the differential conductance spectra. Fig. 5.2.3(e) and (f) show data slices taken from the simulation data at $B = 0\text{T}$ and $B = 3.5\text{T}$, respectively. In Fig. 5.2.3(f), the noise in conductance is reduced, and there is only a single smooth peak. This directly reproduces the qualitative structure observed in the experimental data and provides very good visual agreement; that is, there is clear noise in the spectra in the low field regions, but the noise is diminished in the high field regions. The reason for the difference in magnetic field scale between Fig.

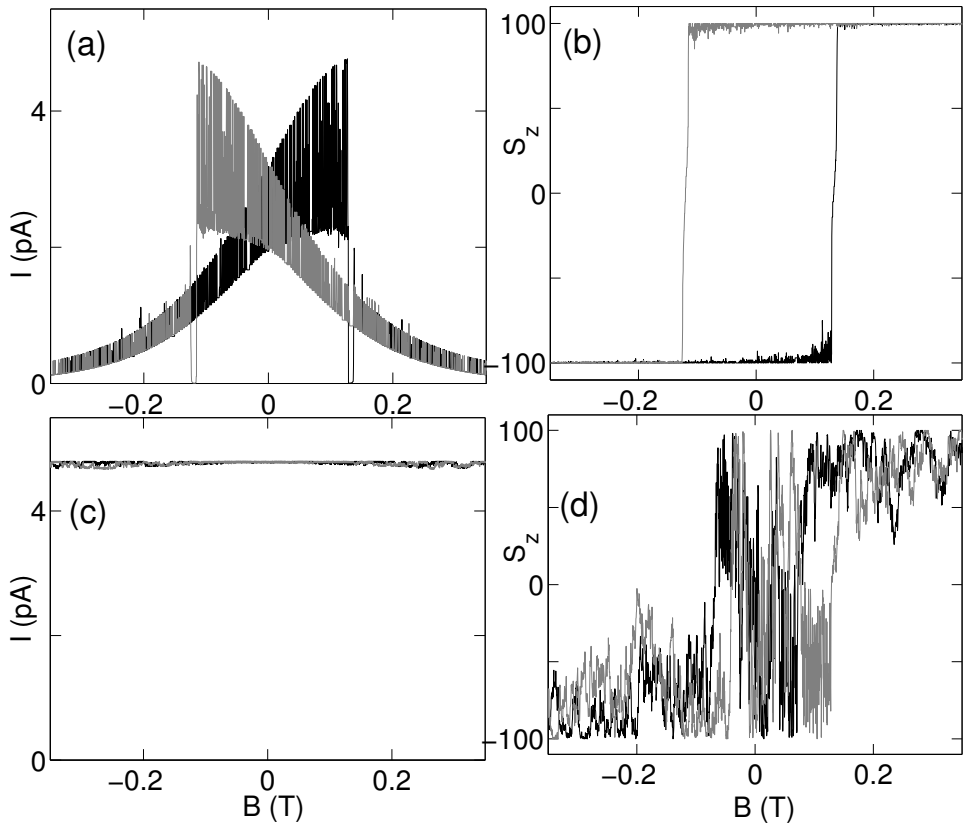

Figure 5.5: Data slices taken from the simulation in Fig. 3-B,C. (A),(C) Simulated current hysteresis loops at $V_L = 4.90$meV and $V_L = 5.28$meV, respectively. (B),(D) Corresponding magnetization hysteresis loops at $V_L = 4.90$meV and $V_L = 5.28$meV, respectively. Gray (black) correspond to data taken from a decreasing (increasing) field sweep.

5.2.3(a) and Fig. 5.2.3(d) in both bias voltage and magnetic field range again lies with the fact that our simulations used smaller spin (and therefore total anisotropy) and corresponding smaller ϵ_{SO} than in the experimental case.

5.4 Understanding of Voltage Control of Hysteresis

As discussed in the previous section, there is a good qualitative agreement between the observed parameters and master equation simulations. The purpose of this section is to illuminate the physics of bias voltage control. The model of voltage control of hysteresis can be understood from the perspective of an effective magnetization blockade, similar to the well known spin blockade phenomenon studied previously in

semiconducting quantum dots. [68, 78, 92, 95, 109, 121, 130] In the case of spin blockade, the tunneling current through consecutive quantum dots is diminished due to the Pauli exclusion principle. In the case of magnetization blockade, the motion of the magnetization is blocked in the neighborhood of the easy axis, due to the interplay between Coulomb blockade and the energy cost associated with deflecting the magnetization at too large an angle away from an easy axis. Consider first the case where ϵ_{SO} increases as the magnetization is displaced from the easy axis. If the bias voltage is low compared with ϵ_{SO}/e, then the potential energy in the leads cannot supply enough energy for the particle to transition into the excited magnetization state (that is, an electron cannot tunnel onto the particle to displace the magnetization beyond a maximum angle determined by the bias voltage), and thus the magnetization remains localized near the easy axis. Once the bias voltage is raised past ϵ_{SO}/e, however, the electron can surmount the magnetization blockade and tunnel into higher particle magnetization states. Next, consider the case where ϵ_{SO} decreases as the magnetization is displaced from the easy axis. In this situation, there is no hindrance to electron transport because further displacements of the magnetization from the easy axis require decreasing amounts of energy. This runaway effect causes the magnetization to displace arbitrarily far from the easy axis as soon as the tunneling process has been initiated.

In the remainder of this section, we will explain this phenomenon of magnetization blockade in detail. In the simulations that follow, we will assume that the applied magnetic field is zero. As discussed earlier, the eigenenergies for the $N+1$ and the N electron particle are labeled $E_{N+1,\alpha}$ and E_{N,S_z}, for the eigenstates $|N+1,\alpha\rangle$ and $|N,S_z\rangle$, respectively. The values $\alpha = 0, 1, 2, ...$ are sorted in order of increasing $\langle\alpha|S_z|\alpha\rangle$. In the vicinity of the energetic minimum with negative $\langle\alpha|S_z|\alpha\rangle$, α also sorts the excited states of the $N+1$ electron particle, that is, $E_{N+1,\alpha}$ increases versus α for the Hamiltonian that we use.

We found that the tunneling density of states (DOS) is a useful structure to explain how voltage controls magnetization dynamics. For the aforementioned realization of H_0 and H_1, Fig. 5.6 displays the results for the tunneling density of states (DOS) for the N-electron particle with spin component S_z, where we define $DOS(S_z, E) = \sum_{\alpha} |\langle N, S_z | N+1, \alpha \rangle|^2 \delta(E_{N+1,\alpha} - E_{N,S_z} - E)$. The $\delta-$functions are broadened by convolving with a Gaussian of width 1μeV. The darkest regions correspond to zero DOS, while the white corresponds to the maximum DOS.

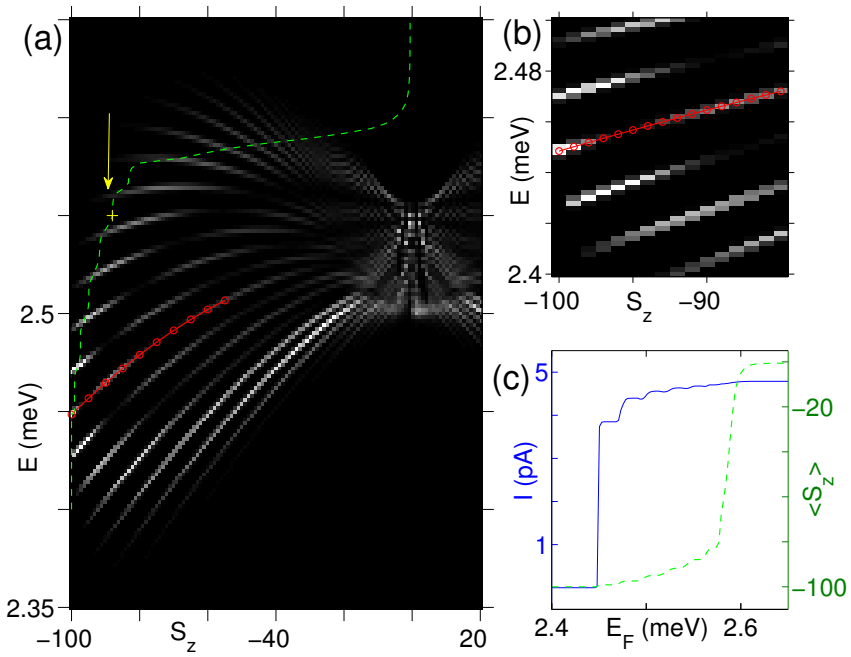

Figure 5.6: Master equation simulations: (A) Tunneling density of states. Red, solid curve with circle markers corresponds to non-magnetic transitions. Green dashed curve corresponds to calculated $\langle S_z \rangle$ as bias voltage is ramped upwards. (B) Zoomed region of the DOS from (A), displaying a so-shifted level increasing as a function of magnetization-displacement from easy axis. (C) Current (blue solid line) and $\langle S_z \rangle$ (green dashed line) vs. bias Fermi energy curves.

We simulate the single-electron-tunneling using a master equation following the procedure described in Ref. [147], to determine field and bias dependence of the converged probability distribution P_{N,S_z} and $P_{N+1,\alpha}$ of quantum states of the particle (see Appendix for more details). The source Fermi level energy of 2.45meV (or a bias voltage of 4.9mV) corresponds to the onset of tunneling at the edge of the Coulomb

blockade. In this section, we discuss the bias in terms of energy rather than voltage. As mentioned previously, the conversion from voltage to energy requires capacitive division, which amounts to a factor of 2 difference between the two quantities. The Fermi function in the drain lead is set to 0 for the energy range in Fig. 5.6.

The white curves in the grayscale image of Fig. 5.6(a) represent energies of various tunneling transitions between the magnetic states of the N and $N+1$ electron particle, as a function of the initial state of the N electron particle. The distance between the curves along the y-axis is dictated by the magnon excitation energy (20μeV for this case). The tunneling transitions in the DOS span an energy range determined by ϵ_{SO}, which is an order of magnitude larger than the magnon energy. Fig. 5.6(b) shows zoomed-in DOS in the vicinity of $S_z = -S_0$. Note the transition indicated by circle markers connected with a line. At $S_z = -100$, the total DOS below the circle-marked line is zero. This indicates that, for the N-electron particle in the ground state, the tunneling transition indicated by the circle-marked line has the lowest energy, which means that after the transition the particle will be in the N+1-electron ground state. If initially $S_z = -S_0 + 1$, there will be only one tunneling transition with energy below the circle-marked line, which will be the transition from the first excited state of the N electron particle to the ground state of the $N + 1$ electron particle. In such transition, the magnetic energy decreases. Overall, the circle-marked line indicates nonmagnetic transitions $|N, -S_0 + n\rangle \rightarrow |N + 1, \alpha\rangle$, where $\alpha = n$. The curves at energies above (below) the energy of the nonmagnetic transition, correspond to the magnetically exciting (relaxing) transitions, in which $\alpha > n$ ($\alpha < n$).

In the vicinity of $S_z = -S_0$, the integral of the DOS over magnetically exciting transitions (i.e. the total weight for the transitions above the circle-marked line) is slightly higher than the integral over magnetically relaxing transitions. Consequently, if E_F in the source lead is above all tunneling transition energies, there will be a net positive energy inflow from the lead into the magnetic subsystem. Similarly, we find

that the electron outflow to the drain also produces a net positive energy inflow into the magnetic subsystem. However, if E_F in the source lead is reduced to lie within the energy range spanned by the white curves, then the Fermi function in the source lead will suppress some magnetically exciting transitions. The net energy flow into the magnetic subsystem can be negative, which means that the magnetic relaxation time is finite. A similar effect was studied in Ref. [147]. Due to this relaxation, a steady state value of S_z will follow.

As an example, consider the N electron particle initially in its ground state $S_z = -S_0$, and apply a bias energy of 2.55meV. Initially, for $S_z = -S_0$, all of the DOS is below E_F. Since the total probability of the magnetically exciting transitions is higher than that for the magnetically relaxing transitions, S_z will initiate a random walk in response to the applied bias, leading to S_z increasing linearly with time. A similar magnetization random walk in the absence of so-interaction was studied previously [147]. When S_z reaches ≈ -88, as shown by the yellow cross in Fig. 5.6(a), then a magnetically exciting transition will turn on in the DOS above E_F, as indicated by the yellow arrow in Fig. 5.6(a). Since this level is energetically prohibited due to the height of E_F, the magnetic energy inflow diminishes, and $\langle S_z \rangle$ will converge to slightly above $S_z = -88$. We can conclude that the required condition for the localization of S_z near the energetic minimum at $S_z = -S_0$, which is also the condition for magnetic hysteresis, is that the energy of the magnetically exciting transitions increase as S_z shifts from the ground state value. This verifies our picture of magnetization blockade, wherein the energy conservation of the tunneling process pins the magnetization within a small localized region, inducing an effective barrier against magnetization motion. The simulations produce a striking separation in the bias voltage values where the current onset occurs and where $\langle S_z \rangle$ increases to zero, as shown in Fig. 5.6(c). The dashed green curve in Fig. 5.6 is the converged $\langle S_z \rangle$ as a function of bias energy $E = E_F$, while the solid blue curve in the Fig. 5.6(c) is the converged

$I(E_F)$ curve. So, the magnitude of the current alone is not a sufficient parameter for magnetization control. Rather, it is the bias Fermi energy that determines the control of magnetization dynamics. As we varied the parameters to study different H_1 operators, we found many Hamiltonians that would altogether prevent the possibility of magnetic hysteresis. Those H_1 operators lack magnetic levels that increase in energy as S_z shifts away from $-S_0$. This explains our numerous experimental Ni samples that showed no observable hysteresis.

5.5 Conclusions

In summary, we have presented an experimental realization of a bias voltage control of magnetic hysteresis in a ferromagnetic particle. Through master equation simulations and probabilistic eigenstate evolution equations, we have demonstrated the emergence of an energy scale from the spin-orbit anisotropy contribution from a single electron, which is able to explain how the range of magnetization motion is controlled by the applied bias, irrespective of the size of the tunneling current. A necessary condition for the bias voltage control of the magnetization is that the anisotropy contribution of a single electron increases in response to a small magnetization displacement from the easy axis. This constraining of magnetization motion within a localized orientation due to the energy conservation of the electron tunneling acts as an effective magnetization blockade. The qualitative results of our simulations agree remarkably well with our experimental data. In terms of spin based electronics, the next step could be to explore the use of voltage, rather than current, to control spin-transfer torque in a ferromagnetic particle or molecule, which would require spin-polarized drain and source leads.

5.6 Appendices

5.6.1 Sample Fabrication

Samples are fabricated by using electron-beam lithography and a shadow evaporation technique. We spin-coat a bilayer of methyl methacrylate/polymethyl methacrylate (MMA/PMMA) electron-beam resist on a SiO_2 substrate. An SEM is used to define the desired sample dimensions and geometries on the substrate. Developing the samples exposes the areas of substrate exposed to the localized electron beam. Samples are placed on a rotatable stage in a vacuum chamber, which is pumped down to 10^{-7} Torr. Layers of metal contacts and nanoparticles are evaporated in the vacuum using current-induced Joule heating of the metals. A crystal monitor is used to track the amount of metal deposited on the sample. In the first step, conducting planes of Al, 40 nm thick, are deposited, followed by 20 nm of insulating Al_2O_3 which conformally covers the conducting Al. This forms the capacitive shunt filters which divert extraneous microwave noise away from the sample electrodes. We spin-coat the samples with MMA/PMMA again and pattern the tunnel junctions. The tunnel junction consists of an Al electrode (14 nm thick) followed by a layer of insulating $Al_2O_3 \approx 1.8$ nm thick. Next a nominal thickness of 5-6 Angstroms of ferromagnetic metal are deposited, which nucleate due to surface tension and form isolated nano-islands with diameters on the order of $2-3$ nm. The lattice constant extracted from the structure in Fig. 5.2 confirms faced-centered-cubic Ni. In addition, energy dispersive X-ray spectra (EDS) demonstrate that the particles are made from Ni. Next, another layer of $Al_2O_3 \approx 1.8$ nm thick is deposited to form the other half of the double tunnel junction. Finally, a second conducting contact of Al (14 nm) is deposited. The remaining metal on the PMMA is washed away during a liftoff process in acetone. Samples are then wired up and attached to a dipstick to be inserted into the dilution refrigerator. The basic structure of the tunnel junction samples is as shown in Fig. 5.7(a), which has the capacitive ground plane beneath the tunnel junction in order to filter any

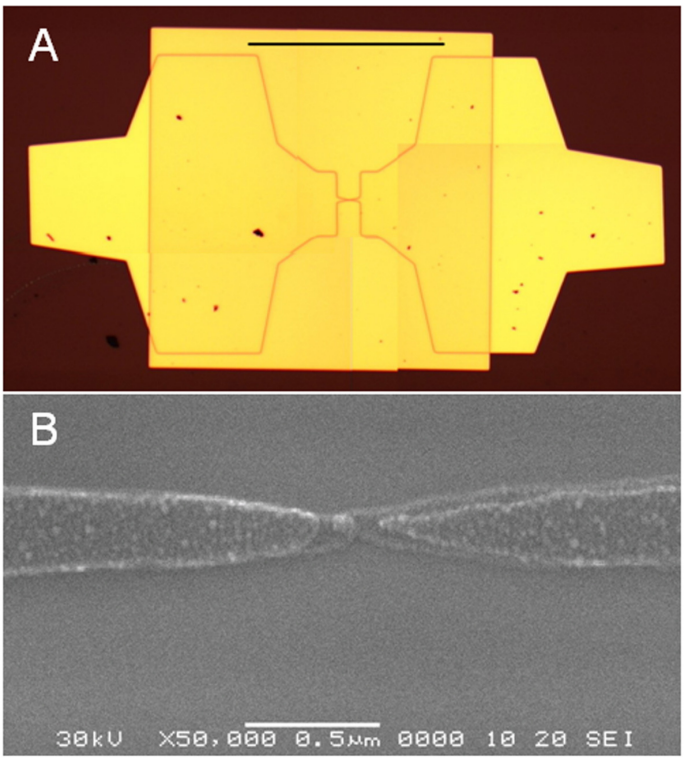

Figure 5.7: (A) Optical microscope image (stitched from multiple images of the same device) of nickel tunneling device geometry with conducting ground plane beneath. The black scale bar indicates 250 microns. (B) SEM image of typical tunnel junction device. White scale bar indicates 0.5 microns.

unwanted high-frequency signals away from the sample. A zoomed SEM image of an exemplary device junction is displayed in Fig. 5.7(b).

Samples are studied in a dilution refrigerator, and the sample leads are additionally cryogenically filtered using a high loss transmission line with an exponential cut-off at frequencies $\sim$ 10MHz. The samples sit in a Faraday cage at temperature $\approx$ 30mK. An on-chip filter in the form of a capacitively coupled ground plane lies beneath the sample, with a frequency cut-off also $\sim$ 10MHz. Typical junction resistance is $\approx G\Omega$, and typical current per discrete levels is quite low, $\sim$ 0.1pA.

5.6.2 Master Equation Simulations

The master equation utilized in our present work is adapted from references [73] and [147]:

$$\frac{\partial P_\alpha}{\partial t} = \sum_\beta \sum_{l=L,R} \sum_{\sigma=up,down} \Gamma_{l\sigma} \Big[\left|\langle\beta|c_{\mu\sigma}|\alpha\rangle\right|^2 \left(f_l(E_\alpha - E_\beta)P_\beta - (1 - f_l(E_\alpha - E_\beta))P_\alpha\right) + \left|\langle\beta|c^\dagger_{\mu\sigma}|\alpha\rangle\right|^2 \left(-f_l(E_\beta - E_\alpha)P_\alpha + (1 - f_l(E_\beta - E_\alpha))P_\beta\right) \Big]$$

The above equation determines the evolution of the probability P_α of occupation of a given particle state $|\alpha\rangle$ in time. The spin of the electron is σ, and the tunneling rate $\Gamma_{l\sigma}$ in general could be different for the source and drain leads, and could depend on the spin polarization. The time rate of change of P_α depends on the Fermi level in the source and drain leads (L and R, respectively). These Fermi functions are evaluated at the energy differences $E_\alpha - E_\beta$ between the states involved in tunneling. Each term in the sum also depends on the overlap between states $|\alpha\rangle$ and $|\beta\rangle$, upon the addition ($c^\dagger_{\mu\sigma}$) or subtraction ($c_{j\sigma}$) of an electron, where $c^\dagger_{\mu\sigma}$ is the electron creation operator for the μ^{th} level, and $c_{\mu\sigma}$ is the electron annihilation operator for the μ^{th} level.

While the total spin S_0 on the N-electron particles in our experiments is likely ~ 200, such calculations become very time consuming and computationally intensive, and since our goal with the master equation simulations was to derive qualitative results rather than a quantitative fit to our experimental data, we elected to do simulations with $S_0 = 100$. Additional parameters for our simulations include tunneling rate $\Gamma = 60$Mhz for both leads, time step $\Delta t = 1$ns, and total integration time $t = 25\mu$s. The probability distribution and magnetic energy are checked for saturated convergence in time.

We studied a Hamiltonian parameter space of $K = 10$, $\epsilon = [-200, 200]$, $\epsilon_z = [-200, 0, 200]$, and $\theta_{\rm SE} = [\pi/6, \pi/4, \pi/3, \pi/2]$. All energies are in units of μeV. Due to mesoscopic fluctuations, these adjustable parameters will vary from sample to sample, and our goal was to merely sample the large possible parameter space. Note, in order to convert from E to voltage, one needs to add the orbital, the exchange, and the

charging energy to E, and account for the capacitive division of the voltage. We assume there is only one quasiparticle state μ within the energy range of tunneling, and that the Fermi level in the drain is $-\infty$; that is, $f_R = 0$.

When determining the $I(V)$ characteristics, the state is initialized in the ground state of the N-electron particle. For subsequent bias voltage data points, the initial state probability distribution is taken as the saturated value from the previous voltage point. In this way, the progression of current and $\langle S_z \rangle$ will occur in the same way as in experiments.

The complementary simulation that we used in the calculation of the hysteresis loops and spectra involves the same Hamiltonian and evolution equation as used in the master equation simulations. One key difference, however, is that instead of evolving the probability distribution of all eigenstates in time simultaneously until temporal convergence, we initialize the particle in its ground state, and then calculate transition probabilities for each time step. That is, we integrate the master equation for one time step, and read all the transition probabilities in that time step. We then generate a random event according to those probabilities, leading to the new eigenstate for the particle before the next time step. For small time steps, the most likely event is that the particle will remain in the same state. We have tested this scheme for a given Hamiltonian and bias voltage, and found that the long-time histogram of eigenstate probabilities using this method is identical to the steady state distribution of states given by the master equation, as expected.

5.6.3 Additional Hysteresis vs. Voltage Data

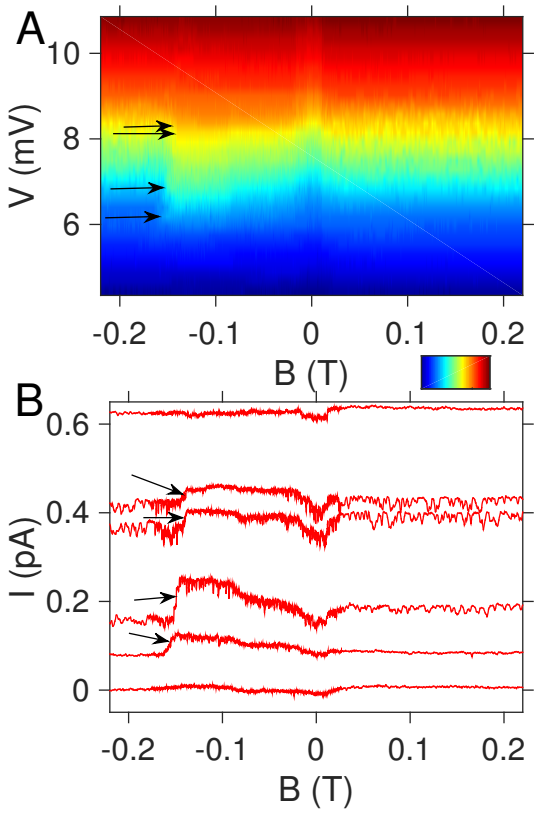

Figure 5.8: Additional voltage sweep data displaying one-sided current hysteresis loops for Ni sample 1. (A) Colorplot displaying the reproducible effect of hysteresis in a specific voltage range. Blue (Red) correspond to lower (higher) current. (B) Data slices taken at constant voltage values from the colorplot in (A). Black arrows indicate switching events. At the lowest and highest biases, switching resolution has been lost.

To emphasize the reproducibility of the importance of voltage bias, rather than current, on the hysteretic properties of Ni sample 1, we provide in Fig. 5.6.3(a) an additional colorscale plot of current hysteresis in a narrow voltage range. Fig. 5.6.3 is an average over four voltage ramps, and the the main effect as observed in the data from Fig. 5.2.2 is reproducible. Fig. 5.6.3(b) displays individual data slices from the colorplot at the following increasing voltage values: 5.4, 6.2, 6.8, 8.2, 8.4, and 10.3 mV. The curves are offset vertically for clarity.

CHAPTER VI

ZEEMAN SPLITTING OF DISCRETE LEVELS IN A SINGLE NI NANOPARTICLE

6.1 Introduction

In single normal metal nanometer-scale particles, studies of Zeeman-splitting of discrete electron-in-a-box levels have led to much information about the properties of the spin-orbit (SO) interaction in those particles. Examples of such studies include measurement of g-factors of Kramers doublets, avoided crossings, and level anisotropies in a magnetic field [2,23,31,38,118,119,125]. Such variety of effects provide complementary information about the SO-interaction, and test theories how the SO-interaction affects particle-in-a-box energy levels of the particle. In contrast to normal metal particles, tunneling spectroscopy of discrete levels in individual ferromagnetic (Co) particles with normal-metal leads, found no Zeeman splitting [41,58,73,74]. In addition, discrete energy levels versus magnetic field exhibited magnetic hysteresis, showing that electron tunneling did not perturb the magnetization of the Co particles significantly. The absence of Zeeman splitting is a sign of a strong asymmetry between the tunneling rates of spin-up and spin-down electrons, for electron tunneling from normal metal leads into or out of the ferromagnetic particle. Without the SO-interaction, those tunneling rates are given by the appropriate Clebsch-Gordan coefficients, which lead to the spin asymmetry in tunneling rate of order $\sim 1/2S_0 \ll 1$ [89]. If the SO-interaction is added to theoretical analysis of spin-up and spin-down tunneling rates, we find here that the ratio can be strongly enhanced and can approach 1, suggesting high probability to observe Zeeman splitting in a ferromagnetic particle. In single magnetic molecules, where $S_0 \sim 1 - 10$, Zeeman splitting in strong magnetic fields

has been observed, but those single molecules did not exhibit magnetic hysteresis [76]. Additionally, Zeeman split levels did not cross at zero magnetic field, which would be a hallmark spin-degeneracy. It is well known that the SO-interaction creates a gap in the spin-space energy spectrum of a ferromagnet, and zero-field splitting in tunneling spectra of magnetic molecules has been attributed to a very strong SO-anisotropy [52, 76]. In this paper we find two single Ni-particles, of diameter 2 to 3nm, that display Zeeman splitting in their discrete energy levels. The Zeeman split levels do not cross at zero magnetic field; rather, they cross at offset field values of $B = \pm 0.5$T. Additionally, we observe zero-field splitting in the differential conductance spectra. Our main result is that the ratio of the currents that flow via two Zeeman split levels is comparable to 1, indicating a strong mixing of spin-up and spin-down states in the particle wave-functions. We also observe significant curvature of the Zeeman split levels versus magnetic field, consistent with the strength of the SO-interaction, and g-factors smaller than but comparable to 2.

6.2 Experimental Methods

To probe the structure of the discrete particle energy levels and their dependence on magnetic field, we perform single electron tunneling spectroscopy measurements in a dilution refrigerator. The basic device geometry is the same as that studied in previous works [50, 51, 73, 74], and is summarized in Fig. 6.2. Samples are fabricated using electron-beam lithography and shadow evaporation techniques. The sample consists of two Al conducting electrodes, separated by a thin insulating layer of Al_2O_3, as shown in Fig. 6.2(d). Embedded within this insulating layer are Ni nanoparticles of size 2 to 3 nm. A representative Transmission Electron Microscope image of a Ni nanoparticle an an amorphous Al_2O_3 substrate is displayed in Fig. 6.2(a). The white lines in Fig. 6.2(a) indicate the primary crystal axes for the face-centered-cubic Ni. Figs.6.2(b) and (c) display $I(V)$ curves of Ni sample 1 and Ni sample 2, respectively.

The red and black curves correspond to magnetic field values. The discrete steps in the $I(V)$ curves indicate the opening of another conducting channel in the particle, which arises when one of the discrete particle energy levels becomes available for tunneling. The insets of Figs. 6.2(b) and (c) display the full $I(V)$ curves, which illuminate the well-known characteristic of Coulomb blockade in the low bias region.

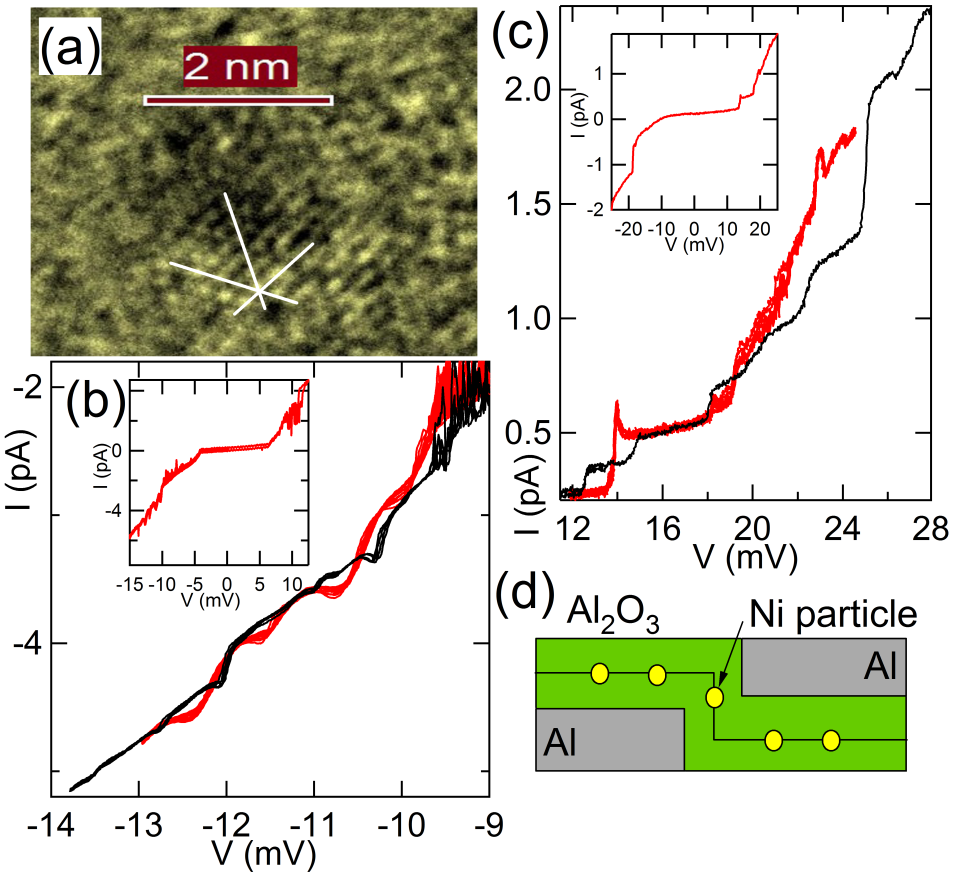

Figure 6.1: Device fabrication geometry and current measurements. (a)Transmission Electron Microscope image of Ni particle (b) Experimental current-voltage curve for Ni sample 2. (c) Experimental current-voltage curve for Ni sample 1. Red (black) correspond to low (high) magnetic field measurements. Steps in the $I(V)$ curves correspond to discrete energy levels on the Ni particles. (d) Double-tunneling barrier device connected to measurement apparatus through Al leads.

The energy level structure of the Ni nanoparticle is studied with differential conductance (dI/dV) measurements as a function of magnetic field. In these experiments,

we ramp the magnetic field slowly, and sweep the bias voltage across the particle in a triangle wave. The current response to the applied bias voltage is measured through a current amplifier. Fig. 6.2 displays differential conductance spectra from two exemplary Ni samples which exhibit zero-field splitting of energy levels, as well as Zeeman splitting of levels for magnetic fields larger than 1T.

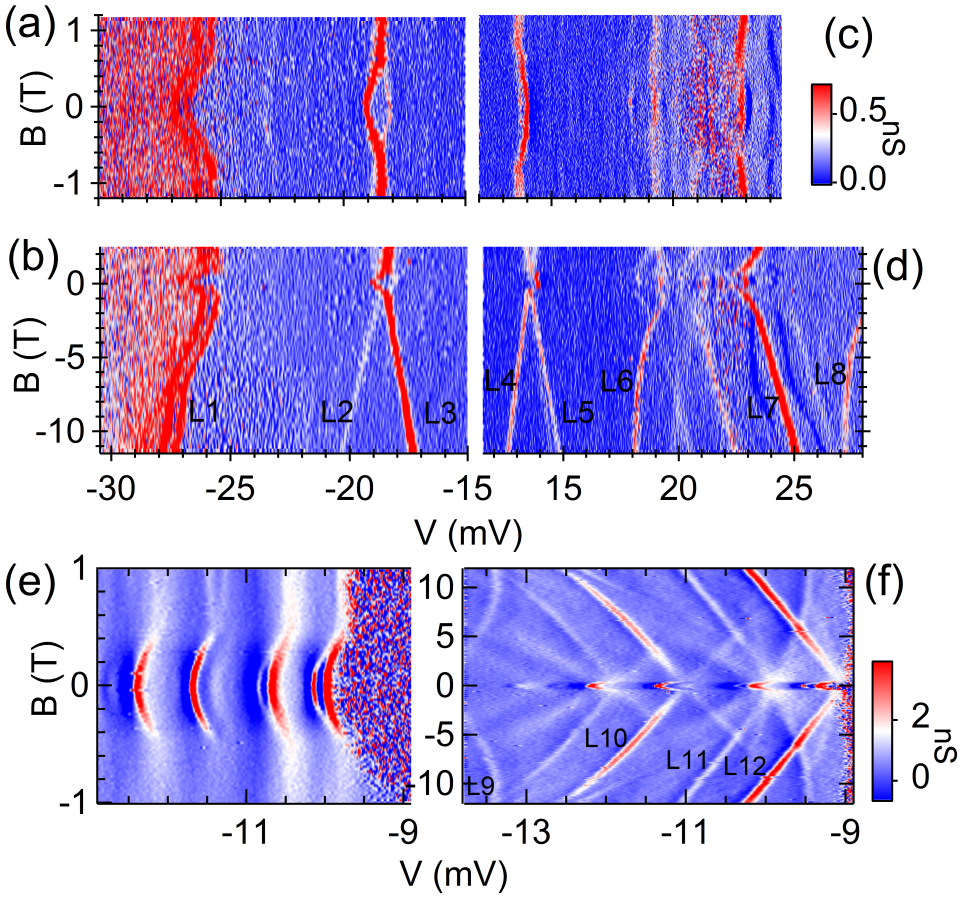

Figure 6.2: Differential Conductance spectra of 2 Ni samples exhibiting zero-field splitting and Zeeman splitting of energy levels. (a),(b) Spectra of Ni sample 1 in the negative bias voltage range. (c),(d) Spectra of Ni sample 1 in the positive bias range.(e),(f) Spectra of Ni sample 2. discrete levels are indicated by L1 through L12.

Figs. 6.2(a) and (c) present differential conductance measurements from the low magnetic field sweeps for Ni sample 1 in the cases of negative and positive bias voltage, respectively. The energy level near -19mV splits into two branches separated

by $\approx$ 1mV as it approaches $B = 0$T. Further, the additional levels in Fig. 6.2(a) on the positive and negative voltage bias regimes appear to exhibit splitting near $B = 0$T; however, these levels are also subject to more noise. Figs. 6.2(b) and (d) contain high-magnitude field sweeps for Ni sample 1. The level that exhibited zero-field splitting in Fig. 6.2(a) also exhibits Zeeman splitting, as it branches into the levels L2 and L3 that vary linearly with field in the high field regime in Fig. 6.2(b). For the lowest field values, the spectra of both samples have a broadened bandwidth, which focuses into more clearly-defined branches as the field is increased. The asymmetry in the voltage values at which conduction onset occurs results from the different tunneling capacitance values in the source and drain leads. Unlike a normal metal particle, the Zeeman splitting of our ferromagnetic Ni samples does not begin at $B = 0$T, but is instead offset by $\approx \pm 0.5$T. The first Zeeman-split level on the negative bias side bears most of the spectral weight in the L3 branch that decreases in energy as the field increases. The energy-increasing branch, L2, consequently, is weak for all magnetic field values measured. The first Zeeman-split level in the positive-bias regime, however, bears comparable spectral weight in branches marked L4 and L5 for most of the field values measured. The amplitude ratio of the Zeeman split levels as a function of magnetic field for Ni sample 1 is displayed in Fig. 6.3(a), for both the positive and negative bias voltage regions. Additionally, the levels at higher bias values in Fig. 6.2(d) exhibit nonlinear dependence on field. In Fig. 6.2(e) and (f), Ni sample 2 contains many of the same qualitative features observed in sample 1. That is, the Zeeman-split levels cross at non-zero field values. Also, there is a single branch that bears much of the spectral weight for each Zeeman-split level. Nonlinearities in the Zeeman-branches are apparent for higher field values. In each the first and third levels above the coulomb blockade (L12 and L11), the energy-increasing branch carries the larger amount of spectral weight. The second and fourth levels above the coulomb blockade carry smaller amounts of spectral weight than the first and

third levels, but they carry the weight more evenly among the energy-increasing and energy-decreasing branches. Level L9 exhibits significant curvature in the high field, as compared with the other more linear Zeeman levels L10, L11, and L12. By fitting a line to the Zeeman-split levels with little curvature, and correcting for capacitive division, we estimate effective g-factors of Ni samples 1 and 2 to be 1.9 and 2, respectively. Higher-order spin transitions are also visible in Fig. 6.2(f), and appear as levels with higher magnitude slope dE/dB.

Based on a result from second order perturbation theory, we can relate the magnitude of ϵ_{SO} to the difference in second derivatives of Zeeman levels of a given sample. If we simply compare the magnitude of the curvatures of the energy levels vs magnetic field, as shown in Fig. 6.3(b), we find good agreement with simulation data. The simulations will be discussed in a later section of the paper. The treatment based on perturbation theory yields an estimate of $\epsilon_{\mathrm{SO}} \approx 0.67$meV for Ni sample 1, and $\epsilon_{\mathrm{SO}} \approx 0.52$meV for Ni sample 2. In each of these cases, we took the difference in curvatures of levels (L1-L2), and (L9+L12) for samples 1 and 2, respectively. If we compare these values to the magnitude of the zero-field splitting of the energy in Ni sample 1, we find good agreement. After correcting for capacitive division, the ZFS of sample 1 is ≈ 0.58meV.

6.3 Simulations-Master Equations

The rich structure inherent to the magnetic spectra can be illuminated by the use of a single-electron tunneling model, as well as master equations [51]. Due to the large mesoscopic variations in our particle Hamiltonians, it is to be expected that the particular details for each spectra may vary substantially as well. Exploring the full range of every one of these mesoscopic parameters in order to perfectly fit each data set of experimental spectra would be computationally infeasible. Nevertheless, by sampling the vast parameter space of mesoscopic variations, we can reproduce a

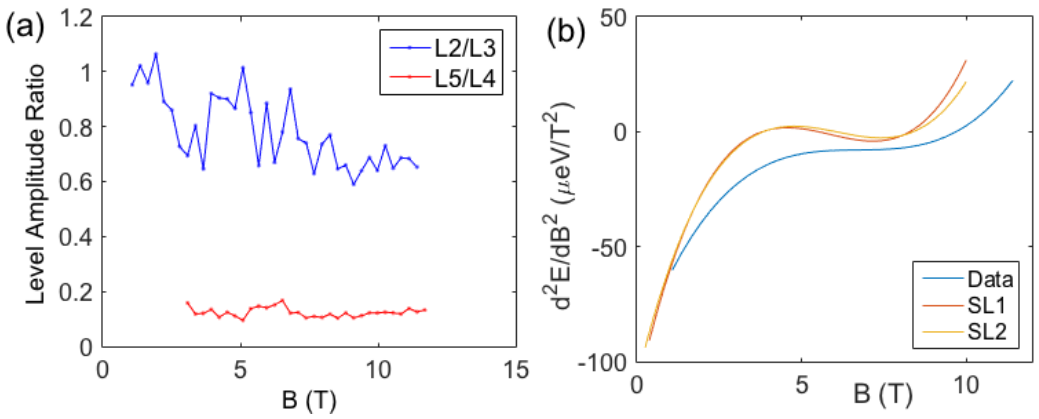

Figure 6.3: (a) Ratio of amplitudes of Zeeman split differential conductance peak branches of Ni sample 1, in the positive (blue) and negative (red) bias voltage regimes, respectively. (b) Curvature (d^2E/dB^2) of representative differential conductance levels as a function of magnetic field. Blue corresponds to Ni sample 1 data, while red and yellow correspond to the simulated differential conductance spectral levels SL1 and SL2 as shown in Fig. 4(a).

significant number of qualitative features. As the electron number on the particle alternates between N and $N+1$, the particle Hamiltonian also switches back and forth between H_N and H_{N+1}. In this work, as we have shown in previous works [51], we model H_N and H_{N+1} in the following forms,

$$H_N = -KS_z^2/S_0 - g\mu_B \vec{B}\cdot\vec{S}$$

$$H_{N+1} = H_N + \epsilon_{\mathrm{SO}}\left[\cos(\theta_{\mathrm{SO}})S_z + \sin(\theta_{\mathrm{SO}})S_x\right]^2/S_0^2$$

where K is a scalar coefficient for the uniaxial anisotropy term, g is the electron g-factor, μ_B is the Bohr magneton, $\vec{B}$ is the applied magnetic field for the Zeeman energy term, $\vec{S}$ is the vector spin operator for the particle in units of $\hbar$, and θ_{SO} and ϵ_{SO} is the magnitude of spin-orbit anisotropy energy added by a single electron during the tunneling process.

Fig. 6.4 displays high-field simulated differential conductance spectra corresponding to a Ni nanoparticle of spin $S_0 = 50$ and $\epsilon_{\mathrm{SO}} = -1$meV. The intrinsic tunneling rate through the right lead is lower than that of the left lead by a factor of 20. In

these cases, we assumed a tunneling rate of 60MHz through the left lead and 3MHz through the right lead. The difference between Fig. 6.4(a) and (b) is which lead's Fermi level is varied. In Fig. 6.4(a), μ_L is assumed fixed at a large value (1 eV), while the Fermi level in the right lead, μ_R, is swept in a triangle wave. Similarly, in Fig. 6.4(b), μ_R is held fixed at -1eV, while μ_L is varied in a triangle wave. In Fig. 6.4(b), there is clear zero field splitting of the energy level by an amount ≈ 0.6meV. However, the zero field splitting is not apparent in Fig. 6.4(a).

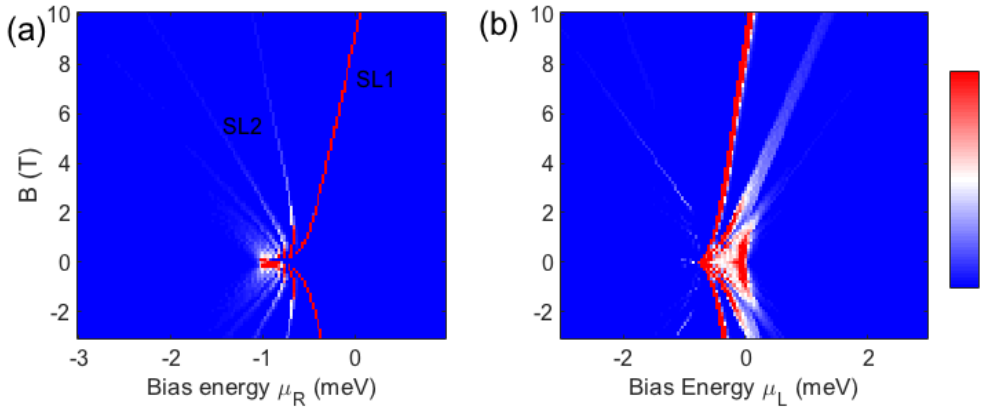

Figure 6.4: Differential conductance simulations from converged Master Equations. In each case, $\epsilon = -1$meV, $\theta_{SO} = \pi/4$, and the tunneling rates through the left (right) lead are 60MHz (3MHz), respectively. (a) The Fermi function in the left lead, $f_L = 1$, and the Fermi energy of the right lead μ_R is varied. (b) The Fermi function in the right lead, $f_R = 0$, while the Fermi energy of the left lead, μ_L, is varied.

In Fig. 6.4(a) and (b), there are Zeeman-split branches of different spectral weights, and the average curvature of the branches is proportional to the magnitude of ϵ_{SO} for each case. Additionally, the spectral weight distributions amongst levels varies as a function of field. That is, multiple levels carry higher weight in the low-field, while the spectral weight redistributes toward the energy decreasing branch in higher fields. This is reminiscent of the experimental data in Figs. 6.2(b) and 6.2(d), in which the energy levels at higher bias exhibit curvature: that is, a non-vanishing d^2E/dB^2. This is again in agreement with our simulated spectra, which display clear nonlinearities in many of the spectral branches. Note, however, that like

the experimental data, the curvatures in Fig. 6.4 can vary between branches of the same level.

6.4 Conclusions

Using tunneling spectroscopy to explore the effects of the so-interaction in nanometer-scale particles offers detailed insight into the interaction of ferromagnetism, charge transport, and quantum mechanics. We have measured Zeeman splitting in the differential conductance spectra of single Ni nanoparticles 2-3 nm in diameter under the condition of tunneling electron transport. Due to the influence of the so-interaction and its effect on the anisotropy of the particle, the tunneling rates of spin-up and spin-down electrons become comparable in magnitude, as is manifested in the relative amplitudes in each Zeeman-split spectral branch. The Ni particles we studied also exhibited spectral splitting near $B = 0$, as well as non-linear field dependence in some of the magnetic energy levels. Through master equation simulations, we studied an asymmetric resistance tunnel junction and found both zero-field splitting and curvature of the differential conductance energy levels comparable in both magnitude shape with the observed data.

CHAPTER VII

VOLTAGE-DRIVEN SPIN-TRANSFER TORQUE IN A MAGNETIC PARTICLE

In this chapter, we discuss a spin-transfer torque device, where the role of the soft ferromagnetic layer is played by a magnetic particle or a magnetic molecule, in weak tunnel contact with two spin polarized leads. We investigate if the magnetization of the particle can be manipulated electronically, in the regime where the critical current for magnetization switching is negligibly weak, which could be due to the reduced particle dimensions. Using master equation simulations to evaluate the effects of spin-orbit anisotropy energy fluctuations on spin-transfer, we obtain reliable reading and writing of the magnetization state of such magnetic particle, and find that the device relies on a critical voltage rather than a critical current. The critical voltage is governed by the spin-orbit energy shifts of discrete levels in the particle. This finding opens a possibility to significantly reduce the power dissipation involved in spin-transfer torque switching, by using very small magnetic particles or molecules.

In recent years, the miniaturization of magnets has approached the scale of single molecules [24,62,76,104,110,111,127]. While there are many measurement techniques for determining the magnetic state of such molecules, electron transport is particularly important for integrating the molecules into a microelectronic system [7]. The reduced dimensions of magnetic molecules pose both challenges and advantages. A primary challenge is due to the fact that the energy barrier for magnetic switching (E_B) is suppressed in proportion with the volume of the magnet, which weakens the

directional stability of the magnetization subject to thermal or electronic perturbations. However, the weakened barrier could also be viewed as an advantage if the external perturbations are properly controlled to manipulate magnetic switching. Consider spin-transfer torque (STT) switching in a metallic nanomagnet [20, 83, 120, 135]. The switching is usually achieved by applying a spin-polarized current through the nanomagnet, via Ohmic contacts between a ferromagnetic lead and the nanomagnet. STT-switching is normally a current-driven effect. Using the expression for current found in reference [135], it can be shown that the critical current for magnetization switching due to STT is proportional to $e\alpha E_B/\eta\hbar$, where e is the electronic charge, α is the Gilbert damping parameter, and η is the efficiency ratio dependent on both the spin polarization in the leads P and the angle between the equilibrium magnetization in the lead and the nanomagnet [135]. In larger nanomagnets, E_B is large and the resulting critical current can be associated with large power dissipation, which is a well known problem for applications. By reducing the size to the molecular scale, E_B can be significantly reduced, leading to the possibility of much lower critical current. Alternatively, a possible reduction in the critical current could be achieved with an increased spin relaxation time [41, 75, 164], which could reduce α. In this article, we consider a magnetic particle or a magnetic molecule, making weak tunneling contact between two ferromagnetic leads, and assume a vanishingly small critical current for STT switching. We address the question if the magnetization direction in such a regime can be reliably measured and manipulated, and find a voltage driven mechanism that controls STT-switching. In that regime, the spin-transfer is dominated by fluctuations of spin-orbit anisotropy energy, and predictable magnetic switching can be induced by applying a critical voltage, independent of the size of the tunneling current. By applying a voltage smaller than the critical voltage, the magnetization direction can be read noninvasively, without inducing magnetic switching.

7.1 Experimental Proposal

Recently, we have demonstrated experimentally that single Ni particles 2 to 3 nm in diameter, embedded in double-tunnel junctions, exhibit hysteresis based on the applied bias voltage [51]. A schematic of the device that we studied is shown in figure 7.1(a). At low temperature, the particle exhibits Coulomb blockade at low bias voltages, and sequential electron tunneling at higher bias voltages. The presence of hysteresis was found to be governed primarily by the voltage applied across the junction, rather than being controlled by the tunneling current. However, our prior experimental work involved the coupling of the Ni particle to normal metal (Al) leads, which lack spin-polarization. Crucial to the voltage control of magnetic hysteresis in nanomagnets is the presence of spin-orbit energy shifts ϵ_{SO} of the discrete energy levels of the particle, which vary with the direction of the magnetization [36,41]. The voltage-control results from an effective magnetization blockade [51], which arises from electron tunneling transitions with energy that increases as the particle magnetization is displaced from the easy axis. The value of the magnetization blockade energy is given by the tunneling transition energy ΔE, for which $d\Delta E/dS_z = 0$, and the magnetization is closest to the easy axis. Here, S_z is the particle spin component along the easy axis. Finding this transition energy requires diagonalization of the particle's magnetic Hamiltonians, and in a typical case, we find the magnetization blockade energy to be $\sim 0.65\epsilon_{SO}$ [51]. At low bias voltage, magnetization blockade prohibits electron tunneling transitions that would perturb the magnetization beyond a certain angle from its easy axis. At bias voltages larger than ϵ_{SO}/e (relative to the Coulomb blockade threshold), the magnetization blockade is surmounted. The result is a voltage-controlled magnetic hysteresis over a bias range on the order of ϵ_{SO}/e, governed by the shifts in spin-orbit anisotropy energy.

Figure 7.1(a) displays a generalization of such a configuration, in which we propose a non-zero spin polarization in the source and drain leads. In figure 7.1(a), the grey

region corresponds to a double-tunnel barrier, and the red circle corresponds to the single-domain magnetic particle. The straight black arrows in this figure and in subsequent figures correspond to the predominant spin polarization (in the $+z$ or $-z$ direction for $\uparrow$ or $\downarrow$, respectively). The collection of spins in the magnetic particle determine the direction of the magnetization.

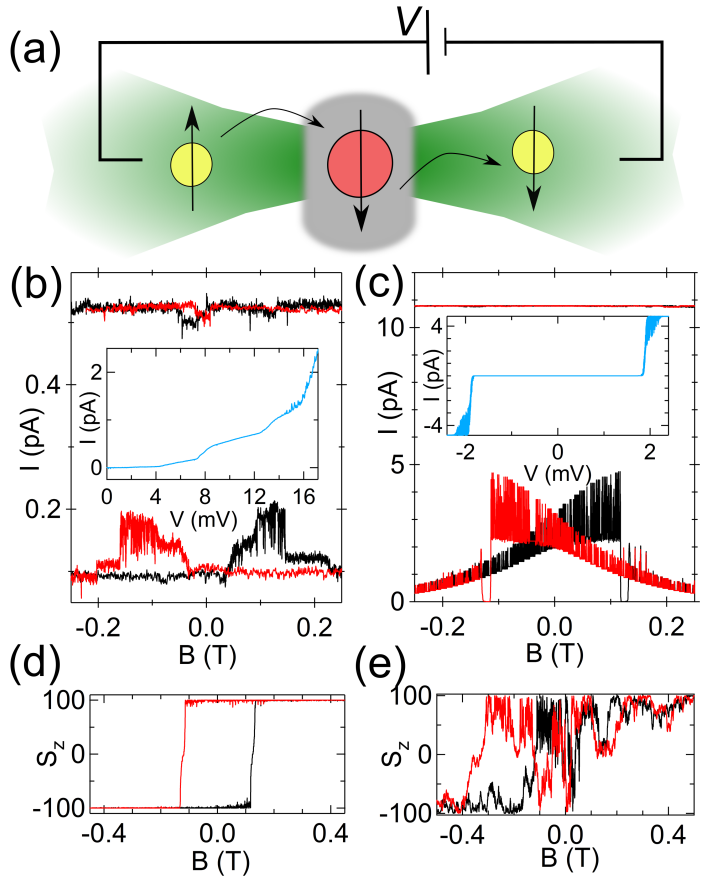

Figure 7.1: (a) Junction geometry with either no spin polarization ($P = 0$) in leads, and an applied magnetic field ($B \neq 0$), or no external magnetic field ($B = 0$), and non-zero spin polarization in leads ($P \neq 0$). Red circle corresponds to magnetic particle with net magnetization in direction of black arrow. Bias voltage V is applied on the left lead, relative to the right lead. (b) Experimental hysteresis loop data at low and high bias voltage values at $T = 350$ mK. Inset is the sample $I(V)$ curve. (c) Simulated current hysteresis loops at low ($V = 1.9$ mV) and high ($V = 2.4$ mV) bias, with inset simulated $I(V)$ curve for $P = 0$ and current onset threshold of $V_{se} = \pm 1.8$mV. Top curve is offset vertically by 6 pA for clarity. (d) Simulated hysteresis of particle magnetization, corresponding to low bias data in (c). (e) Simulated non-hysteretic switching, corresponding to high bias data in (c). For all hysteresis loops, black (red) corresponds to field sweep in positive (negative) direction.

7.2 Modeling with Master Equations and Sequential Electron Tunneling

In this work, we model the effects of single electron tunneling by use of master equations in the same procedure used in our previous work [51]. In doing so, we explore the viability of such an experimental realization as is displayed in Figure 7.1 (a). The magnetic Hamiltonian under consideration is given by the following two alternating operators. For the N electron particle, $H_0 = -KS_z^2/S_0 + 2\mu_B BS_z$, where K is a coefficient for the uniaxial anisotropy of the particle, B is the applied magnetic field, and S_z is the spin operator in the $z-$direction, μ_B is the Bohr magneton, and S_0 is the ground state spin of the particle in units of $\hbar$. For the N+1 electron particle, $H_1 = H_0 + \epsilon \left[\cos\theta_{SE} S_z + \sin\theta_{SE} S_x\right]^2 / S_0^2 + \epsilon_z S_z^2/S_0^2 + E_0$. In the latter case, we include, in addition to the N electron case, the terms ϵ and ϵ_z resulting from the spin-orbit energy shifts. θ_{SE} is the angle of the new anisotropy term arising from the additional electron, and E_0 is a constant offset term that depends on the Coulomb blockade and discrete electron-hole quasiparticle spacing. The numerical parameters are given by $K = 10\mu$eV, $S_0 = 100$, $\epsilon = 200\mu$eV, $\epsilon_z = -200\mu$eV, $\theta_{SE} = \pi/6$, $E_0 = 1$meV, and $T = 70$mK. The tunneling rates to or from a lead of polarization P for up and down spins, respectively, are given by $\Gamma(1+P)$ and $\Gamma(1-P)$, where $\Gamma = 60$ MHz, and the capacitance for each junction was 44aF. In the conversion from energy scale to voltages, a factor of 2 was included to account for the capacitive division. We neglect coupling between the magnetization and the thermal bath. In the previous experimental and computational models [51], as is shown in figure 7.1(b)-(f) a magnetic field is swept rather than using spin-polarized leads. The measured current hysteresis loops as a function of magnetic field are displayed in figure 7.1(b). The top (bottom) curves correspond to the current response at high (low) voltages relative to the magnetization blockade voltage. The dip in current prior to the zero field crossing is an artifact due to the superconducting magnet. The inset shows the tunneling current

as a function of applied bias voltage. A typical stochastic realization of he simulated current hysteresis loops at low and high bias relative to the magnetization blockade are displayed in 7.1(c), along with a simulated $I(V)$ curve in the inset. The simulated magnetization hysteresis loops that correspond to the current loops in figure 7.1(c) are displayed in figure 7.1(d) and (e), for low and high voltages, respectively, relative to ϵ_{SO}/e above the sequential electron tunneling threshold V_{se}. The experimental data and the simulations demonstrate robust magnetic hysteresis at low voltage and random magnetic switching at high bias voltage. The characteristic voltage scale that differentiates between the two regimes corresponds to the magnetization blockade energy.

Figure 7.2(a) and (b) illustrate the Coulomb blockade threshold and the magnetization blockade threshold. When the electrochemical potential of the lead is raised above the first blockade, sequential electron transport is initiated as indicated by the curved green arrows. When the electrochemical potential is increased above the magnetization blockade threshold, the spin-polarized leads initiate the particle magnetization state writing process. In (a), the particle is initially in the $M_{\downarrow}$ state. The voltage is swept linear ramp from -1.8 mV to -2.4 mV, and back to -1.8 mV, as is shown in 7.2(c). When the electrochemical potential in the left lead reaches the writing threshold, indicated by the small dotted line in (a), the magnetization of the particle flips into the $M_{\uparrow}$ state. The voltage threshold for sequential electron tunneling is $V_{se} = \pm 1.8$ mV, while the voltage required for flipping the magnetic state is approximately $V_w = \pm 2.2$ mV. Figure 7.2(d) displays the magnetization during the reverse writing process. Consider the forward writing process (that is, using a negative bias voltage to write the $M_{\uparrow}$ state). As the voltage magnitude rises between V_{se} and V_w, the magnetization (given by S_z) begins to fluctuate about its energetic minimum of $S_z = -100$. When the writing threshold potential is reached, the magnetization blockade is surmounted, and the magnetization flips as indicated by the

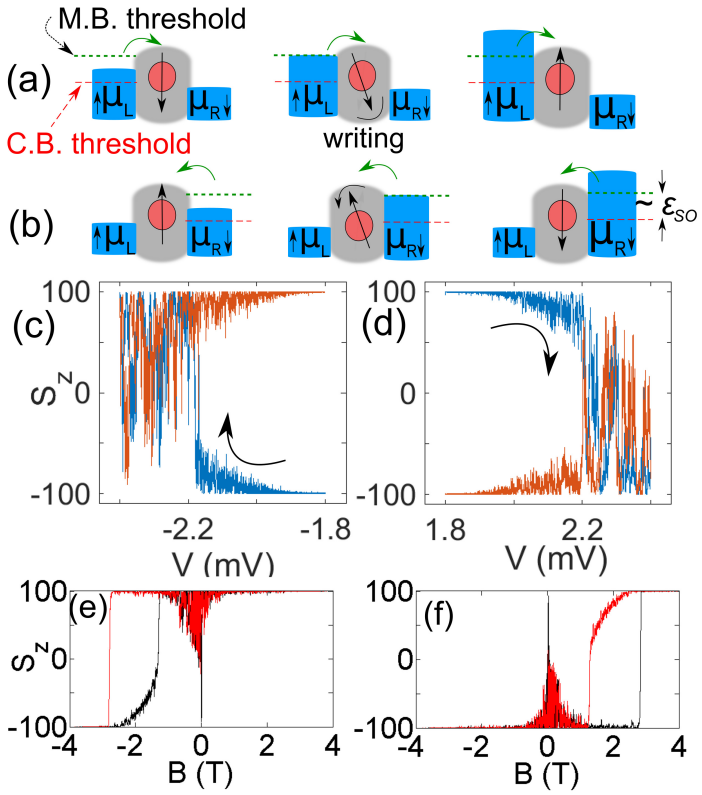

Figure 7.2: Writing the magnetic state with spin-polarized leads $P_L = 0.5, P_R = -0.5$. (a) Illustration of the electrochemical potential of the left lead (μ_L) for the forward writing process ($M_\downarrow \to M_\uparrow$), implying a negative V. Long red dashed line is the coulomb blockade threshold for sequential electron tunneling. When the writing threshold, magnetization blockade (smaller green dotted line) is reached, the particle magnetization flips directions. (b) Illustration of reverse state writing process ($M_\uparrow \to M_\downarrow$). Green arrows indicate electron tunneling direction. (c) Magnetization vs voltage during forward magnetic state writing process illustrated in (a). (d) Magnetization vs voltage for reverse magnetic state writing process as illustrated in (b). In both (c) and (d), blue (orange) correspond to magnetization during positive (negative) magnitude ramp of bias. (e) Magnetic field hysteresis loop with $P_L = 0.5$, $P_R = -0.5$ at $V = -2.2$ mV. Black (red) corresponds to field sweep in positive (negative) direction. (f) same as (e), but with $P_L = -0.5$, $P_R = 0.5$.

sudden jump of S_z around $V = -2.2$meV. Because the applied bias is still large at this point, the magnetization continues to fluctuate about its other energetic minimum state of $S_z = +100$. When the potential is reduced to its initial value, the fluctuations diminish as the magnetization relaxes into the $M_\uparrow$ state.

Similarly, the reverse writing process is displayed in figure 7.2(b) and (d), wherein a positive bias voltage greater than 2.2 mV induces a switch of the particle into the

$M_\downarrow$ state. The same result is obtained as in the forward writing process in figure 7.2(a) and (c). Thus, the sign of voltage can be used to write the binary state of the magnetic particle. In figure 7.2(e) and (f), we simulate hysteresis loops as a function of magnetic field for spin-polarized leads held at a bias voltage of -2.2 mV, the magnitude of which is above the magnetization blockade threshold of -2.16 mV. As a result, we observe an effective exchange bias due to spin accumulation on the particle. If the magnitude of the bias voltage is below the magnetization blockade threshold, the hysteresis loop appears qualitatively the same as in the $P = 0$ case, as the blockade protects the particle from switching near zero field. In figure 7.2(e), the left and right leads have spin polarization values of $P_L = 0.5$ and $P_R = -0.5$, respectively. In figure 7.2(f), $P_L = -0.5$ and $P_R = 0.5$. In both (e) and (f), the black (red) corresponds to a positive (negative) magnetic field sweep direction. In both of these sweeps, there is an increase in magnetization noise near zero field, as the particle has a small probability to flip into the opposite magnetization state. As we have observed in a previous work [74], the smaller magnetic spectrum spacing leads to the enhancement of spin-flip rate, due to the spin-orbit energy fluctuations. This is precisely the characteristic we require to allow STT switching in the proposed configuration. As the magnetic field increases, the spin-flip rate is reduced significantly when the Zeeman splitting energy approaches the spin-orbit energy shift ϵ_{SO}.

If the bias voltage is maintained well between V_{se} and V_w, the differential resistance measurements can operate as a non-invasive sensor to determine the particle magnetization state. Figure 7.3(a) and (b) illustrate the reading process for the $M_\downarrow$ and $M_\uparrow$ states, respectively. Figure 7.3(c) displays the differential resistance (dV/dI) ratios, averaged over time, for the $M_\downarrow$:$M_\uparrow$ states. As a function of bias, the ratio of differential conductance varies as much as 40% for the different magnetization states. This results from the asymmetry in the tunneling resistance near the Coulomb blockade as a function of spin polarization mismatch. As long as the electrochemical potential

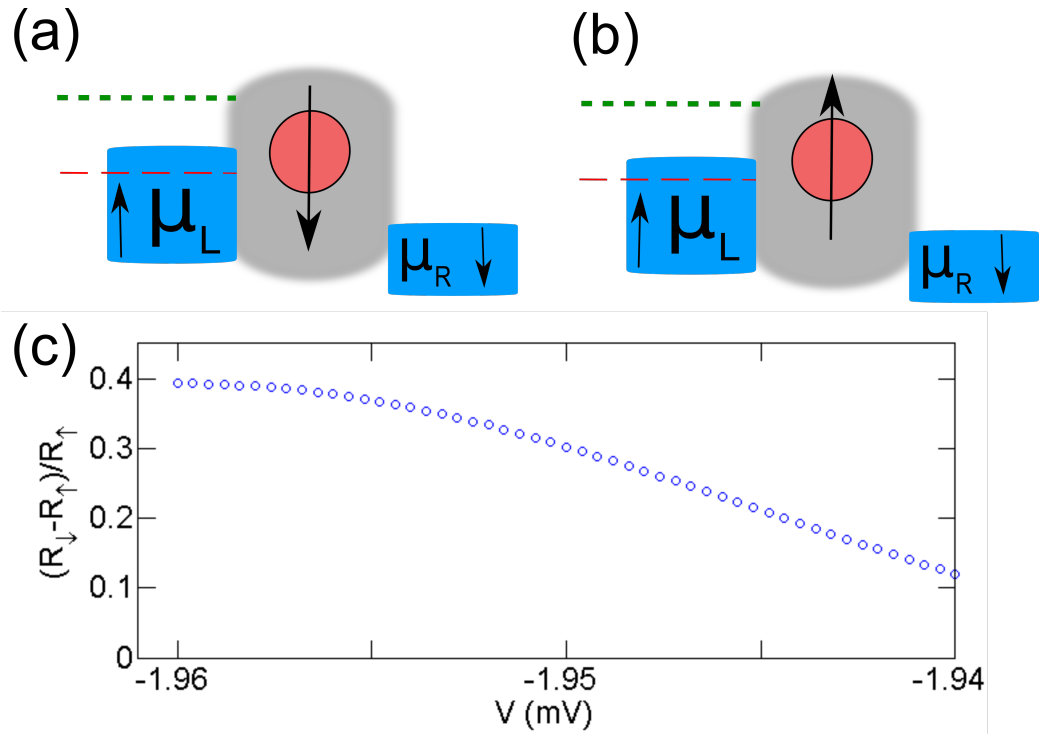

Figure 7.3: Reading the magnetic state. (a) Sensing the $M_\downarrow$ state. (b) Sensing the $M_\uparrow$ state. (c) Ratio of the differential resistance measurements for $M_\downarrow : M_\uparrow$. Electrochemical potential is always maintained well below the writing threshold, indicated by the small dotted green line in (a) and (b).

in the spin-polarized leads is maintained well below the writing threshold, the particle magnetization will only fluctuate weakly about its current energetic minimum orientation, allowing for the reproducible sensing of the magnetic state.

At high voltages compared with $V_{se} + \epsilon_{SO}/e$ during the particle writing process, there is a certain probability that the particle will switch back to its initial state before relaxing. Figure 7.4 displays the histograms of the particle spin states, as a function of spin polarization in the leads and particle size. In each of these cases, the bias was held at $V = -2.4$meV, which is above the magnetization blockade voltage, and would correspond to the forward state writing process as shown in figure 7.2(c). For each configuration, we estimate the reliability r of successfully writing the state $M_\uparrow$ by taking the ratio of the sum of states with $S_z > 0$ to the total sum of states. We chose such a definition because in the actual state writing process, we would reduce

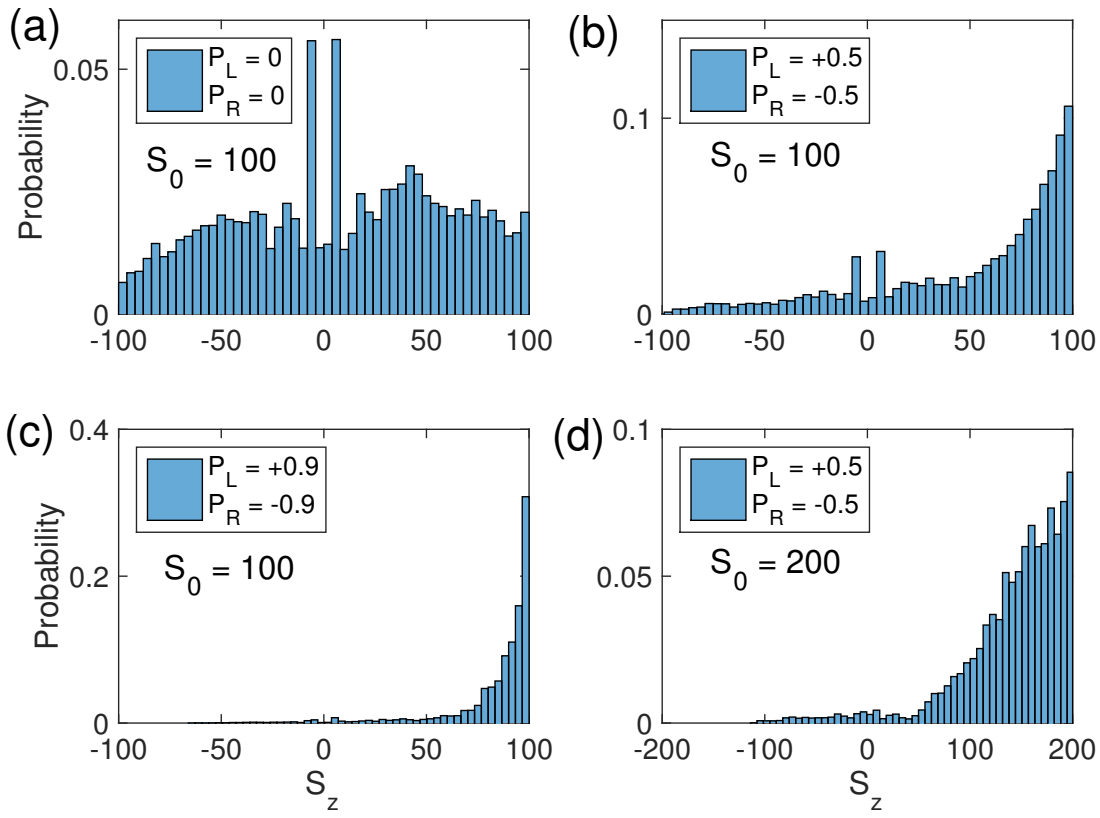

Figure 7.4: Particle state histograms as a function of spin polarization in leads and particle size, at high bias voltages relative to ϵ_{SO}/e. (a) Normal leads with no spin polarization. (b) Spin polarization of ± 0.5 in left and right leads, respectively. (c) Spin polarization of ± 0.9 in left and right leads, respectively. $S_0 = 100$ in (a),(b), and (c). (d) Spin polarization of ± 0.5 in left and right leads, respectively, with larger particle size of $S_0 = 200$.

the magnitude of the bias voltage, and the particle would relax into whichever local minimum had the same sign ($S_z = \pm S_0$, based on the final sign of S_z before lowering the voltage). For figure 7.4(a), the state histogram is evaluated for non-spin-polarized leads, as in the case for our previous experimental work [51]. Not surprisingly, the non-polarized leads are ill-equipped to produce dependable switching of the particle state to $M_\uparrow$. However, as is shown in figure 7.4(b) and (c), the reliability of switching the particle becomes 83% (98%), with respective increases in spin polarization in the leads $P_L = 0.5$ and $P_R = -0.5$ ($P_L = 0.9$ and $P_R = -0.9$). A similar effect can be achieved by altering the size of the particle. For spin polarization in the leads

of $P_L = 0.5$ and $P_R = -0.5$, the reliability of switching a particle of spin $S_0 = 50$ ($S_0 = 200$) is found to be 78% (97%). The state histogram for the latter case of $S_0 = 200$ is displayed in figure 7.4(d). In the case of $P_L = 0.25$ and $P_R = -0.25$ for $S_0 = 100$, we found a reliability of 75%. However, we can increase the effective reliability by use of the following procedure. First, we apply a voltage pulse of the desired sign to attempt writing a magnetic state. Then, we can apply a smaller bias voltage to read out the state. If the initial pulse has successfully written a state, then halt the procedure. If not, apply a second voltage pulse and check the success of the second attempted writing procedure. Assuming independent writing events, each dictated by a reliability r, with $0 \leq r \leq 1$, the overall reliability of the repeated writing procedure will be $1 - (1 - r)^n$, where n is the number of attempted writing events. If at any point between the writing attempts a successful state readout is achieved, then the procedure is stopped. Using such a scheme with $r = 0.75$ and a maximum of 4 writing attempts, the new reliability of writing the desired state is raised above 99%.

7.3 Conclusions

In summary, we have presented a proposal for a generalized STT system in which the soft magnetic layer is composed of a magnetic molecule or a magnetic particle which exhibits an effective magnetization blockade due to spin-orbit shifts of discrete levels. Rather than relying on a critical current to induce magnetic switching, magnetic control in our proposed configuration is instead governed by the applied bias voltage from spin-polarized leads. Our simulations indicate that the proposed configuration is well suited for writing magnetic states with high repeatability, and for reading states in a non-invasive manner. This opens the possibility for a significant reduction in power dissipation in reduced scale STT devices.

CHAPTER VIII

CONCLUSIONS AND FUTURE WORK

In summary, I have presented a dissertation on the effects of the spin-orbit interaction on sequential electron tunneling in ferromagnetic nanoparticles at the confluence of quantum mechanics and nanometer-scale magnetism. By studying metallic samples on the order of 2 nm in diameter using a probe of a single electron at a time, and at temperatures slightly above absolute zero, I was able to study the interaction of different energy scales and observe novel effects due to the spin-orbit interaction. In particular, I observed large electron spin g-factors in Co particles as a result of the interplay between spin-orbit effects and ferromagnetic electron-electron interactions. Further, I studied the detailed differential conductance spectra of Co and Ni samples, and found differing characteristics among different materials. Next, I observed a voltage-controllable hysteresis effect in single Ni nanoparticles, and modeled such effects using master equation simulations. In doing so, I defined an effective magnetization blockade due to the anisotropy energy shifts, and further proposed a voltage-controlled spin-transfer torque device based on the same physical effect.

The magnetization blockade effect opens the the door for further study, including an experimental implementation of the device proposed in the last chapter. Such a project would be challenging, but also rewarding in the possibility of designing a device that will push the limits of spin-transfer torque.

APPENDIX A

DETAILED CODE OVERVIEW

In this appendix, we will discuss in detail the code utilized in this dissertation, and will be broken into two primary sections. First, I will give an overview of the subroutines that are called by the main two types of master equation simulation implementations. Next, I will discuss the full master equation simulations, which describe the temporal evolution of the full probability distribution over the particle eigenstates. Finally, I will describe the stochastic master equation simulations, which use a similar probability evolution equation as the full master equation mentioned previously, but assume that at each time step, the sample is in one of its eigenstates. The transition probabilities are calculated via integrating the master equation above for one time step in order to calculate the likelihood of transition among the different eigenstates. In all of the code below, I have attempted to comment the code as extensively as possible to elucidate the details. All simulations were performed using MATLAB. An initial form of the basic code for the full master equation simulation was written by my former colleague, Wenchao Jiang. I have edited his code and tried to optimize portions that were running slowly. As an example, I vectorized most of the nested loops in order to make use of MATLAB's matrix multiplication strengths. I also wrote the new code for the stochastic evolution simulations, and the plotting procedures.

A.0.1 Subroutines Common to both Implementations of Master Equations

Necessary for each implementation of the primary programs are various subroutines, such as the calculation of the particle spin operators and Hamiltonian operators, sorting the eigenstates, and accounting for the Clebsch-Gordan coefficients. In this

section, I will provide and describe the code of such subroutines that are necessary for both the deterministic master equation evolution and for the stochastic eigenstate evolution simulations.

A.0.1.1 Defining the Hamiltonian Parameters

The code in this section should be tacked on to the beginning of any simulation, in order to define the basic parameters for the N and $N+1$ particle Hamiltonian operators, including the definition of the spin operators. The name of this script is definehamilcellparam.m, and this should be edited to use the desired parameters for the Hamiltonians. Note that this program makes use of the findspinoperators function, which is included as the next program.

```
%definehamilcellparam.m

%%%%%%%%%%%%%%%%%%%%%%%%%%%%%%%%%%%%%%%%%%%%%%%%%%%%%%%%%%%%%%%%%%%%%%%%%%%%%%%
% Set Hamiltonian parameters here
%
%%%%%%%%%%%%%%%%%%%%%%%%%%%%%%%%%%%%%%%%%%%%%%%%%%%%%%%%%%%%%%%%%%%%%%%%%%%%%%%

S0 = 100; %defines the ground state spin of the N-electron particle
S01 = S0-1/2; %defines the ground state spin of the N+1 electron particle
% assumes only minority electrons contribute to tunneling. That is, the
% total spin of the particle is reduced by 1/2 upon the addition of a
% tunneling electron.

%All of the energies are in units of micro-eV.
epsilon = 200; %energy for extra anisotropy due to spin-orbit energy ...
%shifts from one electron.

epsilonz = -200; %energy for second extra anisotropy term.
```

```
18
19 Kbiax = 0; % energy for biaxial anisotropy term
20
21 Kzunianis = 10; %energy coefficient for uniaxial anisotropy term
22
23 theta_se = pi/6; %defines angle of added anisotropy relative to z-axis
24
25 countt=1; %index used for keeping track of the simulation progress ...
26 %to gauge how much time remains.
27
28 ktemp = 86*0.075; % to change the temperature in the leads, change ...
29 %the number that is multiplying 86. As it stands, this represents 75 mK, ...
30 %and 86 is Boltzmann's constant in units of micro-eV/Kelvin.
31
32 kappa=0;%-0.0001% term used to break degeneracy of zero magnetic field case
33
34 h = 0; %initialize the applied magnetic field to zero. this can be altered ...
35 %by making a vector of hvals for the magnetic field values at each time step.
36 Kzunianis = 10; %uniaxial anisotropy coefficient
37
38 [Sx,Sy,Sz,Sx1,Sy1,Sz1] = findspinoperators(S0,S01);
39
40 hamilcellparam = {S0,S01,epsilon,epsilonz,theta_se,kappa,h,Sx,Sy,Sz, ...
41     Sx1,Sy1,Sz1,Kzunianis,Kbiax};
```

The following function takes S0 and S01 as inputs, and outputs the spin operators for the N and N+1 electron particles.

```
1
2 function [Sx,Sy,Sz,Sx1,Sy1,Sz1] = findspinoperators(S0,S01)
3
4 %FINDSPINOPERATORS calculates N and (N+1) electron particle spin operators
```

```
%Sx, Sy, Sz, and (Sx1, Sy1, Sz1), respectively, given total spin values S0
%and S01 for the N and N+1 electron particles
%Sx is for the spin of |S0 m> state
Sx=zeros(2*S0+1,2*S0+1);
Sz=zeros(2*S0+1,2*S0+1);
Sy=zeros(2*S0+1,2*S0+1);

%Sx1 is for the spin of |S0-1/2 m> state
Sx1=zeros(2*S0,2*S0);
Sz1=zeros(2*S0,2*S0);
Sy1=zeros(2*S0,2*S0);

%Calculate Sx, Sy, Sz operators for N electron particle
for k=-1*S0:1:S0
    for j=-1*S0:1:S0
        if j==k-1
            Sx(k+S0+1,j+S0+1)=1/2*(sqrt((S0-j)*(S0+j+1)));
            Sy(k+S0+1,j+S0+1)=-1i/2*(sqrt((S0-j)*(S0+j+1)));
        elseif j==k
            Sz(k+S0+1,j+S0+1)=k;
            Sx(k+S0+1,j+S0+1)=0;
        elseif  j==k+1
            Sx(k+S0+1,j+S0+1)=1/2*(sqrt((S0+j)*(S0-j+1)));
            Sy(k+S0+1,j+S0+1)=1i/2*(sqrt((S0+j)*(S0-j+1)));
        else Sx(k+S0+1,j+S0+1)=0;
        end
    end
end

%Calculate Sx1, Sy1, Sz1 for N+1 electron particle
for k=-(S01):1:(S01)
    for j=-(S01):1:(S01)
```

```
        if j==k-1
            Sx1(k+S01+1,j+S01+1)=1/2*(sqrt((S01-j)*(S01+j+1)));
            Sy1(k+S01+1,j+S01+1)=-1i/2*(sqrt((S01-j)*(S01+j+1)));
        elseif j==k
            Sz1(k+S01+1,j+S01+1)=k;
            Sx1(k+S01+1,j+S01+1)=0;
        elseif  j==k+1
            Sx1(k+S01+1,j+S01+1)=1/2*(sqrt((S01+j)*(S01-j+1)));
            Sy1(k+S01+1,j+S01+1)=1i/2*(sqrt((S01+j)*(S01-j+1)));
        else Sx1(k+S01+1,j+S01+1)=0;
        end
    end
end

end
```

The next section of code defines the Hamiltonian operators for the N and N+1 electron particle. It requires an input cell of hamilcellparam, which can be generated using the definehamilcellparam.m script above. It returns the eigenstates V (V1) and eigenenergies D (D1) for the N (N+1) electron particle. These are combined into a cell, hamiloutcell, for input into the sortandCG program below.

```
format('long')
% define a cell of parameters for input into the findhamilstates program:
hamilcellparam = {S0,S01,epsilon,epsilonz,theta_se,kappa,h,Sx,Sy,Sz, ...
Sx1,Sy1,Sz1,Kzunianis,Kbiax};
%%%%%%%%%%%%%%%%%%%%%%%%%%%%%%%%%%%%%%%%%%%%
function [V,D,V1,D1] = findhamilstates(hamilcellparam)
%FINDHAMILSTATES yields the eigenstates V (V1) and eigenvalues D (D1) for
%the N (N+1) electron Hamiltonians.
%hamilcellparam should be a cell of the following form:
```

```
10 %hamilcellparam = {S0,S01,epsilon,epsilonz,theta_se,kappa,h,Sx,Sy,Sz, ...
11 % Sx1,Sy1,Sz1,Kzunianis,Kbiax};
12 %%%%%%%%%%%%%%%%%%%%%%%%%%%%%%%%%%%%%%%%%%%%
13 % The name of the following subroutine is Costates4_nos.m
14
15 format('long')
16 % export hamiltonian parameters from hamilcellparam cell:
17 S0 =       hamilcellparam{1};
18 S01 =      hamilcellparam{2};
19 epsilon =  hamilcellparam{3};
20 epsilonz = hamilcellparam{4};
21 theta_se = hamilcellparam{5};
22 kappa =    hamilcellparam{6};
23 h =        hamilcellparam{7};
24 Sx =       hamilcellparam{8};
25 Sy =       hamilcellparam{9};
26 Sz =       hamilcellparam{10};
27 Sx1 =      hamilcellparam{11};
28 Sy1 =      hamilcellparam{12};
29 Sz1 =      hamilcellparam{13};
30 Kzunianis= hamilcellparam{14};
31 Kbiax = hamilcellparam{15};
32
33 %Magnetic Field direction
34 %define angles in spherical coordinates relative to z-axis (easy axis)
35 theta1=0;%3*pi/12;
36 phi1=0;%
37 b=[sin(theta1)*cos(phi1) sin(theta1)*sin(phi1) cos(theta1)];
38
39
40 %Spin-orbit anisotropy energy term from a single electron
41 soanisotropy = 0;
```

```
soanisotropy1 = epsilon*((Sz1*cos(theta_se)+Sx1*sin(theta_se)))^2/S01^2 ...
+ epsilonz*Sz1^2/S01^2;


%Shape Anisotropy Energy term (uniaxial in this case). kappa term breaks
%degeneracy in zero magnetic field case.
%Kbix is the coefficient for the biaxial anisotropy term.
shapeanisotropy =  -Kzunianis*Sz^2/S0 + kappa*Sx^2/S0 ...
    - Kbiax*(Sz^2-Sx^2)/S0;
shapeanisotropy1 =  -Kzunianis*Sz1^2/S01 + kappa*Sx1^2/S01 ...
    - Kbiax*(Sz1^2-Sx1^2)/S01;

%Zeeman Energy term (bohr magneton is 57.89 micro-eV/Tesla
zeemanenergy = -(2*h*57.89*(b(1)*Sx+b(2)*Sy+b(3)*Sz));
zeemanenergy1 = -(2*h*57.89*(b(1)*Sx1+b(2)*Sy1+b(3)*Sz1));

%Calculate for the eigenstates and eigenenergies
H=zeemanenergy+soanisotropy+shapeanisotropy;
H1=zeemanenergy1+soanisotropy1+shapeanisotropy1;

[V,D] = eig(H);    %eigenstates/eigenvalues of N-electron Hamiltonian
[V1,D1] = eig(H1); %eigenstates/eigenvalues of (N+1)-electron Hamiltonian


end

hamiloutcell = {V,D,V1,D1};
```

A.0.1.2 Sorting the Particle Eigenstates

This section of code immediately follows the previous subroutine, each time the previous code is run. It calculates the expectation value of each spin component operator (S_x, S_y, and S_z, along with S_x^2, S_y^2, and S_z^2) for every pair of eigenstates for the N

and $N+1$ electron Hamiltonian. It sorts the eigenstates in order of increasing S_z expectation value, and then stores the eigenenergies of these sorted states in the vectors Ens and Ens1 for the N and $N+1$ electron particles, respectively. Then, the code calculates the Clebsch-Gordan coefficients and the state overlap matrices.

```
function [TN2,TP2,T,SZS,SZS1,Ens,Ens1] = sortandCG(hamiloutcell,hamilcellparam)
%SORTANDCG -- sorts eigenstates and calculates clebsch gordan coefficents
%and state overlaps for use in master equation simulations.
%   Takes two cells as inputs. The first, hamiloutcell, consists of a cell
%   of {V,D,V1,D1}, which is the output from the findhamilstates function.
%   The second cell input, hamilcellparam, is the same cell input of
%   parameters into the initial findhamilstates function, and is of the
%   form
%   {S0,S01,epsilon,epsilonz,theta_se,kappa,h,Sx,Sy,Sz,Sx1,Sy1,Sz1, ...
% Kzunianis}

format('long')
%export hamiloutcell parameters (eigenstates and eigenenergies):
V = hamiloutcell{1};
D = hamiloutcell{2};
V1= hamiloutcell{3};
D1= hamiloutcell{4};

% export hamiltonian parameters from hamilcellparam cell:
S0 =       hamilcellparam{1};
S01 =      hamilcellparam{2};
epsilon =  hamilcellparam{3};
epsilonz = hamilcellparam{4};
theta_se = hamilcellparam{5};
kappa =    hamilcellparam{6};
h =        hamilcellparam{7};
```

```
Sx =        hamilcellparam{8};
Sy =        hamilcellparam{9};
Sz =        hamilcellparam{10};
Sx1 =       hamilcellparam{11};
Sy1 =       hamilcellparam{12};
Sz1 =       hamilcellparam{13};
Kzunianis= hamilcellparam{14};
Kbiax= hamilcellparam{15};

%Sort eigenstates below: (formerly the indexeadd.m script)


SpinZ1=real(V1'*(Sz1)*V1);
SpinZ=real(V'*(Sz)*V);
SpinX1=real(V1'*(Sx1)*V1);
SpinX=real(V'*(Sx)*V);
SpinY1=real(V1'*(Sy1)*V1);
SpinY=real(V'*(Sy)*V);

SpinZ2=real(V'*(Sz*Sz)*V);
SpinX2=real(V'*(Sx*Sx)*V);
SpinY2=real(V'*(Sy*Sy)*V);

SZE=zeros(1,2*S0+1);
SZE1=zeros(1,2*S01+1);

for i=1:2*S0+1
    SZE(i)=real(SpinZ(i,i));
end
for i=1:2*S01+1
    SZE1(i)=SpinZ1(i,i);
end
```

```
59 [SZS,IX]=sort(SZE);
60 [SZS1,IX1]=sort(SZE1);
61
62 SZS=SZS';
63 SZS1=SZS1';
64
65 Ens=zeros(1+2*S0,1);
66 Ens1=zeros(1+2*S01,1);
67 SXS=Ens;
68 SYS=Ens;
69 SXS2=Ens;
70 SYS2=Ens;
71 SZS2=Ens;
72 for i=1:2*S0+1
73    Ens(i)=real(D(IX(i),IX(i)));
74    SXS(i)=SpinX(IX(i),IX(i));
75    SYS(i)=SpinY(IX(i),IX(i));
76    SXS2(i)=SpinX2(IX(i),IX(i));
77    SYS2(i)=SpinY2(IX(i),IX(i));
78    SZS2(i)=SpinZ2(IX(i),IX(i));
79 end
80 SXS1=Ens1;
81 SYS1=Ens1;
82 for i=1:2*S01+1
83    SXS1(i)=SpinX1(IX1(i),IX1(i));
84    SYS1(i)=SpinY1(IX1(i),IX1(i));
85    Ens1(i)=real(D1(IX1(i),IX1(i)));
86 end
87
88
89 %%%%%%%%%%%%%%%%%%%%%%%%%%%%%%%%%%%%%%%%%%%%
90 %The following bit of code finds the clebsch gordan coefficients and
```

```
91 %overlap matrices. (formerly the CGpra_vectorized_pg.m script)
92
93 %Clebsch-Gordon (CG) Coefficients
94 % This will calculate the CG coefficients for expressing a composite spin
95 % system's eigenstates |S01,m> in terms of the eigenstates of the separate
96 % representation |1/2,1/2>|S0,m-1/2> and |1/2,-1/2>|S0,m+1/2>, such that
97 % the transformation of one basis to another follows the identity:
98 %  |S01,m> = pCGP*|1/2,1/2>|S0,m-1/2> + pCGN*|1/2,-1/2>|S0,m+1/2>, where
99 %  S01 = S0-1/2.
100
101
102 %initialize vectors of CG coefficients:
103 pCGP = zeros(2*S01+1,1);
104 pCGN = zeros(2*S01+1,1);
105
106 for m=-S01:1:S01
107     pCGP(m+S01+1) = sqrt( (S0-m+1/2)/(2*S0+1) );
108     pCGN(m+S01+1) = -sqrt( (S0+m+1/2)/(2*S0+1) );
109 end
110
111 CGP = pCGP;
112 CGN = pCGN;
113
114 Vs=V;
115 Vs1=V1;
116 for i=1:1+2*S0
117     Vs(:,i)=V(:,IX(i));
118 end
119 for i=1:1+2*S01
120     Vs1(:,i)=conj(V1(:,IX1(i)));
121 end
122 %The following two lines put the CG coefficients in a matrix in order ...
```

```
123 %to allow for vectorization of code for speed.
124 CGNmat = repmat(CGN,[1,2*S01+1]);
125 CGPmat = repmat(CGP,[1,2*S01+1]);
126
127 %The following two lines are a vectorized implementation of sums ...
128 %in order to optimize speed.
129 TN=conj((conj(Vs(2:2*S01+2,:)')*(Vs1.*CGNmat))');
130 TP=conj((conj(Vs(1:2*S01+1,:)')*(Vs1.*CGPmat))');
131
132 TP2=TP.*conj(TP);
133 TN2=TN.*conj(TN);
134 T=TP2+TN2; % T(i,j)=|<i|C|j>|^2+|<i|C+|j>|^2
135
136 end
```

A.0.2 Plotting the Tunneling Density of States

The next program will calculate the Tunneling Density of States (DOS), for a given set of Hamiltonian parameters defined in definehamilcellparam.m script. Requires the findhamilstates and sortandCG sub-routines. The program outputs the DOS as a matrix, dosmat, and automatically plots the result.

```
1 function [dosmat] = plotsingleDOS(eners,sigma)
2 % PLOTSINGLEDOS --calculates the tunneling density of states for the nth
3 % state on the N-electron particle tunneling into the sum over the m'
4 % states of the (N+1)-electron particle. inputs eners is the
5 % vector of energy values at which the DOS is evaluated, and sigma is the
6 % amount by which the delta function is spread by convolving with a
7 % gaussian of standard deviation sigma. Assumes that the
8 % definehamilcellparam script has been appropriately edited with the
9 % desired parameters before running this program.
10
```

```
11 if nargin==0
12     %arbitrarily set eners and sigma if no inputs are given
13     eners = -150:1:150;
14     sigma = 1;
15 end
16 format('long')
17 tic
18
19 definehamilcellparam;
20 [V,D,V1,D1] = findhamilstates(hamilcellparam);
21 hamiloutcell = {V,D,V1,D1};
22 [TN2,TP2,T,SZS,SZS1,Ens,Ens1] = sortandCG(hamiloutcell,hamilcellparam);
23
24 % define a local function 'gaussian' with which to convolve the delta
25 % function energy term:
26 gaussian = @(x) 1./(sigma*sqrt(2*pi))*exp(-x.^2/(2*sigma^2));
27
28
29 dosmat = zeros(2*S0+1,length(eners));
30
31 for inds = 1:2*S0+1
32
33     for inde = 1:length(eners)
34         energy = eners(inde);
35         psum = 0;
36         for indm = 1:2*S0
37             en = Ens(inds);
38             em = Ens1(indm);
39
40             psum = psum + T(indm,inds)*gaussian(energy-em+en);
41
42
```

```
        end
        dosmat(inds,inde) = psum;

    end
end
toc

figure; imagesc(-S0:S0,eners/1000,dosmat');
set(gca,'fontname','arial','fontsize',18)
xlabel('S_z');
ylabel('Energy (meV)');
title(['DOS, h=' num2str(h) 'T, \epsilon = ' num2str(epsilon/1000) ...
    'meV, \epsilon_z=' num2str(epsilonz/1000) 'meV, \theta_S_0 = ' ...
    num2str(theta_se/pi) '\pi.']);
axis xy


end
```

A.0.3 Checking Convergence of Master Equation

The next short program checks to see if the Sz projection, as compared with the former Sz projection 100 time steps previous, has converged to a value within a tolerance of tol=0.1. These (arbitrary) choices can be altered within the simplemaster program below, if desired.

```
function [torf] = checkconvergence(a,b,tol)
%checks to see if b has converged to a within tolerance tol
if abs(b-a)<tol
    torf = true;
else
    torf = false;
```

```
7
8 end
```

A.0.4 Master Equation Code

Now that I have described the preliminary subroutines used in both the deterministic master equation code and the stochastic implementation, I will now describe the deterministic master equation code itself. The name of the program is simplemaster, and must be run for each set of looped parameters, such as the electrochemical potential in the left and right leads (uL and uR, respectively), the thermal energy in the leads (ktemp), the bare tunneling rates in the left and right leads (RL and RR, respectively), the spin polarization in the left and right leads (PSL and PSR, respectively), the total integration time for the master equation (t) and the time step (dt). Further, the program requires an input cell called sortCGoutcell, which is derived from the output of the program sortandCG, which should be run prior to every implementation of simplemaster, if Hamiltonian parameters have changed. During each call to simplemaster, the program checks for convergence of the Sz projection in order to speed up the program. The program outputs the spin projection m as a function of integration time, and the final converged probability distribution for the N and N+1 electron particle (pend and qend, respectively).

```
1 function [m,pend,qend] = simplemaster(sortCGoutcell,loopparamscell)
2 %SIMPLEMASTER -- Integrates the deterministic master equation for a given
3 %set of input parameters, and checks for convergence of Sz projection
4 %within the program -- halts program in order to speed up process if Sz has
5 %converged to its value 100 time steps ago within tolerance tol. Calls
6 %checkconvergence subroutine.
7
8 %export values from the output from sortandCG program:
```

```
9  TN2  = sortCGoutcell{1};
10 TP2  = sortCGoutcell{2};
11 T    = sortCGoutcell{3};
12 SZS  = sortCGoutcell{4};
13 SZS1 = sortCGoutcell{5};
14 Ens  = sortCGoutcell{6};
15 Ens1 = sortCGoutcell{7};
16 S0 = (length(Ens)-1)/2;
17 S01 = (length(Ens1)-1)/2;
18
19 %export values from the current loop parameters:
20 uL    = loopparamscell{1};
21 uR    = loopparamscell{2};
22 ktemp = loopparamscell{3};
23 RL    = loopparamscell{4};
24 RR    = loopparamscell{5};
25 PSL   = loopparamscell{6};
26 PSR   = loopparamscell{7};
27 t     = loopparamscell{8};
28 dt    = loopparamscell{9};
29 pinit = loopparamscell{10};
30 qinit = loopparamscell{11};
31
32 Tt=T(1:(2*S01+1),1:(2*S0+1));
33
34
35
36 dP=zeros(1,2*S0+1);
37 dQ=zeros(1,2*S01+1);
38
39
40 P=zeros(length(t),2*S0+1);
```

```
41 Q=zeros(length(t),2*S01+1);
42
43 % if pinit==0 && qinit==0
44 %     P(1,1)=1;
45 %     %initflag=false;
46 % else
47 P(1,:) = pinit;
48 Q(1,:) = qinit;
49
50 % if initflag==true
51 %     P(1,1)=1;
52 %     initflag=false;
53 % else
54 %     P(1,:) = pinit;
55 %     Q(1,:) = qinit;
56 % end
57
58 Ensmat = repmat(Ens',[2*S01+1,1]);
59 Ens1mat = repmat(Ens1,[1,2*S0+1]);
60
61 fL = 1./(1+exp((Ens1mat-Ensmat-uL)./ktemp));
62 fR = 1./(1+exp((Ens1mat-Ensmat-uR)./ktemp));
63
64
65 Ttu=TP2(1:2*S01+1,1:2*S0+1);
66 Ttd=TN2(1:2*S01+1,1:2*S0+1);
67
68 %spin dependent tunneling rates below:
69 RLu = (1+PSL)*RL;
70 RLd = (1-PSL)*RL;
71 RRu = (1+PSR)*RR;
72 RRd = (1-PSR)*RR;
```

```
73
74 TfLu = RLu*times(Ttu,fL);
75 %matrix element for tunneling on to particle from left lead, spin up
76
77 TfLd = RLd*times(Ttd,fL);
78 %matrix element for tunneling on to particle from left lead, spin down
79
80 TfLua = RLu*times(Ttu,1-fL);
81 %matrix element for tunneling off of particle into left lead, spin up
82
83 TfLda = RLd*times(Ttd,1-fL);
84 %matrix element for tunneling off of particle into left lead, spin down
85
86 TfRu = RRu*times(Ttu,fR);
87 %matrix element for tunneling on to particle from right lead, spin up
88
89 TfRd = RRd*times(Ttd,fR);
90 %matrix element for tunneling on to particle from right lead, spin down
91
92 TfRua = RRu*times(Ttu, 1-fR);
93 %matrix element for tunneling off of particle into right lead, spin up
94
95 TfRda = RRd*times(Ttd, 1-fR);
96 %matrix element for tunneling off of particle into right lead, spin down
97
98 Tfu = TfLu + TfRu;
99 % total matrix element of spin up electron tunneling onto particle from ...
100 % both leads
101
102 Tfd = TfLd + TfRd;
103 % total matrix element of spin down electron tunneling onto particle ...
104 % from both leads
```

```
105
106 Tf = Tfu + Tfd;
107 % total matrix element of both spin polarizations tunneling onto ...
108 % particle from leads
109
110 Tfua = TfLua + TfRua;
111 Tfda = TfLda + TfRda;
112 Tfa = Tfua + Tfda;
113 Tfp = Tfu + Tfd;
114 Tfaq = Tfua + Tfda;
115
116 for s=2:length(t)
117
118
119     qvecnow = (Q(s-1,:))';
120     qmatnow = repmat(qvecnow,[1,2*S0+1]);
121     Tfaq = dt*times(qmatnow,Tfa);
122
123     pvecnow = P(s-1,:);
124     pmatnow = repmat(pvecnow,[2*S01+1,1]);
125     Tfp = dt*times(pmatnow,Tf);
126
127
128
129     Tdiff=Tfaq-Tfp;
130
131     Tdiffp=-1*Tdiff';
132
133     dP=sum(Tdiff);
134     dQ=sum(Tdiffp);
135     dP=double(dP);
136     dQ=double(dQ);
```

```
137     P(s,:)=P(s-1,:)+dP;
138     Q(s,:)=Q(s-1,:)+dQ;
139
140     %Every 200 time steps, this conditional loop checks to see if the
141     %spin projection m has converged to within a tolerance value (the
142     %default tolerance is 0.1 in units of hbar), as compared with the value
143     %of m at 100 time steps prior to the current value. If convergence has
144     %occurred, the remaining probability distribution values for P and Q
145     %are set to the most recent values.
146     if mod(s,200)==0
147         mnow = P(s,:)*SZS + Q(s,:)*SZS1;
148         mold = P(s-100,:)*SZS + Q(s-100,:)*SZS1;
149         if checkconvergence(mnow,mold,0.1)
150             P((s+1):length(t),:) = repmat(P(s,:),[(length(t)-(s+1)+1),1]);
151             Q((s+1):length(t),:) = repmat(Q(s,:),[(length(t)-(s+1)+1),1]);
152
153             break
154         end
155
156     end
157 end
158
159 Eem=P*(Ens(1:(2*S0+1))-Ens(1))+Q*(Ens1(1:(2*S01+1))-Ens1(1));
160 %magnetic energy relative to smallest Sz state energy
161 m=P*(SZS)+Q*(SZS1);
162 %expected spin projection onto z-axis
163 pend = P(end,:);
164 qend = Q(end,:);
165
166 end
```

below is the premaster test, for checking some of the programs.

```
format('long')
definehamilcellparam;

[V,D,V1,D1] = findhamilstates(hamilcellparam);

hamiloutcell = {V,D,V1,D1};

[TN2,TP2,T,SZS,SZS1,Ens,Ens1] = sortandCG(hamiloutcell,hamilcellparam);

sortCGoutcell = {TN2,TP2,T,SZS,SZS1,Ens,Ens1};

%%%%%%%%%%%%%%%%%%%%%%%%%%%%%%%%%%%%%%%%%%%%%%%%%%%%%%%%%%%%%%%%%%%%%%%%%%%%
%Can now run either full master equation simulation, or stochastic version%
%%%%%%%%%%%%%%%%%%%%%%%%%%%%%%%%%%%%%%%%%%%%%%%%%%%%%%%%%%%%%%%%%%%%%%%%%%%%
uLvals = 100;
uRvals = -1E5;
uL = uLvals;
uR = uRvals;
ktemp = 86*0.075;
RR = 6E7;
RL = 6E7;
PSL = 0;
PSR = 0;

h = 0;
dt = 10E-9;
t = 0:dt:6E-5;
initflag = true;
pinit = [1,zeros(1,2*S0)];
qinit = zeros(1,2*S01+1);

%simplemaster
```

```
33 loopparamscell = {uL,uR,ktemp,RL,RR,PSL,PSR,t,dt,pinit,qinit};
34 [m,pend,qend] = simplemaster(sortCGoutcell,loopparamscell);
35 figure; plot(m)
```

The next few programs will define some of the loops over the deterministic master equation program. In particular, I will describe how to calculate the differential conductance spectra based on the converged probability distribution of the master equation for different bias voltage and magnetic field values. There are two main forms of this program. In one form, the Fermi function in the right (that is, the drain) lead is set equal to zero, and the left (that is, the source) Fermi lead is allowed to vary. In the other form, the the Fermi function in the left (that is, the source) lead is set equal to one, and the right (that is, the drain) Fermi lead is allowed to vary. These spectra functions are quite general, and can as a special instance plot the magnetization S_z or the current I as a function of voltage or of magnetic field, based on the way the variables were defined. NOTE: The important concept for these master equation spectra simulations is that they should be run in a new data folder each time a new spectrum is required. This is because the loop over the master equation program will save an individual data file for each implementation of the simplemaster program, which ends up populating data folders with many files quickly. One way to accomplish this is to copy the relevant code files into a new folder, and then set the Matlab path to that new folder.

A.0.5 Defining uL (or uR) and the magnetic field

The following function can be used to initialize the chemical potential values and magnetic field values, based on the desired range and number of data points for each variable.

```
1 function [hvals,uLvals] = find_h_and_uL(numhvals,hrange,numuLvals,uLrange)
```

```
%FIND_H_AND_UL -- given the number of distinct magnetic field values
%numhvals, within the field range hrange=[hmin,hmax], and given the number
%of distinct bias electrochemical potential values numuLvals, within the
%range uLrange = [uLmin,uLmax], returns overall vectors for magnetic field
%values hvals and bias values uLvals, that will reproduce the structure
%employed in differential conductance spectra measurements. It is assumed
%that the magnetic field is swept slowly from hmin to hmax, while the bias
%voltage values are swept in a triangle wave from uLmin to uLmax.

h1 = linspace(hrange(1),hrange(2),numhvals);
uL1= linspace(uLrange(1),uLrange(2),numuLvals);
uL1 = uL1(:);

hvals = repmat(h1(:),[1,numuLvals]);
hvals = reshape(hvals',1,numuLvals*numhvals);

if mod(numhvals,2)== 0
    %even number of sweeps of uL
    uL2 = [uL1,uL1(end:-1:1)];
    uLvals = reshape(repmat(uL2,[1,numhvals/2]),1,numuLvals*numhvals);


else
    %odd number of sweeps of uL
    uL2 = [uL1,uL1(end:-1:1)];
    uLvals = repmat(uL2,[1,(numhvals-1)/2]);
    uLvals=  [uLvals,uL1];
    uLvals = reshape(uLvals,1,numuLvals*numhvals);
end


```

```
end
```

A.0.6 Define the Loop Parameters

The following script should be edited and run prior to running any loops over the full master equation simulation.

```
% defineloopparamscell.m
% This script should be run prior to running the run_masteruL program, in
% order to initialize the loopparamscell parameter data structure.
uL = uLvals(1);
uR = uRvals(1);
ktemp = 86*0.075; % to change the temperature in the leads, change ...
%the number that is multiplying 86. As it stands, this represents 75 mK,...
%and 86 is Boltzmann's constant in units of micro-eV/Kelvin.
RR = 6E7;
RL = 6E7/20;
PSL = 0;
PSR = 0;

h = hvals(1);
dt = 10E-9; %time step for master equation integration
t = 0:dt:6E-5; %vector of time values for integrating master equation

%below, pinit and qinit are the initial state probability distribution
%vectors for the N and N+1 electron particle eigenstates, respectively.
pinit = [1,zeros(1,2*S0)]; % this initializes the particle in the N ...
%electron particle ground state.
qinit = zeros(1,2*S01+1);

loopparamscell={uL,uR,ktemp,RL,RR,PSL,PSR,t,dt,pinit,qinit};
```

A.0.7 Looping simplemaster over uL

The following program changes the source Fermi lead electrochemical potential uL, as well as the magnetic field h, and loops over their values to save the converged data point files in the current folder.

```
function [] = masterloopuL(loopvals,hamilcellparam,loopparamscell)
%MASTERLOOPUL -- this program loops over the different values of uL and h
%to run simplemaster in each case, then saves the results in the current
%directory folder.

format('long')

%export values from the current loop parameters:
uL    = loopparamscell{1};
uR    = loopparamscell{2};
ktemp = loopparamscell{3};
RL    = loopparamscell{4};
RR    = loopparamscell{5};
PSL   = loopparamscell{6};
PSR   = loopparamscell{7};
t     = loopparamscell{8};
dt    = loopparamscell{9};
pinit = loopparamscell{10};
qinit = loopparamscell{11};
if RR>RL
    str_leadrate = 'hiR';
elseif RL>RR
    str_leadrate = 'hiL';
else
    str_leadrate = 'equalleads';
end
```

```
27
28 % export hamiltonian parameters from hamilcellparam cell:
29 S0 =       hamilcellparam{1};
30 S01 =      hamilcellparam{2};
31 epsilon =  hamilcellparam{3};
32 epsilonz = hamilcellparam{4};
33 theta_se = hamilcellparam{5};
34 kappa =    hamilcellparam{6};
35 h =        hamilcellparam{7};
36 Sx =       hamilcellparam{8};
37 Sy =       hamilcellparam{9};
38 Sz =       hamilcellparam{10};
39 Sx1 =      hamilcellparam{11};
40 Sy1 =      hamilcellparam{12};
41 Sz1 =      hamilcellparam{13};
42 Kzunianis= hamilcellparam{14};
43 Kbiax= hamilcellparam{15};
44
45 if ~exist('delta2','var')
46     delta2 = 0;
47 end
48
49 tic;
50
51 uLvals = loopvals{1};
52 uRvals = loopvals{2};
53 hvals  = loopvals{3};
54 uLaxis = loopvals{4};
55 haxis  = loopvals{5};
56
57 numsims = length(uLvals);
58 %run first loop separately....
```

```
h = hvals(1);
uL = uLvals(1);
uR = uRvals(1);
hamilcellparam{7} = h;
[V,D,V1,D1]=findhamilstates(hamilcellparam);
hamiloutcell = {V,D,V1,D1};
[TN2,TP2,T,SZS,SZS1,Ens,Ens1]=sortandCG(hamiloutcell,hamilcellparam);
sortCGoutcell = {TN2,TP2,T,SZS,SZS1,Ens,Ens1};


[m,pend,qend]= simplemaster(sortCGoutcell,loopparamscell);
toc
display([num2str(1/numsims*100) 'percent done'])

str = ['varyuL_PG_v_' str_leadrate '_SPECTRA_ZEEMAN_h_' num2str(h) ...
    '_S' num2str(S0) '_T_' num2str(ktemp/86) 'K_delta_' ...
    num2str(delta2) '_epz_' num2str(epsilonz/1000) '_angle_' ...
    num2str(theta_se/pi) 'pi_ep' num2str(epsilon/1000) '_bias_' ...
    num2str(1E-3*uL) 'mV.mat'];
save(str,'pend','qend','m')


for tind = 2:numsims
    uL = uLvals(tind);
    uR = uRvals(tind);
    h = hvals(tind);
    if h~=hvals(tind-1)
        hamilcellparam{7} = h;
        [V,D,V1,D1]=findhamilstates(hamilcellparam);
        hamiloutcell = {V,D,V1,D1};
        [TN2,TP2,T,SZS,SZS1,Ens,Ens1]=sortandCG(hamiloutcell,hamilcellparam);
```

```
91          sortCGoutcell = {TN2,TP2,T,SZS,SZS1,Ens,Ens1};
92      end
93
94      loopparamscell{1}  = uL;
95      loopparamscell{2}  = uR;
96      loopparamscell{10} = pend;
97      loopparamscell{11} = qend;
98
99
100     [m,pend,qend]= simplemaster(sortCGoutcell,loopparamscell);
101     toc
102     display([num2str(tind/numsims*100) 'percent done'])
103
104     str = ['varyuL_PG_v_' str_leadrate '_SPECTRA_ZEEMAN_h_' num2str(h) ...
105         '_S' num2str(S0) '_T_' num2str(ktemp/86) 'K_delta_' ...
106         num2str(delta2) '_epz_' num2str(epsilonz/1000) '_angle_' ...
107         num2str(theta_se/pi) 'pi_ep' num2str(epsilon/1000) '_bias_' ...
108         num2str(1E-3*uL) 'mV.mat'];
109     save(str,'pend','qend','m')
110
111 end
112
113 end
```

A.0.8 Plotting Spectra, Magnetization, and Current (varying uL)

This program will plot the results calculated in the previous loop program. Note that the saved files must be in the same folder as this program. The plotted results are stored as matrices, and saved as a new file in the same folder.

```
1 function [currentmat,conductmat,szprojmat] = ...
2     plotspecuL(hamilcellparam,loopparamscell,loopvals)
```

```
% Plot current, spectra, and magnetization as a function of magnetic field
% and bias energy uL, given the converged data point saved files from
% looping over the masterloopuL program.
%export values from the current loop parameters:
uL    = loopparamscell{1};
uR    = loopparamscell{2};
ktemp = loopparamscell{3};
RL    = loopparamscell{4};
RR    = loopparamscell{5};
PSL   = loopparamscell{6};
PSR   = loopparamscell{7};
t     = loopparamscell{8};
dt    = loopparamscell{9};
pinit = loopparamscell{10};
qinit = loopparamscell{11};
if RR>RL
    str_leadrate = 'hiR';
elseif RL>RR
    str_leadrate = 'hiL';
else
    str_leadrate = 'equalleads';
end

% export hamiltonian parameters from hamilcellparam cell:
S0 =       hamilcellparam{1};
S01 =      hamilcellparam{2};
epsilon =  hamilcellparam{3};
epsilonz = hamilcellparam{4};
theta_se = hamilcellparam{5};
kappa =    hamilcellparam{6};
h =        hamilcellparam{7};
Sx =       hamilcellparam{8};
```

```
Sy =       hamilcellparam{9};
Sz =       hamilcellparam{10};
Sx1 =      hamilcellparam{11};
Sy1 =      hamilcellparam{12};
Sz1 =      hamilcellparam{13};
Kzunianis= hamilcellparam{14};
Kbiax= hamilcellparam{15};

% export sweep parameters from loopvals cell:
uLvals = loopvals{1};
uRvals = loopvals{2};
hvals  = loopvals{3};
uLaxis = loopvals{4};
haxis  = loopvals{5};

currentmat = zeros(length(uLaxis),length(haxis));
conductmat = zeros(length(uLaxis)-1,length(haxis));
szprojmat = zeros(length(uLaxis),length(haxis));

for hind = 1:length(haxis)
    h = haxis(hind);
    hamilcellparam{7} = h;
    display(num2str(hind/length(haxis)*100));

    %Ens1c = Ens1;
    %plotiv_v_FAST_uL;
    [currentvec,conductvec,szprojvec] = findivuL(hamilcellparam, ...
    loopparamscell,loopvals);

    currentmat(:,hind) = currentvec;
    conductmat(:,hind) = conductvec;
    szprojmat(:,hind)  = szprojvec;
```

```
%     end
end
delta2 = 0;
figure; imagesc(uLaxis/1000,haxis,currentmat'); axis xy;
title(['vary \mu_L, Current vs. field and bias, \delta = ' ...
    num2str(delta2) ', ' str_leadrate]);
xlabel('Bias Energy \mu_L (meV)'); ylabel('Magetic Field (T)');
figure; imagesc(uLaxis(1:end-1)/1000,hvals,conductmat'); axis xy;
title(['Conductance vs. field and bias, \delta = ' num2str(delta2) ', ' ...
    str_leadrate]);
xlabel('Bias Energy \mu_L (mV)'); ylabel('Magetic Field (T)');
figure; imagesc(uLaxis/1000,haxis,szprojmat'); axis xy;
title('Magnetization vs. field and bias');
xlabel('Bias \mu_L (meV)'); ylabel('Magetic Field (T)')
save(['spectrafig_' num2str(epsilon/1000) 'meV_' str_leadrate ...
    '_vary_uL.mat'],'conductmat','currentmat',...
    'szprojmat','uLaxis','haxis');

end
```

A.0.9 Find the I(V) curve by varying uL

The following program is a subroutine of the above program. It is called for each slice of the spectra of constant magnetic field. If the number of magnetic field values is chosen to be one, then this will simply find the I(V) curve.

```
function [currentvec,conductvec,szprojvec] = findivuL(hamilcellparam, ...
    loopparamscell,loopvals)
%Plot IV-- given data from master equation solutions at different bias
%voltage values (for the left lead) uL, this function will calculate the
%current output as a function of bias and plot the result.
format('long')
```

```
7
8  %export values from the current loop parameters:
9  uL    = loopparamscell{1};
10 uR    = loopparamscell{2};
11 ktemp = loopparamscell{3};
12 RL    = loopparamscell{4};
13 RR    = loopparamscell{5};
14 PSL   = loopparamscell{6};
15 PSR   = loopparamscell{7};
16 t     = loopparamscell{8};
17 dt    = loopparamscell{9};
18 pinit = loopparamscell{10};
19 qinit = loopparamscell{11};
20 if RR>RL
21     str_leadrate = 'hiR';
22 elseif RL>RR
23     str_leadrate = 'hiL';
24 else
25     str_leadrate = 'equalleads';
26 end
27
28 % export hamiltonian parameters from hamilcellparam cell:
29 S0 =       hamilcellparam{1};
30 S01 =      hamilcellparam{2};
31 epsilon =  hamilcellparam{3};
32 epsilonz = hamilcellparam{4};
33 theta_se = hamilcellparam{5};
34 kappa =    hamilcellparam{6};
35 h =        hamilcellparam{7};
36 Sx =       hamilcellparam{8};
37 Sy =       hamilcellparam{9};
38 Sz =       hamilcellparam{10};
```

```
Sx1 =      hamilcellparam{11};
Sy1 =      hamilcellparam{12};
Sz1 =      hamilcellparam{13};
Kzunianis= hamilcellparam{14};
Kbiax= hamilcellparam{15};

% export sweep parameters from loopvals cell:
uLvals = loopvals{1};
uRvals = loopvals{2};
hvals  = loopvals{3};
uLaxis = loopvals{4};
haxis  = loopvals{5};

currentvec= zeros(1,length(uLaxis));
szprojvec = zeros(1,length(uLaxis));

%hamilcellparam = {S0,S01,epsilon,epsilonz,theta_se,kappa,h,Sx,Sy,Sz, ...
%Sx1,Sy1,Sz1,Kzunianis,Kbiax};
[V,D,V1,D1] = findhamilstates(hamilcellparam);
hamiloutcell = {V,D,V1,D1};
[TN2,TP2,T,SZS,SZS1,Ens,Ens1] = sortandCG(hamiloutcell,hamilcellparam);
sortCGoutcell = {TN2,TP2,T,SZS,SZS1,Ens,Ens1};

%Costates4_nos; indexeadd; CGpra_vectorized_pg; T_0p3pi = T;
%Ens1c = Ens1;


Ensmat = repmat(Ens',[2*S01+1,1]);
Ens1mat = repmat(Ens1,[1,2*S0+1]);

fL = 1./(1+exp((Ens1mat-Ensmat-uL)./ktemp));
fR = 1./(1+exp((Ens1mat-Ensmat-uR)./ktemp));
```

```
71
72 %figure; imagesc(T);
73 % for indvp=1:length(uRvals)
74 for indvp=1:length(uLaxis)
75     uL = uLaxis(indvp);
76     delta2 = 0;
77
78     str = ['varyuL_PG_v_' str_leadrate '_SPECTRA_ZEEMAN_h_' num2str(h) ...
79         '_S' num2str(S0) '_T_' num2str(ktemp/86) 'K_delta_' ...
80         num2str(delta2) '_epz_' num2str(epsilonz/1000) '_angle_' ...
81         num2str(theta_se/pi) 'pi_ep' num2str(epsilon/1000) '_bias_' ...
82         num2str(1E-3*uL) 'mV.mat'];
83     load(str);
84
85     szprojvec(indvp) = m(end);
86
87
88     for alpha = 1:length(Ens)
89        for beta = 1:length(Ens1)
90            fermifunc(alpha,beta) = 1./(exp((Ens1(beta)-Ens(alpha)-uL)/ktemp)+1);
91
92        end
93     end
94
95
96     for alpha = 1:length(Ens)
97         for beta = 1:length(Ens1)
98
99             currentvec(indvp) = currentvec(indvp)+ ...
100            fermifunc(alpha,beta)*T(beta,alpha)*pend(alpha);
101
102        end
```

```
103     end
104
105 end
106
107 gammaL = 2*RR*RL/(RR+RL);
108 q = 1.6E-19; %electronic charge
109 ccoef = gammaL*q*1E12;
110 %coefficient of current in units of pico-amps
111 currentvec = currentvec*ccoef;
112
113 conductvec = diff(currentvec)/mean(diff(uLaxis));
114
115 end
```

A.0.10 Calculating and Plotting, looping over the master equation by varying uL

The following program combines all of the above programs and both calculates and plots the spectra, using the full master equation.

```
1  %run_masteruL.m
2  % The values below should be edited to their desired parameter values prior
3  % to running the script. This script loops over the different uL values and
4  % magnetic field values, and both saves the converged data and plots the
5  % resulting spectra.
6  numhvals = 31;
7  hrange = [-3,10];
8  numuLvals = 41;
9  %uLrange = [-2.5E3,2.5E3];
10 uLrange = [-2.5E3,2.5E3];
11 [hvals,uLvals] = find_h_and_uL(numhvals,hrange,numuLvals,uLrange);
12 uRvals = -1E5*ones(size(uLvals));
```

```
13
14 uLaxis = linspace(uLrange(1),uLrange(2),numuLvals);
15 haxis  = linspace(hrange(1),hrange(2),numhvals);
16 loopvals = {uLvals,uRvals,hvals,uLaxis,haxis};
17
18 definehamilcellparam;
19
20 defineloopparamscell;
21
22 hamilcellparam{7} = hvals(1);
23
24
25
26 masterloopuL(loopvals,hamilcellparam,loopparamscell);
27
28 [currentmat,conductmat,szprojmat] = ...
29     plotspecuL(hamilcellparam,loopparamscell,loopvals);
30
31 figure; plot(currentmat)
```

A.1 Varying uR

The next few programs are identical to those in the previous section, with the exception that the right (drain) fermi lead is varied, while the left (source) fermi lead is held at a constant value of one.

```
1 function [] = masterloopuR(loopvals,hamilcellparam,loopparamscell)
2 %MASTERLOOPUR -- this function loops through the different uR values and
3 %magnetic field values by running simplemaster and saves the results in the
4 %current directory folder.
5 format('long')
6
```

```
%export values from the current loop parameters:
uL    = loopparamscell{1};
uR    = loopparamscell{2};
ktemp = loopparamscell{3};
RL    = loopparamscell{4};
RR    = loopparamscell{5};
PSL   = loopparamscell{6};
PSR   = loopparamscell{7};
t     = loopparamscell{8};
dt    = loopparamscell{9};
pinit = loopparamscell{10};
qinit = loopparamscell{11};
if RR>RL
    str_leadrate = 'hiR';
elseif RL>RR
    str_leadrate = 'hiL';
else
    str_leadrate = 'equalleads';
end

% export hamiltonian parameters from hamilcellparam cell:
S0 =       hamilcellparam{1};
S01 =      hamilcellparam{2};
epsilon =  hamilcellparam{3};
epsilonz = hamilcellparam{4};
theta_se = hamilcellparam{5};
kappa =    hamilcellparam{6};
h =        hamilcellparam{7};
Sx =       hamilcellparam{8};
Sy =       hamilcellparam{9};
Sz =       hamilcellparam{10};
Sx1 =      hamilcellparam{11};
```

```
Sy1 =      hamilcellparam{12};
Sz1 =      hamilcellparam{13};
Kzunianis= hamilcellparam{14};
Kbiax= hamilcellparam{15};

if ~exist('delta2','var')
    delta2 = 0;
end

tic;

uLvals = loopvals{1};
uRvals = loopvals{2};
hvals  = loopvals{3};
uLaxis = loopvals{4};
haxis  = loopvals{5};

numsims = length(uLvals);
%run first loop separately....
h = hvals(1);
uL = uLvals(1);
uR = uRvals(1);
hamilcellparam{7} = h;
[V,D,V1,D1]=findhamilstates(hamilcellparam);
hamiloutcell = {V,D,V1,D1};
[TN2,TP2,T,SZS,SZS1,Ens,Ens1]=sortandCG(hamiloutcell,hamilcellparam);
sortCGoutcell = {TN2,TP2,T,SZS,SZS1,Ens,Ens1};


[m,pend,qend]= simplemaster(sortCGoutcell,loopparamscell);
toc
display([num2str(1/numsims*100) 'percent done'])
```

```
71
72 str = ['varyuR_PG_v_' str_leadrate '_SPECTRA_ZEEMAN_h_' num2str(h) ...
73         '_S' num2str(S0) '_T_' num2str(ktemp/86) 'K_delta_' ...
74         num2str(delta2) '_epz_' num2str(epsilonz/1000) '_angle_' ...
75         num2str(theta_se/pi) 'pi_ep' num2str(epsilon/1000) '_bias_' ...
76         num2str(1E-3*uR) 'mV.mat'];
77 save(str,'pend','qend','m')
78
79
80
81 for tind = 2:numsims
82     uL = uLvals(tind);
83     uR = uRvals(tind);
84     h = hvals(tind);
85     if h~=hvals(tind-1)
86         hamilcellparam{7} = h;
87         [V,D,V1,D1]=findhamilstates(hamilcellparam);
88         hamiloutcell = {V,D,V1,D1};
89         [TN2,TP2,T,SZS,SZS1,Ens,Ens1]=sortandCG(hamiloutcell,hamilcellparam);
90         sortCGoutcell = {TN2,TP2,T,SZS,SZS1,Ens,Ens1};
91     end
92
93     loopparamscell{1}  = uL;
94     loopparamscell{2}  = uR;
95     loopparamscell{10} = pend;
96     loopparamscell{11} = qend;
97
98
99     [m,pend,qend]= simplemaster(sortCGoutcell,loopparamscell);
100    toc
101    display([num2str(tind/numsims*100) 'percent done'])
102
```

```
103       str = ['varyuR_PG_v_' str_leadrate '_SPECTRA_ZEEMAN_h_' num2str(h) ...
104          '_S' num2str(S0) '_T_' num2str(ktemp/86) 'K_delta_' ...
105          num2str(delta2) '_epz_' num2str(epsilonz/1000) '_angle_' ...
106          num2str(theta_se/pi) 'pi_ep' num2str(epsilon/1000) '_bias_' ...
107          num2str(1E-3*uR) 'mV.mat'];
108      save(str,'pend','qend','m')
109
110
111
112
113 end
114
115 end
```

plotspecuR

```
1  function [currentmat,conductmat,szprojmat] = ...
2      plotspecuR(hamilcellparam,loopparamscell,loopvals)
3  % Plot current, spectra, and magnetization as a function of magnetic field
4  % and bias energy uR.
5  %export values from the current loop parameters:
6  uL    = loopparamscell{1};
7  uR    = loopparamscell{2};
8  ktemp = loopparamscell{3};
9  RL    = loopparamscell{4};
10 RR    = loopparamscell{5};
11 PSL   = loopparamscell{6};
12 PSR   = loopparamscell{7};
13 t     = loopparamscell{8};
14 dt    = loopparamscell{9};
15 pinit = loopparamscell{10};
16 qinit = loopparamscell{11};
```

```
17 if RR>RL
18     str_leadrate = 'hiR';
19 elseif RL>RR
20     str_leadrate = 'hiL';
21 else
22     str_leadrate = 'equalleads';
23 end
24
25 % export hamiltonian parameters from hamilcellparam cell:
26 S0 =       hamilcellparam{1};
27 S01 =      hamilcellparam{2};
28 epsilon =  hamilcellparam{3};
29 epsilonz = hamilcellparam{4};
30 theta_se = hamilcellparam{5};
31 kappa =    hamilcellparam{6};
32 h =        hamilcellparam{7};
33 Sx =       hamilcellparam{8};
34 Sy =       hamilcellparam{9};
35 Sz =       hamilcellparam{10};
36 Sx1 =      hamilcellparam{11};
37 Sy1 =      hamilcellparam{12};
38 Sz1 =      hamilcellparam{13};
39 Kzunianis= hamilcellparam{14};
40 Kbiax= hamilcellparam{15};
41
42 % export sweep parameters from loopvals cell:
43 uLvals = loopvals{1};
44 uRvals = loopvals{2};
45 hvals  = loopvals{3};
46 uRaxis = loopvals{4};
47 haxis  = loopvals{5};
48
```

```
currentmat = zeros(length(uRaxis),length(haxis));
conductmat = zeros(length(uRaxis)-1,length(haxis));
szprojmat = zeros(length(uRaxis),length(haxis));

for hind = 1:length(haxis)
    h = haxis(hind);
    hamilcellparam{7} = h;
    display(num2str(hind/length(haxis)*100));

    %Ens1c = Ens1;
    %plotiv_v_FAST_uL;
    [currentvec,conductvec,szprojvec] = findivuR(hamilcellparam, ...
    loopparamscell,loopvals);

    currentmat(:,hind) = currentvec;
    conductmat(:,hind) = conductvec;
    szprojmat(:,hind)  = szprojvec;
%     end
end
delta2 = 0;
figure; imagesc(uRaxis/1000,haxis,currentmat'); axis xy;
title(['vary \mu_L, Current vs. field and bias, \delta = ' ...
    num2str(delta2) ', ' str_leadrate]);
xlabel('Bias Energy \mu_L (meV)'); ylabel('Magetic Field (T)');
figure; imagesc(uRaxis(1:end-1)/1000,hvals,-conductmat'); axis xy;
title(['Conductance vs. field and bias, \delta = ' num2str(delta2) ', ' ...
    str_leadrate]);
xlabel('Bias Energy \mu_L (mV)'); ylabel('Magetic Field (T)');
figure; imagesc(uRaxis/1000,haxis,szprojmat'); axis xy;
title('Magnetization vs. field and bias');
xlabel('Bias \mu_L (meV)'); ylabel('Magetic Field (T)')

```

```
save(['spectrafig_' num2str(epsilon/1000) 'meV_' str_leadrate ...
    '_vary_uL.mat'],'conductmat','currentmat',...
    'szprojmat','uRaxis','haxis');

end
```

findivuR

```
function [currentvec,conductvec,szprojvec] = findivuR(hamilcellparam, ...
    loopparamscell,loopvals)
%Plot IV-- given data from master equation solutions at different bias
%voltage values (for the right lead) uR, this function will calculate the
%current output as a function of bias and plot the result.
format('long')

%export values from the current loop parameters:
uL    = loopparamscell{1};
uR    = loopparamscell{2};
ktemp = loopparamscell{3};
RL    = loopparamscell{4};
RR    = loopparamscell{5};
PSL   = loopparamscell{6};
PSR   = loopparamscell{7};
t     = loopparamscell{8};
dt    = loopparamscell{9};
pinit = loopparamscell{10};
qinit = loopparamscell{11};
if RR>RL
    str_leadrate = 'hiR';
elseif RL>RR
    str_leadrate = 'hiL';
else
```

```
25      str_leadrate = 'equalleads';
26  end
27
28  % export hamiltonian parameters from hamilcellparam cell:
29  S0 =        hamilcellparam{1};
30  S01 =       hamilcellparam{2};
31  epsilon =   hamilcellparam{3};
32  epsilonz =  hamilcellparam{4};
33  theta_se =  hamilcellparam{5};
34  kappa =     hamilcellparam{6};
35  h =         hamilcellparam{7};
36  Sx =        hamilcellparam{8};
37  Sy =        hamilcellparam{9};
38  Sz =        hamilcellparam{10};
39  Sx1 =       hamilcellparam{11};
40  Sy1 =       hamilcellparam{12};
41  Sz1 =       hamilcellparam{13};
42  Kzunianis=  hamilcellparam{14};
43  Kbiax=  hamilcellparam{15};
44
45  % export sweep parameters from loopvals cell:
46  uLvals = loopvals{1};
47  uRvals = loopvals{2};
48  hvals  = loopvals{3};
49  uRaxis = loopvals{4};
50  haxis  = loopvals{5};
51
52  currentvec= zeros(1,length(uRaxis));
53  szprojvec = zeros(1,length(uRaxis));
54
55  %hamilcellparam = {S0,S01,epsilon,epsilonz,theta_se,kappa,h,Sx,Sy,Sz, ...
56  %Sx1,Sy1,Sz1,Kzunianis,Kbiax};
```

```
[V,D,V1,D1] = findhamilstates(hamilcellparam);
hamiloutcell = {V,D,V1,D1};
[TN2,TP2,T,SZS,SZS1,Ens,Ens1] = sortandCG(hamiloutcell,hamilcellparam);
sortCGoutcell = {TN2,TP2,T,SZS,SZS1,Ens,Ens1};

%Costates4_nos; indexeadd; CGpra_vectorized_pg; T_0p3pi = T;
%Ens1c = Ens1;


Ensmat = repmat(Ens',[2*S01+1,1]);
Ens1mat = repmat(Ens1,[1,2*S0+1]);

fL = 1./(1+exp((Ens1mat-Ensmat-uL)./ktemp));
fR = 1./(1+exp((Ens1mat-Ensmat-uR)./ktemp));

%figure; imagesc(T);
% for indvp=1:length(uRvals)
for indvp=1:length(uRaxis)
    uR = uRaxis(indvp);
    delta2 = 0;

    str = ['varyuR_PG_v_' str_leadrate '_SPECTRA_ZEEMAN_h_' num2str(h) ...
        '_S' num2str(S0) '_T_' num2str(ktemp/86) 'K_delta_' ...
        num2str(delta2) '_epz_' num2str(epsilonz/1000) '_angle_' ...
        num2str(theta_se/pi) 'pi_ep' num2str(epsilon/1000) '_bias_' ...
        num2str(1E-3*uR) 'mV.mat'];
    load(str);

    szprojvec(indvp) = m(end);


    for alpha = 1:length(Ens)
```

```
89          for beta = 1:length(Ens1)
90
91              fermifunc(alpha,beta) = 1-1./(exp((Ens1(beta)-Ens(alpha)-uR)/ktemp)+1);
92          end
93      end
94
95
96      for alpha = 1:length(Ens)
97          for beta = 1:length(Ens1)
98
99              currentvec(indvp) = currentvec(indvp)+ ...
100             fermifunc(alpha,beta)*T(beta,alpha)*pend(alpha);
101
102         end
103     end
104
105 end
106
107 gammaL = 2*RR*RL/(RR+RL);
108 q = 1.6E-19; %electronic charge
109 ccoef = gammaL*q*1E12;
110 %coefficient of current in units of pico-amps
111 currentvec = currentvec*ccoef;
112
113 conductvec = diff(currentvec)/mean(diff(uRaxis));
114
115 end
```

```
1 %run_masteruR.m
2 % The values below should be edited to their desired parameter values prior
3 % to running the script. This script loops over the different uR values and
```

```
% magnetic field values, and both saves the converged data and plots the
% resulting spectra.
numhvals = 31;
hrange = [-3,10];
numuRvals = 41;
%uLrange = [-2.5E3,2.5E3];
uRrange = [-2.5E3,2.5E3];
[hvals,uRvals] = find_h_and_uL(numhvals,hrange,numuRvals,uRrange);
uLvals = 1E5*ones(size(uRvals));

uRaxis = linspace(uRrange(1),uRrange(2),numuRvals);
haxis  = linspace(hrange(1),hrange(2),numhvals);
loopvals = {uLvals,uRvals,hvals,uRaxis,haxis};

definehamilcellparam;

defineloopparamscell;

hamilcellparam{7} = hvals(1);



masterloopuR(loopvals,hamilcellparam,loopparamscell);

[currentmat,conductmat,szprojmat] = ...
    plotspecuR(hamilcellparam,loopparamscell,loopvals);

figure; plot(currentmat)
```

A.1.1 Stochastic Evolution Code

In this section, I will describe the stochastic eigenstate evolution code. First, I will list the subroutine function that generates a random event based on the current

state-change probability distribution, using Matlab's built-in pseudo-random number generator, 'rand', which returns a uniformly distributed random floating point number between 0 and 1. This function 'genrand' returns an index in the total state vector.

```
function index_of_p = genrand(stateprob)
%this function will take an input state probability distribution function
%stateprob and find the cumulative probability distribution cp, and
%generate a random number to sample from cp, and output the index in the
%probability distribution
cp = cumsum(stateprob);
cp = cp/max(cp);

index_of_p=find(cp>rand(1),1);
end
```

The next program should be implemented each time the magnetic field changes. It calculates the overlap of the previous eigenstate with the new set of eigenstates, and assumes that the new state probability distribution is given by the state which has a maximum overlap with the initial state.

```
function newstateprob = statechangedbv(stateprob,hinit,hnew,hamilcellparam)
%STATECHANGEDBV -- given input state probability distribution (from the previous
%time step, and the initial and new magnetic field values at the initial time
%step and the new time step, and a cell of hamiltonian parameters hamilcellparam
% this function is used when there is a transition between eigenstates as
%B --> B + dB.
% This script determines the closest eigenstate of H(B+dB) to H(B) as the
% magnetic field changes from B to B+dB.


```

```
S0 = hamilcellparam{1};
S01 = hamilcellparam{2};

%hamilcellparam = {S0,S01,epsilon,epsilonz,theta_se,kappa,h,Sx,Sy,Sz, ...
    %Sx1,Sy1,Sz1,Kzunianis,Kbiax};


%calculate states for previous magnetic field value:
hamilcellparam{7} = hinit;
[V,D,V1,D1] = findhamilstates(hamilcellparam);
hamiloutcell = {V,D,V1,D1};
[TN2,TP2,T,SZS,SZS1,Ens,Ens1] = sortandCG(hamiloutcell,hamilcellparam);
sortCGoutcell = {TN2,TP2,T,SZS,SZS1,Ens,Ens1};

Vold = V;
V1old = V1;


%calculate states for new magnetic field value:
hamilcellparam{7} = hnew;
[V,D,V1,D1] = findhamilstates(hamilcellparam);
hamiloutcell = {V,D,V1,D1};
[TN2,TP2,T,SZS,SZS1,Ens,Ens1] = sortandCG(hamiloutcell,hamilcellparam);
sortCGoutcell = {TN2,TP2,T,SZS,SZS1,Ens,Ens1};

Vnew = V;
V1new = V1;

stateprobind = find(stateprob==max(stateprob),1);
if stateprobind>2*S0+1
    %state is in Q. that is, N+1-electron case.
```

```
    oldstate = V1old(:,stateprobind-(2*S0+1));

    indnewstate = find(abs(real(oldstate'*V1new))==max(abs(real(oldstate'*V1new))));
    Q = zeros(1,2*S01+1); Q(indnewstate)=1;
    P = zeros(1,2*S0+1);
    newstateprob = [P,Q];
else
    %state is in P. that is, N-electron case.
    oldstate = Vold(:,stateprobind);
    indnewstate = find(abs(real(oldstate'*Vnew))==max(abs(real(oldstate'*Vnew))));
    Q = zeros(1,2*S01+1);
    P = zeros(1,2*S0+1); P(indnewstate)=1;
    newstateprob = [P,Q];
end

% if newstateprob ~= stateprob
%     bprojflag = bprojflag+1;
% end


end
```

The following program is a subroutine to be used in defining the magnetic field values and the applied bias voltage as a function of time:

```
function [hvals,uLvals] = find_h_and_uL(numhvals,hrange,numuLvals,uLrange)
%FIND_H_AND_UL -- given the number of distinct magnetic field values
%numhvals, within the field range hrange=[hmin,hmax], and given the number
%of distinct bias electrochemical potential values numuLvals, within the
%range uLrange = [uLmin,uLmax], returns overall vectors for magnetic field
%values hvals and bias values uLvals, that will reproduce the structure
%employed in differential conductance spectra measurements. It is assumed
```

```
%that the magnetic field is swept slowly from hmin to hmax, while the bias
%voltage values are swept in a triangle wave from uLmin to uLmax.

h1 = linspace(hrange(1),hrange(2),numhvals);
uL1= linspace(uLrange(1),uLrange(2),numuLvals);
uL1 = uL1(:);

hvals = repmat(h1(:),[1,numuLvals]);
hvals = reshape(hvals',1,numuLvals*numhvals);

if mod(numhvals,2)== 0
    %even number of sweeps of uL
    uL2 = [uL1,uL1(end:-1:1)];
    uLvals = reshape(repmat(uL2,[1,numhvals/2]),1,numuLvals*numhvals);


else
    %odd number of sweeps of uL
    uL2 = [uL1,uL1(end:-1:1)];
    uLvals = repmat(uL2,[1,(numhvals-1)/2]);
    uLvals=  [uLvals,uL1];
    uLvals = reshape(uLvals,1,numuLvals*numhvals);
end

end
```

Next, I include the full stochastic code. The basic program is called stochastic_master_spectra, used for running a calculation of the differential conductance spectra for a given set of Hamiltonian parameters. First, the script run_stochmasterspec is run, which calls the stochastic_master_spectra function. All of the relevant parameters should be defined in the run_stochmasterspec first few lines. This function also calls the find_h_and_uL function, which calculates the magnetic field and bias

energy uL as a function of time, given the input parameters. It should be noted that, although these programs contain the word 'spec', implying a calculation of the differential conductance spectrum, they can equally well be used to calculate a single I(V) curve, if the magnetic field range hrange contains the same value for hmin and hmax, and if the number of distinct magnetic field values is set to one: numhvals =1. One-sided hysteresis loops can be run as well, if numuLvals is set to one. Alternatively, for a full hysteresis loop, the line below the hvals definition in the run_stochmasterspec program can be uncommented. This code can also be used for running spin-polarized switching simulations, such as the voltage-driven Spin-Transfer Torque methods discussed in the main text of the dissertation. This can be performed by changing PSL and PSR in the initial few lines of the run_stochmasterspec code below.

```

%%%%%%%%%%%%%%%%%%%%%%%%%%%%%%%%%%%%%%%%%%%%%%%%%%%%%%%%%%%%%%%%%%%%%%%%%%%
% Set Hamiltonian Parameters below, prior to running the ...
%
% stochastic_master_spectra program
%
%%%%%%%%%%%%%%%%%%%%%%%%%%%%%%%%%%%%%%%%%%%%%%%%%%%%%%%%%%%%%%%%%%%%%%%%%%%

definehamilcellparam;


PSL   = 0; %spin polarization in left (source) lead
PSR   = 0; %spin polarization in right (drain) lead
RR    = 6E7; %bare tunneling rate in the right (drain) lead
RL    = 6E7/20; %bare tunneling rate in the left (source) lead

numhvals = 1E3; % umber of distinct b-field values
hrange = [-3,10];%[range of b-field values, of form [min_h,max_h]
```

```
numuLvals = 1E4; %number of distinct uL bias values
uLrange = [-2.5E3,2.5E3]; %range of uL bias values


[hvals,uLvals] = find_h_and_uL(numhvals,hrange,numuLvals,uLrange);
% The line below can be uncommented when it is desired to run a full hysteresis loop
%hvals = [hvals,hvals(end:-1:1)];
%uLvals = [uLvals,uLvals];
uRvals= -1E5*ones(size(uLvals));

dt = 10E-9; %time step
tvals = dt*[0:1:(length(uLvals)-1)]; %vector of time values

% the cell below is input into the stochastic_master_spectra program
stochloopparamcell= {S0,S01,PSL,PSR,RR,RL,ktemp,epsilon,epsilonz, ...
    theta_se,kappa,hvals,uLvals,uRvals,tvals,Kzunianis,Kbiax};

%run the stochastic_master_spectra program:
[stochmasterspecout] = stochastic_master_spectra(stochloopparamcell);
%stochmasterspecout = {mvalue,currentvector,hvals,uLvals,uRvals,tvals};
%extract the magnetization (mvalue) and the current (currentvector) as a
%function of time:
mvalue = stochmasterspecout{1};
currentvector = stochmasterspecout{2};

%define two matrices containing the current and magnetization vectors,
%ordered in order to plot them vs. applied magnetic field and applied bias
%energy uL:
currentmat = reshape(currentvector, numuLvals,numhvals);
mvaluemat = reshape(mvalue, numuLvals,numhvals);
%the following loop accounts for the fact that the simulation sweeps the
%bias energy uL in a triangle wave, but is plotted in sorted format:
```

```
for hind = 2:2:numhvals
   currentmat(:,hind) = currentmat(end:-1:1,hind);
   mvaluemat(:,hind) = mvaluemat(end:-1:1,hind);
end
%define axes for magnetic field and bias energy uL:
haxis = linspace(hrange(1),hrange(2),numhvals);
uLaxis = linspace(uLrange(1),uLrange(2),numuLvals);
%define conductance matrix by taking derivative of current matrix:
condmat = diff(currentmat,1,1);



%the following loop checks the existence of a file name, and then saves the
%data from the most recent simulation in a new file name, without
%overwriting.
scount = 1;
strsave = ['spec_ws' num2str(scount) '.mat'];
flag = true;
while flag
    if exist(strsave,'file')
        scount = scount+1;
        strsave = ['spec_ws' num2str(scount) '.mat'];
    else
        flag = false;
    end
end
save(strsave);

%plot current and conductance matrices:
figure; imagesc(uLaxis,haxis,currentmat'); axis xy;
figure; imagesc(uLaxis(1:end-1),haxis,condmat'); axis xy;
%plot magnetization matrix:
```

```
figure; imagesc(uLaxis,haxis,mvaluemat'); axis xy;

%uncomment below to plot hysteresis loops:
%npts = length(hvals)/2;
%ind1 = 1:npts;
%ind2 = (npts+1):length(hvals);
%figure; plot(hvals(ind1),mvalue(ind1),'k'); hold on;
%plot(hvals(ind2),mvalue(ind2),'r');



function [stochmasterspecout] = stochastic_master_spectra(stochloopparamcell)

% This script will calculate the temporal evolution of the magnetization of
% a Ni nanoparticle, due to the influence of single electron tunneling from
% spin-polarized leads. It takes the state transition probabilities from
% the master equation distribution, and generates a random event at each
% timestep, governed by the probability distribution of state transitions.
% At each timestep, the particle is assumed to be in an eigenstate of the
% tunneling hamiltonian |alpha>. The component Sz of the state alpha is
% recorded at each time step, that is, <alpha|Sz|alpha>. Outputs cell
% stochmasterspecout = {mvalue,currentvector,hvals,uLvals,uRvals,tvals}.


% This version is to be used to generate time-dependent, stochastic ...
% dI/dV spectra.

format('long');

%rng('default'); rng(1);  % uncomment this line to choose to initialize the
%pseudo-random number generator and set seed to 1 for reproducibility.

tic;
```

```
23
24 S0    = stochloopparamcell{1};
25 S01   = stochloopparamcell{2};
26 PSL   = stochloopparamcell{3};
27 PSR   = stochloopparamcell{4};
28 RR    = stochloopparamcell{5};
29 RL    = stochloopparamcell{6};
30 ktemp = stochloopparamcell{7};
31 epsilon =stochloopparamcell{8};
32 epsilonz=stochloopparamcell{9};
33 theta_se=stochloopparamcell{10};
34 kappa  =stochloopparamcell{11};
35 hvals = stochloopparamcell{12};
36 uLvals= stochloopparamcell{13};
37 uRvals= stochloopparamcell{14};
38 tvals = stochloopparamcell{15};
39 Kzunianis = stochloopparamcell{16};
40 Kbiax = stochloopparamcell{17};
41
42 [Sx,Sy,Sz,Sx1,Sy1,Sz1] = findspinoperators(S0,S01);
43 RLu = (1+PSL)*RL;
44 RLd = (1-PSL)*RL;
45 RRu = (1+PSR)*RR;
46 RRd = (1-PSR)*RR;
47
48
49
50 %[TN2,TP2,T,SZS,SZS1,Ens,Ens1] = sortandCG(hamiloutcell,hamilcellparam);
51
52
53 mtime = tvals;%0:tau:(100*201-1)*tau;
54 tau = mean(diff(tvals));
```

```
55 uL = uLvals(1);
56 uR = uRvals(1);
57 h = hvals(1);
58 currentvector = zeros(size(mtime)); %initialize current values to zero
59
60
61 hamilcellparam = {S0,S01,epsilon,epsilonz,theta_se,kappa,h,Sx,Sy,Sz, ...
62     Sx1,Sy1,Sz1,Kzunianis,Kbiax};
63 [V,D,V1,D1] = findhamilstates(hamilcellparam);
64 hamiloutcell = {V,D,V1,D1};
65 [TN2,TP2,T,SZS,SZS1,Ens,Ens1] = sortandCG(hamiloutcell,hamilcellparam);
66 sortCGoutcell = {TN2,TP2,T,SZS,SZS1,Ens,Ens1};
67
68
69
70 Ttu=TP2(1:2*S01+1,1:2*S0+1);
71 Ttd=TN2(1:2*S01+1,1:2*S0+1);
72
73 mvalue = zeros(size(mtime));
74
75 P = zeros(1,2*S0+1);
76 % probability distribution of N electron particle states
77
78 Q = zeros(1,2*S01+1);
79 % probability distribution of N+1 electron particle states
80 dP = zeros(size(P));
81 dQ = zeros(size(Q));
82
83 pstateup = false;
84 if pstateup == true
85     Q(end)=1;
86     %initialize particle in N+1 electron state, with Sz1 near +S01.
```

```
87
88 else
89     Q(1)=1;
90     %initialize particle in N+1 electron state, with Sz1 near -S01.
91
92 end
93 flagnp1=true;
94 %keeps track of whether the particle has N+1 electrons.
95
96 stateprob = [P,Q];
97 % total probability distribution among N and N+1 electron particle states
98
99 cstateprob = cumsum(stateprob);
100
101 mvalue(1) = P*SZS+Q*SZS1;
102 %yields magnetization value, based on total spin-projection ...
103 %of particle along z axis.
104
105
106
107 Ensmat = repmat(Ens',[2*S01+1,1]);
108 Ens1mat = repmat(Ens1,[1,2*S0+1]);
109
110 fL = 1./(1+exp((Ens1mat-Ensmat-uL)./ktemp));
111 fR = 1./(1+exp((Ens1mat-Ensmat-uR)./ktemp));
112
113 % the above is the vectorized equivalent of the following ...
114 %nested loops:
115
116 %         for j=1:2*S0+1
117 %             for i=1:2*S01+1
118 %                 fL(i,j)=1/(exp((Ens1(i)-Ens(j)-uL)/ktemp)+1);
```

```
119 %                 fR(i,j)=1/(exp((Ens1(i)-Ens(j)-uR)/ktemp)+1);
120 %             end
121 %         end
122
123
124 currentvector(1) = sum((fL.*T)*P')+sum((fL.*T)'*Q');
125
126 %the above is the vectorized version of the following nested loops:
127
128 %         for alpha = 1:length(Ens)
129 %             for beta = 1:length(Ens1)
130 %                 currentvector(1) = currentvector(1)+ ...
131 %fL(beta,alpha)*T(beta,alpha)*P(alpha)+ ...
132 %fL(beta,alpha)'*T(beta,alpha)'*Q(beta);
133 %             end
134 %         end
135
136 TfLu = RLu*times(Ttu,fL);
137 %matrix element for tunneling on to particle from left lead, spin up
138
139 TfLd = RLd*times(Ttd,fL);
140 %matrix element for tunneling on to particle from left lead, spin down
141
142 TfLua = RLu*times(Ttu,1-fL);
143 %matrix element for tunneling off of particle into left lead, spin up
144
145 TfLda = RLd*times(Ttd,1-fL);
146 %matrix element for tunneling off of particle into left lead, spin down
147
148 TfRu = RRu*times(Ttu,fR);
149 %matrix element for tunneling on to particle from right lead, spin up
150
```

```
151 TfRd = RRd*times(Ttd,fR);
152 %matrix element for tunneling on to particle from right lead, spin down
153
154 TfRua = RRu*times(Ttu, 1-fR);
155 %matrix element for tunneling off of particle into right lead, spin up
156
157 TfRda = RRd*times(Ttd, 1-fR);
158 %matrix element for tunneling off of particle into right lead, spin down
159
160 Tfu = TfLu + TfRu;
161 % total matrix element of spin up electron tunneling onto particle from ...
162 % both leads
163
164 Tfd = TfLd + TfRd;
165 % total matrix element of spin down electron tunneling onto particle ...
166 % from both leads
167
168 Tf = Tfu + Tfd;
169 % total matrix element of both spin polarizations tunneling onto ...
170 % particle from leads
171
172 Tfua = TfLua + TfRua;
173 Tfda = TfLda + TfRda;
174 Tfa = Tfua + Tfda;
175 Tfp = Tfu + Tfd;
176 Tfaq = Tfua + Tfda;
177
178 gammaL = RR*RL/(RR+RL);
179 q = 1.6E-19; %electronic charge
180 ccoef = gammaL*q*1E12;
181 %coefficient of current in units of pico-amps
182
```

```
%now, loop over all times
for tind=2:length(mtime)
    h = hvals(tind);
    uL = uLvals(tind);
    uR = uRvals(tind);
    if hvals(tind)~= hvals(tind-1)
        hamilcellparam = {S0,S01,epsilon,epsilonz,theta_se,kappa,h,Sx, ...
            Sy,Sz,Sx1,Sy1,Sz1,Kzunianis,Kbiax};
        [V,D,V1,D1] = findhamilstates(hamilcellparam);
        hamiloutcell = {V,D,V1,D1};
        [TN2,TP2,T,SZS,SZS1,Ens,Ens1] = sortandCG(hamiloutcell, ...
            hamilcellparam);
        sortCGoutcell = {TN2,TP2,T,SZS,SZS1,Ens,Ens1};

        %Costates4_nos; indexeadd; CGpra_vectorized_pg;

        Ttu=TP2(1:2*S01+1,1:2*S0+1);
        Ttd=TN2(1:2*S01+1,1:2*S0+1);

        hnew=hvals(tind);
        hinit=hvals(tind-1);
        newstateprob = statechangedbv(stateprob,hinit,hnew,hamilcellparam);
        %         statechange_deltab_v;
        stateprob = newstateprob;
    end

    %define Fermi functions in left and right leads for bias
    %uL, uR

    Ensmat = repmat(Ens',[2*S01+1,1]);
    Ens1mat = repmat(Ens1,[1,2*S0+1]);

```

```
215     fL = 1./(1+exp((Ens1mat-Ensmat-uL)./ktemp));
216     fR = 1./(1+exp((Ens1mat-Ensmat-uR)./ktemp));
217
218
219     %             for j=1:2*S0+1
220     %                 for i=1:2*S01+1
221     %                     fL(i,j)=1/(exp((Ens1(i)-Ens(j)-uL)/ktemp)+1);
222     %                     fR(i,j)=1/(exp((Ens1(i)-Ens(j)-uR)/ktemp)+1);
223     %                 end
224     %             end
225
226     TfLu = RLu*times(Ttu,fL); %matrix element for tunneling on to ...
227     % particle from left lead, spin up
228     TfLd = RLd*times(Ttd,fL); %matrix element for tunneling on to ...
229     % particle from left lead, spin down
230     TfLua = RLu*times(Ttu,1-fL);%matrix element for tunneling off of ...
231     % particle into left lead, spin up
232     TfLda = RLd*times(Ttd,1-fL);%matrix element for tunneling off of ...
233     % particle into left lead, spin down
234
235     TfRu = RRu*times(Ttu,fR); %matrix element for tunneling on to ...
236     % particle from right lead, spin up
237     TfRd = RRd*times(Ttd,fR); %matrix element for tunneling on to ...
238     % particle from right lead, spin down
239     TfRua = RRu*times(Ttu, 1-fR); %matrix element for tunneling off of ...
240     % particle into right lead, spin up
241     TfRda = RRd*times(Ttd, 1-fR); %matrix element for tunneling off of ...
242     % particle into right lead, spin down
243
244     Tfu = TfLu + TfRu; % total matrix element of spin up electron ...
245     % tunneling onto particle from both leads
246     Tfd = TfLd + TfRd; % total matrix element of spin down electron ...
```

```
247     % tunneling onto particle from both leads
248     Tf = Tfu + Tfd;    % total matrix element of both spin polarizations ...
249     % tunneling onto particle from leads
250     Tfua = TfLua + TfRua;
251     Tfda = TfLda + TfRda;
252     Tfa = Tfua + Tfda;
253     Tfp = Tfu + Tfd;
254     Tfaq = Tfua + Tfda;
255
256     %generate probability distribution to determine if transition takes
257     %place.
258     if flagnp1
259         qmat = repmat(Q',[1,2*S0+1]);
260         Tfaq = tau*times(qmat,Tfa);
261         %for i=1:2*S0+1
262         %    Tfaq(:,i)=tau*times(Q',Tfa(:,i));
263         %end
264         pmat = repmat(P,[2*S01+1,1]);
265         %for i=1:2*S01+1
266         %    Tfp(i,:)=tau*times(P,Tf(i,:));
267         %end
268         Tfp = tau*times(pmat,Tf);
269
270         Tdiff=Tfaq-Tfp;
271         Tdiffp=-1*Tdiff';
272         dP=sum(Tdiff);
273         dQ=sum(Tdiffp);
274         stateprob =stateprob+[dP,dQ];
275         %         if tind==2
276         %             figure; plot(stateprob);
277         %         end
278         eventind = genrand(stateprob);
```

```
279         if eventind>2*S0+1
280             mvalue(tind) = mvalue(tind-1); %no transition case
281             currentvector(tind) = currentvector(tind-1);
282         else
283             P = zeros(1,2*S0+1);
284             Q = zeros(1,2*S01+1);
285             P(eventind) = 1;
286             flagnp1=false;
287             mvalue(tind) = P*SZS+Q*SZS1;
288
289
290             currentvector(tind) = sum((fL.*T)*P')+sum((fL.*T)'*Q');
291             %the above expression is a vectorized version of the following
292             %nested loops:
293
294 %                 for alpha = 1:length(Ens)
295 %                     for beta = 1:length(Ens1)
296 %                         currentvector(tind) = currentvector(tind)+ ...
297 % fL(beta,alpha)*T(beta,alpha)*P(alpha)+ ...
298 % fL(beta,alpha)'*T(beta,alpha)'*Q(beta);
299 %                     end
300 %                 end
301
302
303             stateprob = [P,Q];
304         end
305
306     else
307         qmat = repmat(Q',[1,2*S0+1]);
308         Tfaq = tau*times(qmat,Tfa);
309
310         pmat = repmat(P,[2*S01+1,1]);
```

```
311
312         Tfp = tau*times(pmat,Tf);
313         %                           qmat =
314         %                           %for i=1:2*S0+1
315         %                           %    Tfaq(:,i)=tau*times(Q',Tfa(:,i));
316         %                           %end
317         %                           pmat =
318         %                           %for i=1:2*S01+1
319         %                           %    Tfp(i,:)=tau*times(P,Tf(i,:));
320         %                           %end
321         Tdiff=Tfaq-Tfp;
322         Tdiffp=-1*Tdiff';
323         dP=sum(Tdiff);
324         dQ=sum(Tdiffp);
325         stateprob =stateprob+[dP,dQ];
326         eventind = genrand(stateprob);
327         if eventind<=2*S0+1
328             mvalue(tind) = mvalue(tind-1); %no transition case
329             currentvector(tind) = currentvector(tind-1);
330         else
331
332             P = zeros(1,2*S0+1);
333             Q = zeros(1,2*S01+1);
334             Q(eventind-(2*S0+1)) = 1;
335             flagnp1=true;
336             mvalue(tind) = P*SZS+Q*SZS1;
337
338
339             currentvector(tind) = sum((fL.*T)*P')+sum((fL.*T)'*Q');
340
341             stateprob = [P,Q];
342
```

```
343         end
344     end
345
346     %the following conditional expression keeps track of how much progress
347     %the simulation has made overall, as a percent.
348     if mod(tind,2000)==0
349         toc;
350         display([num2str(tind/length(mtime)*100) ...
351             ' percent done....']);
352     end
353
354 end
355
356 toc;
357
358 %convert the current into pA, rather than normalized units:
359 currentvector = currentvector*ccoef;
360
361 stochmasterspecout = {mvalue,currentvector,hvals,uLvals,uRvals,tvals};
362
363 %The commented code below can be used to save the data in different
364 %formats. In this new version of the code, the saving process takes place
365 %outside of this program, and is performed after the stochmasterspecout
366 %cell is returned.
367 %
368 %             time = clock;
369 %             savestrval = [num2str(time(1)) '_' num2str(time(2)) '_' ...
370 %                 num2str(time(3)) '_t' num2str(time(4)) '_' ...
371 %                 num2str(time(5))];
372 %
373 %             runnum = 1;
374 %             tre = true;
```

```
375 %
376 %             if ud==true
377 %                 strin = 'ud';
378 %             else
379 %                 strin='u';
380 %             end
381 %
382 %             while tre
383 %                 strtestforrun = [strin 'fig2_hyst_uRanduL_Test_' ...
384 %                     strinitstate 'PG_Mag_vs_time_SP_voltageswitching' ...
385 %                     '_H100alpha_PSL_' num2str(PSL) '_PSR_' num2str(PSR) ...
386 %                     'umin_' num2str(umin/1000) '_umax_' ...
387 %                     num2str(umax/1000) 'meV_temp_' num2str(ktemp/86) ...
388 %                     'K_run_' num2str(runnum) '.mat'];
389 %
390 %                 if exist(strtestforrun,'file')
391 %                     display(num2str(runnum));
392 %                     runnum = runnum+1;
393 %                 else
394 %                     tre=false;
395 %                 end
396 %             end
397 %             save([strin 'fig2_hyst_uRanduL_Test_' strinitstate ...
398 %                 'PG_Mag_vs_time_SP_voltageswitching_H100alpha_PSL_' ...
399 %                 num2str(PSL) '_PSR_' num2str(PSR) 'umin_' ...
400 %                 num2str(umin/1000) '_umax_' num2str(umax/1000) ...
401 %                 'meV_temp_' num2str(ktemp/86) 'K_run_' num2str(runnum) ...
402 %                 '.mat'],'mvalue','mtime','tau','uL','currentvector', ...
403 %                 'hvals','RR','RL','uR','epsilon','epsilonz','theta_se', ...
404 %                 'ktemp','PSL','PSR','runnum');
405
406
```

```
407 end
```

REFERENCES

[1] Adam, S., Kindermann, M., Rahav, S., and Brouwer, P. W., "Mesoscopic anisotropic magnetoconductance fluctuations in ferromagnets," *Phys. Rev. B*, vol. 73, 2006.

[2] Adam, S., Polianski, M. L., Waintal, X., and Brouwer, P. W., "Magnetic-field dependence of energy levels in ultrasmall metal grains," *Phys. Rev. B*, vol. 66, p. 195412, 2002.

[3] Aleiner, I., Brouwer, P., and Glazman, L., "Quantum effects in coulomb blockade," *Physics Reports*, vol. 358, no. 56, pp. 309 – 440, 2002.

[4] Alhassid, Y., "The statistical theory of quantum dots," *Reviews of Modern Physics*, vol. 72, no. 4, p. 895, 2000.

[5] Anaya, A., Bowman, M., and Davidović, D., "Suppression of spin-orbit scattering in strong-disordered gold nanojunctions," *Phys. Rev. Lett.*, vol. 93, p. 246604, 2004.

[6] Anaya, A., Korotkov, A. L., Bowman, M., Waddell, J., and Davidović, D., "Nanometer-scale metallic grains connected with atomic-scale conductors," *Journal of Applied Physics*, vol. 93, p. 3501, 2003.

[7] Aradhya, S. V. and Venkataraman, L., "Single-molecule junctions beyond electronic transport," *Nature nanotechnology*, vol. 8, no. 6, pp. 399–410, 2013.

[8] Ashoori, R. C., "Electrons in artificial atoms," *Nature*, vol. 379, p. 413, 1996.

[9] Averin, D. V. and Korotkov, A. N., "Correlated single-electron tunneling via mesoscopic metal particles - effects of the energy quantization," *Journal of low temperature physics*, vol. 80, p. 173, 1990.

[10] Averin, D. V., Korotkov, A. N., and Likharev, K. K., "Theory of single-electron charging of quantum wells and dots," *Phys. Rev. B*, vol. 44, p. 6199, 1999.

[11] Baadji, N., Piacenza, M., Tugsuz, T., Della Sala, F., Maruccio, G., and Sanvito, S., "Electrostatic spin crossover effect in polar magnetic molecules," *Nature materials*, vol. 8, no. 10, pp. 813–817, 2009.

[12] Baibich, M. N., Broto, J. M., Fert, A., Van Dau, F. N., Petroff, F., Etienne, P., Creuzet, G., Friederich, A., and Chazelas, J., "Giant magnetoresistance of (001)fe/(001)cr magnetic superlattices," *Phys. Rev. Lett.*, vol. 61, pp. 2472–2475, 1988.

[13] Baranger, H. U., Ullmo, D., and Glazman, L. I., "Interactions and interference in quantum dots: kinks in coulomb-blockade peak positions," *Phys. Rev. B*, vol. 61, pp. R2425–R2428, Jan 2000.

[14] Barnas, J. and Fert, A., "Effects of spin accumulation on single-electron tunneling in a double ferromagnetic microjunction," *Europhysics letters*, vol. 44, p. 85, 1998.

[15] Barnas, J. and Fert, A., "Magnetoresistance oscillations due to charging effects in double ferromagnetic tunnel junctions," *Phys. Rev. Lett.*, vol. 80, p. 1058, 1998.

[16] Barnas, J. and Fert, A., "Interplay of spin-accumulation and coulomb blockade in double ferromagnetic junctions," *J. Magn. Magn. Matter.*, vol. 192, p. 391, 1999.

[17] Barnas, J., Martinek, J., Michalek, G., Bulka, B. R., and Fert, A., "Spin effects in ferromagnetic single-electron transistors," *Phys. Rev. B*, vol. 62, p. 12363, 2000.

[18] Bass, J. and Pratt Jr, W. P., "Spin-diffusion lengths in metals and alloys, and spin-flipping at metal/metal interfaces: an experimentalist's critical review," *Journal of Physics: Condensed Matter*, vol. 19, no. 18, p. 183201, 2007.

[19] Beenakker, C. W. J., "Theory of coulomb-blockade oscillations in the conductance of a quantum dot," *Phys. Rev. B*, vol. 44, p. 1646, 1991.

[20] Berger, L., "Emission of spin waves by a magnetic multilayer traversed by a current," *Phys. Rev. B*, vol. 54, pp. 9353–9358, 1996.

[21] Birk, F. T. and Davidović, D., "Magnetoresistance in an aluminum nanoparticle with a single ferromagnetic contact," *Phys. Rev. B*, vol. 81, p. 241402, 2010.

[22] Birk, F. T., Malec, C. E., and Davidović, D., "Spin-polarized electron tunneling through an aluminum particle in a noncollinear magnetic field," *Phys. Rev. B*, vol. 79, p. 245425, 2009.

[23] Black, C. T., Ralph, D. C., and Tinkham, M., "Spectroscopy of the superconducting gap in individual nanometer-scale aluminum particles," *Phys. Rev. Lett.*, vol. 76, p. 688, 1996.

[24] Bogani, L. and Wernsdorfer, W., "Molecular spintronics using single-molecule magnets," *Nature Materials*, vol. 7, p. 179, 2008.

[25] Bonet, E., Deshmukh, M. M., and Ralph, D. C., "Solving rate equations for electron tunneling via discrete quantum states," *Phys. Rev. B*, vol. 65, p. 045317, 2002.

[26] Bowman, M., Anaya, A., Korotkov, A. L., and Davidović, D., "Localization and capacitance fluctuations in disordered au nano-junctions," *Phys. Rev. B*, vol. 69, p. 205405, 2004.

[27] Brataas, A., Nazarov, Y. V., Inoue, J., and Bauer, G. E. W., "Non-equilibrium spin accumulation in ferromagnetic single-electron transistors," *European physical journal B*, vol. 9, p. 421, 1999.

[28] Brataas, A., Nazarov, Y. V., Inoue, J., and Bauer, G. E. W., "Spin accumulation in small ferromagnetic double-barrier junctions," *Phys. Rev. B*, vol. 59, p. 93, 1999.

[29] Brataas, A. and Wang, X. H., "Linear response conductance and magnetoresistance of ferromagnetic single electron transistors," *Phys. Rev. B*, vol. 64, p. 104434, 2001.

[30] Brewer, G., *Electron-beam technology in microelectronic fabrication*. Elsevier, 2012.

[31] Brouwer, P. W., Waintal, X., and Halperin, B. I., "Fluctuating spin g-tensor in small metal grains," *Phys. Rev. Lett.*, vol. 85, p. 369, 2000.

[32] Brown, W. F., "Thermal fluctuations of a single-domain particle," *Phys. Rev.*, vol. 130, pp. 1677–1686, 1963.

[33] Bryant, B., Spinelli, A., Wagenaar, J. J. T., Gerrits, M., and Otte, A. F., "Local control of single atom magnetocrystalline anisotropy," *Phys. Rev. Lett.*, vol. 111, p. 127203, Sep 2013.

[34] Burzurí, E., Zyazin, A. S., Cornia, A., and van der Zant, H. S. J., "Direct observation of magnetic anisotropy in an individual fe4 single-molecule magnet," *Phys. Rev. Lett.*, vol. 109, p. 147203, Oct 2012.

[35] Canali, C. M. and MacDonald, A. H., "Theory of tunneling spectroscopy in ferromagnetic nanoparticles," *Phys. Rev. Lett.*, vol. 85, p. 5623, 2000.

[36] Cehovin, A., Canali, C. M., and MacDonald, A. H., "Magnetization orientation dependence of the quasiparticle spectrum and hysteresis in ferromagnetic metal nanoparticles," *Phys. Rev. B*, vol. 66, p. 094430, Sep 2002.

[37] Cehovin, A., Canali, C. M., and MacDonald, A. H., "Elementary excitations of ferromagnetic metal nanoparticles," *Phys. Rev. B*, vol. 68, p. 014423, Jul 2003.

[38] Cehovin, A., Canali, C. M., and MacDonald, A. H., "Orbital and spin contributions to the g tensors in metal nanoparticles," *Phys. Rev. B*, vol. 69, p. 045411, Jan 2004.

[39] Davidović, D. and Tinkham, M., "Spectroscopy, interactions, and level splittings in an nanoparticles," *Phys. Rev. Lett.*, vol. 83, pp. 1644–1647, 1999.

[40] Deshmukh, M. M., E, E. B., Pasupathy, A. N., and Ralph, D. C., "Equilibrium and nonequilibrium electron tunneling via discrete quantum states," *Phys. Rev. B*, vol. 65, p. 073301, 2002.

[41] Deshmukh, M. M., Kleff, S., Gueron, S., Bonet, E., Pasupathy, A. N., von Delft, J., and Ralph, D. C., "Magnetic anisotropy variations and nonequilibrium tunneling in a cobalt nanoparticle," *Phys. Rev. Lett*, vol. 87, p. 226801, 2001.

[42] Deshmukh, M. M. and Ralph, D. C., "Using single quantum states as spin filters to study spin polarization in ferromagnets," *Phys. Rev. Lett*, vol. 89, p. 266803, 2002.

[43] Dorantes-Dávila, J. and Pastor, G. M., "Magnetic anisotropy of one-dimensional nanostructures of transition metals," *Phys. Rev. Lett.*, vol. 81, pp. 208–211, Jul 1998.

[44] Dyakonov, M. and Perel, V., "Current-induced spin orientation of electrons in semiconductors," *Physics Letters A*, vol. 35, no. 6, pp. 459–460, 1971.

[45] Elliot, R. J., "Theory of the effect of spin-orbit coupling on magnetic resonance in some semiconductors," *Phys. Rev.*, vol. 96, p. 266, 1954.

[46] Elste, F. and Timm, C., "Transport through anisotropic magnetic molecules with partially ferromagnetic leads: Spin-charge conversion and negative differential conductance," *Phys. Rev. B*, vol. 73, p. 235305, 2006.

[47] Fert, A., "Nobel lecture: Origin, development, and future of spintronics*," *Rev. Mod. Phys.*, vol. 80, pp. 1517–1530, Dec 2008.

[48] Friedel, J., Lenglart, P., and Leman, G., "Etude du couplage spin-orbite dans les metaux de transition. application au platine," *Journal of Physics and Chemistry of Solids*, vol. 25, no. 8, pp. 781–800, 1964.

[49] Friedman, J. R., Sarachik, M. P., Tejada, J., and Ziolo, R., "Macroscopic measurement of resonant magnetization tunneling in high-spin molecules," *Phys. Rev. Lett.*, vol. 76, p. 3830, 1996.

[50] Gartland, P., Birk, F. T., Jiang, W., and Davidović, D., "Giant electron-spin g factors in a ferromagnetic nanoparticle," *Phys. Rev. B*, vol. 88, p. 075303, Aug 2013.

[51] Gartland, P., Jiang, W., and Davidović, D., "Voltage control of magnetic hysteresis in a nickel nanoparticle," *Phys. Rev. B*, vol. 91, p. 235408, Jun 2015.

[52] Gatteschi, D. and Sessoli, R., "Quantum tunneling of magnetization and related phenomena in molecular materials," *Angewandte Chemie International Edition*, vol. 42, no. 3, pp. 268–297, 2003.

[53] Geim, A. K. and Novoselov, K. S., "The rise of graphene," *Nature materials*, vol. 6, no. 3, pp. 183–191, 2007.

[54] Gorokhov, D. A. and Brouwer, P. W., "Electron correlations in metal nanoparticles with spin-orbit scattering," *arXiv preprint cond-mat/0311086*, 2003.

[55] Gorokhov, D. A. and Brouwer, P. W., "Fluctuations of g factors in metal nanoparticles: Effects of electron-electron interaction and spin-orbit scattering," *Phys. Rev. Lett.*, vol. 91, p. 186602, Oct 2003.

[56] Gorokhov, D. A. and Brouwer, P. W., "Combined effect of electron-electron interactions and spin-orbit scattering in metal nanoparticles," *Phys. Rev. B*, vol. 69, p. 155417, Apr 2004.

[57] Grünberg, P., Schreiber, R., Pang, Y., Brodsky, M. B., and Sowers, H., "Layered magnetic structures: Evidence for antiferromagnetic coupling of fe layers across cr interlayers," *Phys. Rev. Lett.*, vol. 57, p. 2442, 1986.

[58] Gueron, S., Deshmukh, M. M., Myers, E. B., and Ralph, D. C., "Tunneling via individual electronic states in ferromagnetic nanoparticles," *Phys. Rev. Lett.*, vol. 83, p. 4148, 1999.

[59] Halperin, W. P., "Quantum size effects in metal particles," *Rev. Mod. Phys.*, vol. 58, p. 533, 1986.

[60] Hänggi, P., Talkner, P., and Borkovec, M., "Reaction-rate theory: fifty years after kramers," *Reviews of Modern Physics*, vol. 62, no. 2, p. 251, 1990.

[61] Hanson, R., Witkamp, B., Vandersypen, L. M. K., van Beveren, L. H. W., Elzerman, J. M., and Kouwenhoven, L. P., "Zeeman energy and spin relaxation in a one-electron quantum dot," *Phys. Rev. Lett.*, vol. 91, p. 196802, Nov 2003.

[62] Heersche, H. B., de Groot, Z., Folk, J. A., van der Zant, H. S. J., Romeike, C., Wegewijs, M. R., Zobbi, L., Barreca, D., Tondello, E., and Cornia, A., "Electron transport through single mn12 molecular magnets," *Phys. Rev. Lett.*, vol. 96, p. 206801, May 2006.

[63] Heinrich, A. J., Gupta, J. A., Lutz, C. P., and Eigler, D. M., "Single-atom spin-flip spectroscopy," *Science*, vol. 306, no. 5695, pp. 466–469, 2004.

[64] Heinze, S., Bode, M., Kubetzka, A., Pietzsch, O., Nie, X., Blgel, S., and Wiesendanger, R., "Real-space imaging of two-dimensional antiferromagnetism on the atomic scale," *Science*, vol. 288, no. 5472, pp. 1805–1808, 2000.

[65] Herzog, G., Krause, S., and Wiesendanger, R., "Heat assisted spin torque switching of quasistable nanomagnets across a vacuum gap," *Applied Physics Letters*, vol. 96, no. 10, pp. –, 2010.

[66] Hirjibehedin, C. F., Lin, C.-Y., Otte, A. F., Ternes, M., Lutz, C. P., Jones, B. A., and Heinrich, A. J., "Large magnetic anisotropy of a single atomic spin embedded in a surface molecular network," *Science*, vol. 317, no. 5842, pp. 1199–1203, 2007.

[67] Hirjibehedin, C. F., Lutz, C. P., and Heinrich, A. J., "Spin coupling in engineered atomic structures," *Science*, vol. 312, no. 5776, pp. 1021–1024, 2006.

[68] Hüttel, A., Qin, H., Holleitner, A., Blick, R., Neumaier, K., Weinmann, D., Eberl, K., and Kotthaus, J., "Spin blockade in ground-state

resonance of a quantum dot," *EPL (Europhysics Letters)*, vol. 62, no. 5, p. 712, 2003.

[69] Žutić, I., Fabian, J., and Das Sarma, S., "Spintronics: Fundamentals and applications," *Rev. Mod. Phys.*, vol. 76, pp. 323–410, 2004.

[70] Jamet, M., Wernsdorfer, W., Thirion, C., Mailly, D., Dupuis, V., Méinon, P., and Pérez, A., "Magnetization reversal of a 1000-atoms cobalt cluster," *Journal of Magnetism and Magnetic Materials*, vol. 226-230, pp. 1833 – 1834, 2001.

[71] Jamet, M., Wernsdorfer, W., Thirion, C., Mailly, D., Dupuis, V., Mélinon, P., and Pérez, A., "Magnetic anisotropy of a single cobalt nanocluster," *Phys. Rev. Lett.*, vol. 86, pp. 4676–4679, May 2001.

[72] Jamet, M., Wernsdorfer, W., Thirion, C., Dupuis, V., Mélinon, P., Pérez, A., and Mailly, D., "Magnetic anisotropy in single clusters," *Phys. Rev. B*, vol. 69, p. 024401, 2004.

[73] Jiang, W., G. P. and Davidović, D., "Size-dependence of magneto-electronic coupling in co nanoparticles," *Journal of Applied Physics*, vol. 113, no. 22, pp. –, 2013.

[74] Jiang, W., Birk, F. T., and Davidovic, D., "Effects of confinement and electron transport on magnetic switching in single co nanoparticles," *Sci. Rep.*, vol. 3, p. 1200, 2013.

[75] Jiang, W., Birk, F. T., and Davidovic, D., "Microwave coupled electron tunneling measurement of co nanoparticles," *Appl. Phys. Lett.*, vol. 99, p. 032510, 2011.

[76] Jo, M.-H., Grose, J. E., Baheti, K., Deshmukh, M. M., Sokol, J. J., Rumberger, E. M., Hendrickson, D. N., Long, J. R., Park, H., and Ralph, D. C., "Signatures of molecular magnetism in single-molecule transport spectroscopy," *Nano Letters*, vol. 6, pp. 2014–2020, 2006.

[77] Johnson, G. E., "Constructions of particular random processes," *Proceedings of the IEEE*, vol. 82, no. 2, pp. 270–285, 1994.

[78] Johnson, M. and Silsbee, R. H., "Interfacial charge-spin coupling: injection and detection of spin magnetization in metals.," *Phys. Rev. Lett.*, vol. 55, p. 1790, 1985.

[79] Kane, C. L. and Mele, E. J., "Z 2 topological order and the quantum spin hall effect," *Physical review letters*, vol. 95, no. 14, p. 146802, 2005.

[80] Kastner, M. A., "Artificial atoms," *Physics Today*, vol. 46, no. 1, pp. 24–31, 1993.

[81] Katine, J. A., Albert, F. J., Buhrman, R. A., Myers, E. B., and Ralph, D. C., "Current-driven magnetization reversal and spin-wave excitations in co /cu /co pillars," *Phys. Rev. Lett.*, vol. 84, p. 3149, 2000.

[82] Katine, J. and Fullerton, E. E., "Device implications of spin-transfer torques," *Journal of Magnetism and Magnetic Materials*, vol. 320, no. 7, pp. 1217–1226, 2008.

[83] Katine, J. and Fullerton, E. E., "Device implications of spin-transfer torques," *Journal of Magnetism and Magnetic Materials*, vol. 320, no. 7, pp. 1217–1226, 2008.

[84] Khajetoorians, A. A., Schlenk, T., Schweflinghaus, B., dos Santos Dias, M., Steinbrecher, M., Bouhassoune, M., Lounis, S., Wiebe,

J., and Wiesendanger, R., "Spin excitations of individual fe atoms on pt(111): Impact of the site-dependent giant substrate polarization," *Phys. Rev. Lett.*, vol. 111, p. 157204, Oct 2013.

[85] Khajetoorians, A. A., Baxevanis, B., Hbner, C., Schlenk, T., Krause, S., Wehling, T. O., Lounis, S., Lichtenstein, A., Pfannkuche, D., Wiebe, J., and Wiesendanger, R., "Current-driven spin dynamics of artificially constructed quantum magnets," *Science*, vol. 339, no. 6115, pp. 55–59, 2013.

[86] Khajetoorians, A. A., Wiebe, J., Chilian, B., Lounis, S., Blügel, S., and Wiesendanger, R., "Atom-by-atom engineering and magnetometry of tailored nanomagnets," *Nature Physics*, vol. 8, no. 6, pp. 497–503, 2012.

[87] Khajetoorians, A. A., Wiebe, J., Chilian, B., and Wiesendanger, R., "Realizing all-spinbased logic operations atom by atom," *Science*, vol. 332, no. 6033, pp. 1062–1064, 2011.

[88] King, P., Hatch, R. C., Bianchi, M., Ovsyannikov, R., Lupulescu, C., Landolt, G., Slomski, B., Dil, J., Guan, D., Mi, J., and others, "Large tunable rashba spin splitting of a two-dimensional electron gas in bi 2 se 3," *Physical review letters*, vol. 107, no. 9, p. 096802, 2011.

[89] Kleff, S., Delft, J. v., Deshmukh, M. M., and Ralph, D. C., "Model for ferromagnetic nanograins with discrete electronic states," *Phys. Rev. B*, vol. 64, p. 220401, 2001.

[90] Kleff, S. and von Delft, J., "Nonequilibrium excitations in ferromagnetic nanoparticles," *Phys. Rev. B*, vol. 65, p. 214421, Jun 2002.

[91] Kogan, A., Granger, G., Kastner, M. A., Goldhaber-Gordon, D., and Shtrikman, H., "Singlet˘triplet transition in a single-electron transistor at zero magnetic field," *Phys. Rev. B*, vol. 67, p. 113309, Mar 2003.

[92] Koppens, F. H. L., Buizert, C., Tielrooij, K. J., Vink, I. T., Nowack, K. C., Meunier, T., Kouwenhoven, L. P., and Vandersypen, L. M. K., "Driven coherent oscillations of a single electron spin in a quantum dot," *Nature*, vol. 442, pp. 766–771, 2006.

[93] Kouwenhoven, L. P., Marcus, C. M., McEuen, P. L., Tarucha, S., Westervelt, R. M., and Wingreen, N. S., "Electron transport in quantum dots," in *Mesoscopic electron transport*, pp. 105–214, Springer, 1997.

[94] Krause, S., Herzog, G., Stapelfeldt, T., Berbil-Bautista, L., Bode, M., Vedmedenko, E. Y., and Wiesendanger, R., "Magnetization reversal of nanoscale islands: How size and shape affect the arrhenius prefactor," *Phys. Rev. Lett.*, vol. 103, p. 127202, Sep 2009.

[95] Liu, R. S., Michalak, L., Canali, C. M., Samuelson, L., and Pettersson, H., "Tunneling anisotropic magnetoresistance in co/alox/au tunnel junctions," *Nano Letters*, vol. 8, no. 3, pp. 848–852, 2008.

[96] Liu, W., *Fundamentals of III-V Devices: HBTs, MESFETs, and HFETs/HEMTs*. Wiley, 1999.

[97] Loth, S., Baumann, S., Lutz, C. P., Eigler, D. M., and Heinrich, A. J., "Bistability in atomic-scale antiferromagnets," *SCIENCE*, vol. 335, pp. 196–199, JAN 13 2012.

[98] Loth, S., Etzkorn, M., Lutz, C. P., Eigler, D. M., and Heinrich, A. J., "Measurement of fast electron spin relaxation times with atomic resolution," *Science*, vol. 329, no. 5999, pp. 1628–1630, 2010.

[99] MacDonald, A. and Canali, C., "Quantum description of ferromagnet metal nanoparticles," *Solid State Communications*, vol. 119, no. 45, pp. 253 – 258, 2001.

[100] Marcus, C., Patel, S., Huibers, A., Cronenwett, S., Switkes, M., Chan, I., Clarke, R., Folk, J., Godijn, S., Campman, K., and others, "Quantum chaos in open versus closed quantum dots: Signatures of interacting particles," *Chaos, Solitons & Fractals*, vol. 8, no. 7, pp. 1261–1279, 1997.

[101] Mattis, D. C., *The theory of magnetism made simple*. World Scientific, 2006.

[102] Matveev, K. A., Glazman, L. I., and Larkin, A. I., "g-factors of discrete levels in nanoparticles," *Phys. Rev. Lett.*, vol. 85, p. 2789, 2000.

[103] Michalak, L., Canali, C. M., and Benza, V. G., "Electron-magnon coupling and nonlinear tunneling transport in magnetic nanoparticles," *Phys. Rev. Lett.*, vol. 97, p. 096804, 2006.

[104] Miyamachi, T., Gruber, M., Davesne, V., Bowen, M., Boukari, S., Joly, L., Scheurer, F., Rogez, G., Yamada, T. K., Ohresser, P., and others, "Robust spin crossover and memristance across a single molecule," *Nature communications*, vol. 3, p. 938, 2012.

[105] Nadj-Perge, S., Pribiag, V. S., van den Berg, J. W. G., Zuo, K., Plissard, S. R., Bakkers, E. P. A. M., Frolov, S. M., and Kouwenhoven, L. P., "Spectroscopy of spin-orbit quantum bits in indium antimonide nanowires," *Phys. Rev. Lett.*, vol. 108, p. 166801, Apr 2012.

[106] Néel, L., "Théorie du traînage magnétique des ferromagnétiques en grains fins avec applications aux terres cuites," *Ann. Géophys*, vol. 5, p. 99, 1949.

[107] Neto, A. C., Guinea, F., Peres, N., Novoselov, K. S., and Geim, A. K., "The electronic properties of graphene," *Reviews of modern physics*, vol. 81, no. 1, p. 109, 2009.

[108] Nilsson, H. A., Caroff, P., Thelander, C., Larsson, M., Wagner, J. B., Wernersson, L.-E., Samuelson, L., and Xu, H. Q., "Giant, level-dependent g factors in insb nanowire quantum dots," *Nano Letters*, vol. 9, no. 9, pp. 3151–3156, 2009. PMID: 19736971.

[109] Ono, K., Shimada, H., Kobayashi, S., and Outuka, Y., "Magnetoresistance of ni/nio/co small tunnel junctions in coulomb blockade regime," *Journal of the physical society of Japan*, vol. 65, p. 3449, 1996.

[110] Osorio, E., Bjørnholm, T., Lehn, J., Ruben, M., and Van Der Zant, H., "Single-molecule transport in three-terminal devices," *Journal of Physics: Condensed Matter*, vol. 20, no. 37, p. 374121, 2008.

[111] Osorio, E. A., Moth-Poulsen, K., van der Zant, H. S., Paaske, J., Hedegård, P., Flensberg, K., Bendix, J., and Bjørnholm, T., "Electrical manipulation of spin states in a single electrostatically gated transition-metal complex," *Nano letters*, vol. 10, no. 1, pp. 105–110, 2009.

[112] Otte, A. F., Ternes, M., Loth, S., Lutz, C. P., Hirjibehedin, C. F., and Heinrich, A. J., "Spin excitations of a kondo-screened atom coupled to a second magnetic atom," *Phys. Rev. Lett.*, vol. 103, p. 107203, Sep 2009.

[113] Pankhurst, Q. A., Connolly, J., Jones, S., and Dobson, J., "Applications of magnetic nanoparticles in biomedicine," *Journal of physics D: Applied physics*, vol. 36, no. 13, p. R167, 2003.

[114] Papaconstantopoulos, D., *Handbook of the band structure of elemental solids*. Plenum Press New York, 1986.

[115] Petta, J. R., Johnson, A. C., Taylor, J. M., Laird, E. A., A, A. Y., Lukin, M. D., Marcus, C. M., Hanson, M. P., and Gossard, A. C., "Coherent manipulation of coupled electron spins in semiconductor quantum dots," *Science*, vol. 309, pp. 2180–2184, 2004.

[116] Petta, J. R. and Ralph, D. C., "Studies of spin-orbit scattering in noble-metal nanoparticles using energy-level tunneling spectroscopy," *Phys. Rev. Lett.*, vol. 87, p. 266801, 2001.

[117] Radisavljevic, B., Radenovic, A., Brivio, J., Giacometti, V., and Kis, A., "Single-layer mos2 transistors," *Nature nanotechnology*, vol. 6, no. 3, pp. 147–150, 2011.

[118] Ralph, D. C., Black, C. T., and Tinkham, M., "Spectroscopic measurements of discrete electronic states in single metal particles," *Phys. Rev. Lett.*, vol. 74, p. 3241, 1995.

[119] Ralph, D. C., Black, C. T., and Tinkham, M., "Gate-voltage studies of discrete electronic states in aluminum nanoparticles," *Phys. Rev. Lett.*, vol. 78, p. 4087, 1997.

[120] Ralph, D. and Stiles, M. D., "Spin transfer torques," *Journal of Magnetism and Magnetic Materials*, vol. 320, no. 7, pp. 1190–1216, 2008.

[121] Rokhinson, L. P., Guo, L. J., Chou, S. Y., and Tsui, D. C., "Spin transitions in a small si quantum dot," *Phys. Rev. B*, vol. 63, p. 035321, Jan 2001.

[122] Romming, N., Hanneken, C., Menzel, M., Bickel, J. E., Wolter, B., von Bergmann, K., Kubetzka, A., and Wiesendanger, R., "Writing and deleting single magnetic skyrmions," *Science*, vol. 341, no. 6146, pp. 636–639, 2013.

[123] Romming, N., Kubetzka, A., Hanneken, C., von Bergmann, K., and Wiesendanger, R., "Field-dependent size and shape of single magnetic skyrmions," *Phys. Rev. Lett.*, vol. 114, p. 177203, May 2015.

[124] Sakurai, J. J. and Napolitano, J. J., *Modern quantum mechanics*. Pearson Higher Ed, 2014.

[125] Salinas, D. G., Gueron, S., Ralph, D. C., Black, C. T., and Tinkham, M., "Effects of spin-orbit interactions on tunneling via discrete energy levels in metal nanoparticles," *Phys. Rev. B*, vol. 60, p. 6137, 1999.

[126] Sanvito, S. and Rocha, A., "Molecular-spintronics: The art of driving spin through molecules," *Journal of Computational and Theoretical Nanoscience*, vol. 3, pp. 624–642, 2006.

[127] Sanvito, S., "Molecular spintronics," *Chemical Society Reviews*, vol. 40, no. 6, pp. 3336–3355, 2011.

[128] Schroer, M. D., Petersson, K. D., Jung, M., and Petta, J. R., "Field tuning the g factor in inas nanowire double quantum dots," *Phys. Rev. Lett.*, vol. 107, p. 176811, Oct 2011.

[129] Sessoli, R., Gatteschi, D., Caneschi, A., and Novak, M., "Magnetic bistability in a metal-ion cluster," *NATURE*, vol. 365, pp. 141–143, SEP 9 1993.

[130] Shaji, N., Simmons, C. B., Thalakulam, M., Klein, L. J., Qin, H., Luo, H., Savage, D. E., Lagally, M. G., Rimberg, A. J., Joynt, R., Friesen, M., Blick, R. H., Coppersmith, S. N., and Eriksson, M. A., "Spin blockade and lifetime-enhanced transport in a few-electron si/sige double quantum dot," *Nature Physics*, vol. 4, pp. 540–544, 2008.

[131] Skomski, R., "Nanomagnetics," *Journal of Physics: Condensed Matter*, vol. 15, no. 20, p. R841, 2003.

[132] Skomski, R., Kirby, R. D., and Sellmyer, D. J., "Activation entropy, activation energy, and magnetic viscosity," *Journal of applied physics*, vol. 85, no. 8, pp. 5069–5071, 1999.

[133] Skumryev, V., Stoyanov, S., Zhang, Y., Hadjipanayis, G., Givord, D., and Nogues, J., "Beating the superparamagnetic limit with exchange bias," *Nature*, vol. 423, pp. 850–853, 2003.

[134] Slonczewski, J. C., "Conductance and exchange coupling of two ferromagnets separated by a tunneling barrier," *Phys. Rev. B*, vol. 39, p. 6995, 1989.

[135] Slonczewski, J. C., "Current-driven excitation of magnetic multilayers," *Journal of Magnetism and Manetic Materials*, vol. 159, pp. L1–L7, 1996.

[136] Stiles, M., Xiao, J., and Zangwill, A., "Phenomenological theory of current-induced magnetization precession," *Physical Review B*, vol. 69, no. 5, p. 054408, 2004.

[137] Stoner, E. C. and Wohlfarth, E., "A mechanism of magnetic hysteresis in heterogeneous alloys," *Philosophical Transactions of the Royal Society of London A: Mathematical, Physical and Engineering Sciences*, vol. 240, no. 826, pp. 599–642, 1948.

[138] Sun, J. Z., "Spin-current interaction with a monodomain magnetic body: A model study," *Phys. Rev. B*, vol. 62, pp. 570–578, Jul 2000.

[139] Sun, J. and Ralph, D., "Magnetoresistance and spin-transfer torque in magnetic tunnel junctions," *Journal of Magnetism and Magnetic Materials*, vol. 320, no. 7, pp. 1227–1237, 2008.

[140] Tamion, A., Raufast, C., Orozco, E. B., Dupuis, V., Fournier, T., Crozes, T., Bernstein, E., and Wernsdorfer, W., "Magnetization reversal of a single cobalt cluster using a rf field pulse," *J. Magn. Magn. Mater.*, vol. 322, p. 1315, 2010.

[141] Tarucha, S., Austing, D. G., Tokura, Y., van der Wiel, W. G., and Kouwenhoven, L. P., "Direct coulomb and exchange interaction in artificial atoms," *Phys. Rev. Lett.*, vol. 84, pp. 2485–2488, Mar 2000.

[142] Thirion, C., Wernsdorfer, W., and Mailly, D., "Switching of magnetization by nonlinear resonance studied in single nanoparticles," *Nature Mater.*, vol. 2, p. 524, 2003.

[143] Thomas, L., Lionti, F., Ballou, R., Gatteschi, D., Sessoli, R., and Barbara, B., "Macroscopic quantum tunnelling of magnetization in a single crystal of nanomagnets," *Nature*, vol. 383, p. 145, 1996.

[144] Timm, C., "Tunneling through magnetic molecules with arbitrary angle between easy axis and magnetic field," *Phys. Rev. B*, vol. 76, p. 014421, Jul 2007.

[145] Timm, C. and Elste, F., "Spin amplification, reading, and writing in transport through anisotropic magnetic molecules," *Phys. Rev. B*, vol. 73, p. 235304, Jun 2006.

[146] Tuominen, M. T., Hergenrother, J. M., Tighe, T. S., and Tinkham, M., "Experimental evidence for parity-based 2e periodicity in a superconducting single-electron tunneling transistor," *Phys. Rev. Lett.*, vol. 69, pp. 1997–2000, Sep 1992.

[147] Waintal, X. and Brouwer, P. W., "Tunable magnetic relaxation mechanism in magnetic nanoparticles," *Phys. Rev. Lett.*, vol. 91, p. 247201, 2003.

[148] Wang, Q. H., Kalantar-Zadeh, K., Kis, A., Coleman, J. N., and Strano, M. S., "Electronics and optoelectronics of two-dimensional transition metal dichalcogenides," *Nature nanotechnology*, vol. 7, no. 11, pp. 699–712, 2012.

[149] Wang, Y. and Sham, L., "Quantum approach of mesoscopic magnet dynamics with spin transfer torque," *Physical Review B*, vol. 87, no. 17, p. 174433, 2013.

[150] Wei, Y. G., Liu, X. Y., Zhang, L. Y., and Davidovic, D., "Mesoscopic resistance fluctuations in cobalt nanoparticles," *Phys. Rev. Lett.*, vol. 96, p. 146803, 2006.

[151] Wei, Y. G., Malec, C. E., and Davidovic, D., "Modeling electron-spin accumulation in a metallic nanoparticle," *Phys. Rev. B*, vol. 78, p. 035435, 2008.

[152] Wernsdorfer, W., Orozco, E. B., Hasselbach, K., Benoit, A., Barbara, B., Demoncy, N., Loiseau, A., Pascard, H., and Mailly, D., "Experimental evidence of the néel-brown model of magnetization reversal," *Phys. Rev. Lett.*, vol. 78, pp. 1791–1794, 1997.

[153] Wiesendanger, R., "Spin mapping at the nanoscale and atomic scale," *Rev. Mod. Phys.*, vol. 81, pp. 1495–1550, Nov 2009.

[154] Wolf, E. L., *Principles of Electron Tunneling Spectroscopy*. Oxford University Press, 1989.

[155] Wolf, S. A., Awschalom, D. D., Buhrman, R. A., Daughton, J. M., von Molnar, S., Roukes, M. L., Chtchelkanova, A. Y., and Treger, D. M., "Spintronics: A spin-based electronics vision for the future," *Science*, vol. 294, p. 1488, 2001.

[156] Wolter, B., Yoshida, Y., Kubetzka, A., Hla, S.-W., von Bergmann, K., and Wiesendanger, R., "Spin friction observed on the atomic scale," *Phys. Rev. Lett.*, vol. 109, p. 116102, Sep 2012.

[157] Wu, B. and Kumar, A., "Extreme ultraviolet lithography and three dimensional integrated circuita review," *Applied Physics Reviews*, vol. 1, no. 1, p. 011104, 2014.

[158] Xiao, J., Bauer, G. E., and Brataas, A., "Spin-transfer torque in magnetic tunnel junctions: Scattering theory," *Physical Review B*, vol. 77, no. 22, p. 224419, 2008.

[159] Xiao, J., Zangwill, A., and Stiles, M., "Boltzmann test of slonczewskis theory of spin-transfer torque," *Physical Review B*, vol. 70, no. 17, p. 172405, 2004.

[160] Xiao, J., Zangwill, A., and Stiles, M., "Macrospin models of spin transfer dynamics," *Physical Review B*, vol. 72, no. 1, p. 014446, 2005.

[161] Xiao, J., Zangwill, A., and Stiles, M., "A numerical method to solve the boltzmann equation for a spin valve," *The European Physical Journal B*, vol. 59, no. 4, pp. 415–427, 2007.

[162] Xiao, J., Zangwill, A., and Stiles, M., "Spin-transfer torque for continuously variable magnetization," *Physical Review B*, vol. 73, no. 5, p. 054428, 2006.

[163] Yafet, Y., "g factors and spin-lattice relaxation of conduction electrons," *Sol. State Phys.*, vol. 14, p. 1, 1963.

[164] Yakushiji, K., Ernult, F., Imamura, H., Yamane, K., Mitani, S., Takanashi, K., Maekawa, S., and Fujimori, H., "Enhanced spin accumulation and novel magnetotransport in nanoparticles," *Nature Mater.*, vol. 4, p. 57, 2005.

[165] Zangwill, A., *Modern electrodynamics*. Cambridge University Press, 2013.

[166] Zeller, H. R. and Giaver, I., "Tunneling, zero-bias anomalies, and small superconductors," *Phys. Rev.*, vol. 181, p. 789, 1969.

[167] Zyazin, A. S., van den Berg, J. W., Osorio, E. A., van der Zant, H. S., Konstantinidis, N. P., Leijnse, M., Wegewijs, M. R., May, F., Hofstetter, W., Danieli, C., and others, "Electric field controlled magnetic anisotropy in a single molecule," *Nano letters*, vol. 10, no. 9, pp. 3307–3311, 2010.

[168] Zyazin, A. S., van der Zant, H. S., Wegewijs, M. R., and Cornia, A., "High-spin and magnetic anisotropy signatures in three-terminal transport through a single molecule," *Synthetic Metals*, vol. 161, no. 7, pp. 591–597, 2011.

VITA

Patrick Gartland was born a giddy lad in dewy Mountain Brook, AL. There he was blessed with true friends, and with many teachers throughout the years who not only instilled in him a sense of the joy that came with learning, but who also expressed personal interest in his well-being. As a result, he developed a love of physics, music, math, and poetry. Upon graduating from Mountain Brook High School, Patrick travelled to Auburn University to study Physics at 'The Loveliest Village On The Plains'. There he met the fair lass Ashley, who was to become his closest friend. After graduating from Auburn, Patrick continued on to pursue his PhD in physics at Georgia Tech in Atlanta, GA. After some time in graduate school, the giddy lad asked for fair Ashley's hand in marriage, and they began their life adventure together. In November of 2015, Patrick met with his committee to defend his dissertation.